Phase transformation in TZP-ZrO_2 under local stress and numerical simulation

Dissertation

der Mathematisch-Naturwissenschaftlichen Fakultät

der Eberhard Karls Universität Tübingen

zur Erlangung des Grades eines

Doktors der Naturwissenschaften

(Dr. rer. nat.)

vorgelegt von

M.Sc. Xin Wang

aus Huaibei, Volksrepublik China

Tübingen

2010

Tag der mündlichen Qualifikation:	14.12.2010
Dekan:	Prof. Dr. Wolfgang Rosenstiel
1. Berichterstatter:	Prof. Klaus Nickel, PhD
2. Berichterstatter:	Dr. Christoph Berthold

Declaration

I herewith declare that that this dissertation was done by me without external help other than those sources declared and cited. This thesis has not been forwarded to any other examination committee. All formulations, which were taken literally or in the meaning of other sources are cited accordingly.

Acknowledgement

I am sincerely thankful to all the people, who have helped and supported me during my work for this dissertation.

First, I would like to thank my supervisor Prof. Dr. Klaus Nickel, who gave me the opportunity to carry out my dissertation in his group and whose guidance, encouragement, kindness and wisdom have always been an important backup for me.

Thanks also to Dr. Christoph Berthold, who has showed me how to operate the universal testing machine and supported me with XRD measurements as well.

Many thanks to my dear colleague Dr. Haibin Zhang, for his very valuable help, for discussing the results and for providing lots of good ideas.

I am grateful to Dr. Bernd Binder, who took the time to introduce me into the Raman instrumenttation and who helped me out with difficulties concerning the Raman measurements.

Special thanks go to Dr. Michael Dorn, who helped and supported me with insight from his work, which my work based upon.

Thanks to Mr. Daniel Russ for helping to find a way to ease the mountain of data treatment that needed to be done.

I thank our mechanical team, Ms. Indra Gill-Kopp and Ms. Barbara Maier for the difficult sample preparations, and Mr. Norbert Walker for the help with the rotary stage.

Thanks to Ms. Dimitrovice, for a lot of organizational help of all kinds and at any time.

Contents

1 Summary

The main topics of this Ph.D thesis are phase transformations of zirconia from the tetragonal phase to the monoclinic phase under local application of loads, and the numerical modelling of this mechanical process using the commercial finite element method (FEM) software ABAQUS. The aim of the experiments and simulations is to determine the critical stress value required of this material for phase transformation to occur.

The technique used in the experiments is to combine the Vickers indentation testing and Raman spectroscopy with blue laser light, and then to determine the monoclinic phase content around the Vickers indentation. Different stress values cause different levels of phase transformation and different monoclinic phase fractions. Monoclinic phase could not be detected in the unstressed area at a great distance from the indentation.

The numerical simulation was performed using ABAQUS/standard Version 6.5 and 6.7 with 2D and 3D models. The maximum principal stress is particularly chosen to consider the stress field distribution for the contact problem.

This thesis concerns the following:

Determination of hardness and fracture toughness, influence factors on indentation, depth profile of Raman spectroscopy, top surface and lateral distribution of the monoclinic phase, residual stress analysis, influence factors on stress field, analysis of stress field of Vickers indentation in FEM, determination of critical stress required for phase transformation.

1 Zusammenfassung

Die Schwerpunkte dieser Dissertation sind Phasenumwandlungen von der tetragonalen in die monokline Phase in ZrO_2 unter lokaler mechanischer Belastung sowie die numerische Modellierung der mechanischen Prozesse unter Zuhilfenahme kommerzieller FEM-Tools – in diesem Fall ABAQUS. Ziel der Kombination aus Experiment und Simulation war es die kritischen Spannungswerte, ab welchen sich die Phasenumwandlungen ereignen, zu ermitteln.

Die Realisierung der Experimente bestand darin um die mittels Vickers-Härteeindruckverfahrens produzierten Eindrücke Mikro-Raman-Spektroskopie zu betreiben und auf diesem Wege den Anteil der monoklinen Phase um den Eindruck zu ermitteln. Unterschiedliche Spannungswerte führen zu unterschiedlichem Ausmaß der Phasenumwandlungen und zu unterschiedlichen monoklinen Phasenanteilen. In unbelasteten Bereichen mit großer Entfernung zum Eindruck konnte kein monokliner Phasengehalt nachgewiesen werden.

Die numerische Simulation wurde gemäß der Symmetrie mit zwei- und drei-dimensionalen Modellen unter Verwendung von ABAQUS/standard version 6.5 durchgeführt. Die maximale Grundspannung ist speziell ausgewählt um die Spannungsfeldverteilung für das Kontaktproblem zu berücksichtigen.

Diese Arbeit befasst sich mit folgenden Aspekten:

Bestimmung der Härte und Bruchzähigkeit, Einflussfaktoren auf das Eindruckverhalten, Tiefenprofil mittels Raman-Spektroskopie, Oberflächen- und laterale Verteilung der monoklinen Phase, Restspannungsanalyse, Einflussfaktoren auf das Spannungsfeld, Analyse der Spannungsfelder der Eindrücke mittels FEM, Bestimmung der kritischen Spannungswerte für die Phasenumwandlung.

2 Introduction

The earliest work of ceramics were making and decorating pottery, which appeared much earlier than metals. Ceramic materials (inorganic, non-metallic materials), metals and organic materials constitute the main body of engineering materials.

The modern design and manufacture of machines and equipment require modern materials with advanced mechanical, thermal, electrical, magnetic and anticorrosive properties. High-performance engineering ceramics meets these material requirements. Due to developments in material science, more is known about material structures and properties, thus improving the productivity and quality of various ceramics.

On account of its non-active chemical property, high strength and fracture toughness, good abrasion and wear resistance, high melting point, high electrical resistivity, and high index of refraction, zirconia has become very important to modern engineering material, thermostable material and ceramic insulate material

Zirconia (Zirconium dioxide, ZrO_2) has a natural mineral form called monoclinic crystalline structure. Pure monoclinic zirconia transforms into tetragonal and cubic crystal structures with an increase in temperature. Cubic zirconia is transparent, known most famously as diamond simulate. The volume expansion of zirconia during the transformation from cubic to tetragonal to monoclinic induces very high stress, which leads to the destruction of its fabric components.

The phase transformation from tetragonal to monoclinic phase at room temperature under an applied stress, combined with the associated volume expansion, suppresses and retards the growth of a crack in the zirconia and accounts for the fracture toughness of this material. This phase transformation can reinforce the material's mechanical properties, which in turn influence its commercial status as engineering ceramics. It is important to research such behaviour in the material to understand this relationship more clearly.

Stabilized zirconia has high refractability, low specific heat and heat conductivity. It therefore may be used for the inner wall of a blast furnace as an ideal thermic insulant material. It also may be used as thermostable coating, or as an additive to metal to resist high temperatures.

The electrical resistivity of zirconia decreases greatly with increasing temperature. Due to its apparent ionic conductivity at high temperature, this material may be used as a heating element, as electrode material, or as a solid electrolyte of a fuel cell at high temperature. Due to its oxygen ionic conductivity, zirconia is used to produce oxygen sensors that measure oxygen consistency and control the combustion of engines in the steel industry.

Metastable zirconia ceramics has very good mechanical properties, low thermal conductivity, and large thermal expansion coefficients. For this reason it is similar to metallic elements. Some parts of ceramic engines such as the cylinder, piston and valve, are currently made of a composite of zirconia and metals.
In addition, zirconia ceramics may be used as unlubricated bearing in the mining industry to create nozzles, mulling balls and components in the metallurgical industry. It might also be used to make scissors and knives of high toughness. Furthermore, zirconia ceramic material is now commonly used as a biological ceramic material because it does not react with organisms.

Different oxides such as yttrium oxide, magnesium oxide, calcium oxide and cerium oxide, are added into monoclinic zirconia to obtain the tetragonal phase. The transformation of the stabilized tetragonal into the monoclinic phase leads to the increase of toughness under local pressure. This is the basis for the applications that require high wear resistance and high strength and toughness.

The intrinsic brittleness and low reliability of ceramic materials are the main restrictions to industry applications. However, the phenomenon of stabilized zirconia with increased toughness helps in overcoming brittleness. The toughening mechanisms include stress-induced transformation toughening, microcrack toughening and residual toughening, et al. These mechanisms may interact with or complement each other.

Raman spectroscopy is used to characterize the properties and structures of different zirconia phases. As a non-destructive technique, Raman spectroscopy is based on the inelastic scattering (Raman scattering) of monochromatic light from a laser in the visible range. The laser light interacts with the sample, excites the molecules, and transforms them into oscillating dipoles. The energy shifts supply the information of the materials.

The main advantages of Raman spectroscopy lie in its simple (no special preparation for samples), rapid (short timescale), and non-destructive applications for both powder and bulk samples. In particular, the scale that micro-Raman spectroscopy detects can reach micrometer, which is a crucial advantage in investigating the grain boundary of phases and locally-dependent changes in the structure. The information of the sample, such as crystal structure, composition, orientation of crystallites and crystal, is reflected in the height, width, position and shape of the bands of the Raman spectrum.

In recent years, the computer simulation of physical processes has developed as an interesting direction of research in the development of materials and their structural behaviour. This method affords opportunities to analyze numerically, which is otherwise expensive and complicated to practice. The Finite Element Method (FEM) has proved to be a good numerical method for solving indentation problems, as it gives quantitative estimation for indentation stress field.

As commercial software, ABAQUS can solve problems ranging from relatively simple linear analyses to the most challenging nonlinear simulation. Both preprocessors and postprocessors can be executed with ABAQUS.

This thesis is divided into two parts: the first part is an overview of zirconia and the investigation method of Raman spectroscopy and its applications. This includes the identification of the different phase states, the corresponding Raman spectra, and dependence on various device parameters. The other part is numerical simulation, which represents the indentation process in ABAQUS, and calculates the stress distribution.

The present work involves the following parts:

Hardness testing is an important method used to define the mechanical properties and other characters of materials. The first part of the thesis describes hardness testing methods and their effects on the investigated samples. The beginning of this thesis introduces different hardness testing methods and their application to material research.

In the second part various zirconia ceramics are presented and associated with their structures, mechanical and thermal properties, and possible phase transitions under external mechanical conditions, as well as with the low-temperature degradation.

Raman spectroscopy is introduced in detail afterward, including the theoretical principle and instrumentation, the Raman bands of different zirconia phases, Raman shifts under pressure, and the influence of temperature, grain size and dopants on Raman spectra.

The fourth point of the theoretical principle is the introduction of the FEM, including the element's stiffness matrix. The stages of the chosen commercial software ABAQUS are illustrated and the needed parameters are explained.

Following the introduction of the theoretical principal are the experiments and results. This includes the equipment used in the experiments, and the characterization and preparation of the samples. The results are then presented, including the evaluation of hardness, fracture toughness, the effect of focusing on Raman bands of different materials, and the mapping of monoclinic fraction.

For the FEM simulations, the influences of yield stress, elastic modulus and Poisson's ration on the calculation were previously researched by the author of this work. For the real TZP material and the experiment condition, modelling under the forces of 100 N and 250 N was executed, and stress distributions were obtained. The results of the following experiments and simulations give rise to an estimate of the critical stress needed for this material to undergo phase transition.

3 Theoretical principal

3.1 Hardness testing

In materials science, hardness is defined as the resistance of a material to permanent deformation, scratching and erosion. This is an important property for engineering applications. Hardness testing is achieved by indenting the testing material with a hard indenter of known geometry and mechanical properties. The indenter may be spherical, conical, or pyramidal.

3.1.1 Classification

In ceramics, common techniques used to measure hardness are Vickers (HV), Knoop (HK), and Rockwell (HR). Hardness values involve the size of residual plastic impression and the applied load. For brittle ceramic materials, the hardness is conveniently measured with a diamond pyramid indenter, since the residual impression can be easily obtained with relatively low values of indenter load.

3.1.2 Vickers diamond hardness

The Vickers indenter is a pyramid diamond with opposite faces at an angle of 136° (22° between the indenter face and sample surface [1]; d is the length of the diagonal measured from corner to corner), and the formed impression on the sample surface is a square (Fig. 1).

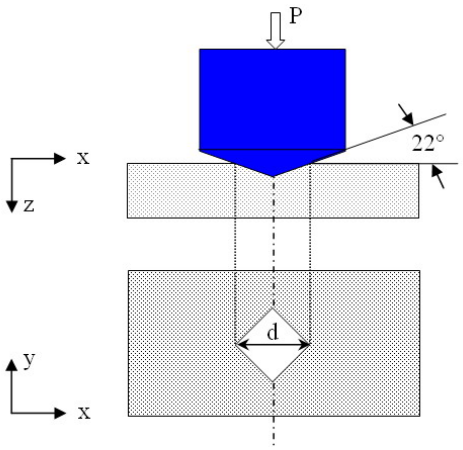

Fig. 1 Schematic diagram of Vickers indentation.

The Vickers hardness (HV) is calculated from the applied load and the actual surface area of the impression:

$$HV = \frac{P}{A_{actual}} \qquad (1)$$

Actual surface area can be determined from projected area as shown in Fig. 2:

$$A_{actual} = \frac{A_{proj.}}{\sin 68°} \tag{2}$$

where $a = \frac{d}{\sqrt{2}}$ and $A_{proj.} = a^2 = \frac{d^2}{2}$. Then $A_{actual} = \frac{d^2}{2\sin 68°}$.

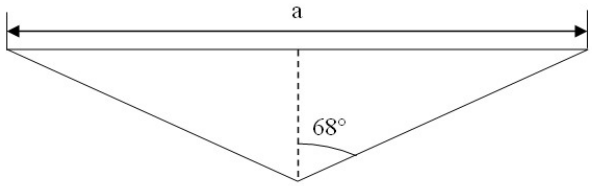

Fig. 2 Transverse section of Vickers indenter.

So

$$HV \quad \frac{P}{A_{actual}} \quad \frac{2P}{d^2}\sin 68 \quad = 1.86\frac{P}{d^2} \tag{3}$$

Then the corresponding unit of HV is kilogram force per square millimetre (kgf/mm²). To convert a Vickers hardness number into SI units (MPa or GPa) one must convert the force applied from kgf to newtons and the area from mm^2 to m^2 to give results in pascals (1 kgf/mm² = 9.80665×10^6 Pa).

Vickers hardness numbers are reported as **xxxHVyy**, e.g. **500HV35**, where: **500** is the hardness number, **HV** gives the hardness scale (Vickers), and **35** indicates the load used in kg.

For small indentation loads (<9.8 N), problems always arise from the significant load dependence of hardness and measurement uncertainty due to the small indentation size. For higher loads (>49 N), cracking and spalling can be a problem and may make measurement impossible.

3.1.3 Knoop hardness

Frederick Knoop developed an elongated pyramidal diamond indenter as an alternative to the square pyramidal Vickers indenter in 1934 at the National Bureau of Standards in the United States. The diamond pyramid of the Knoop indenter has unequal length edges, whose impression has one diagonal with a length seven times the shorter diagonal. The angles for the opposite faces of a Knoop indenter are 172°30’ and 130° (Fig. 3). Because of the smaller depth of penetration by a given indenter load, the Knoop indenter is especially useful for highly brittle materials to overcome the cracking, and it is also very useful for researching the anisotropy of the surface of the specimen.

As shown in Fig. 4, the length of the longer diagonal is used to determine the projected area of the impression. The Knoop hardness number is calculated from [1]:

$$HK = \frac{P}{A_{proj.}} \tag{4}$$

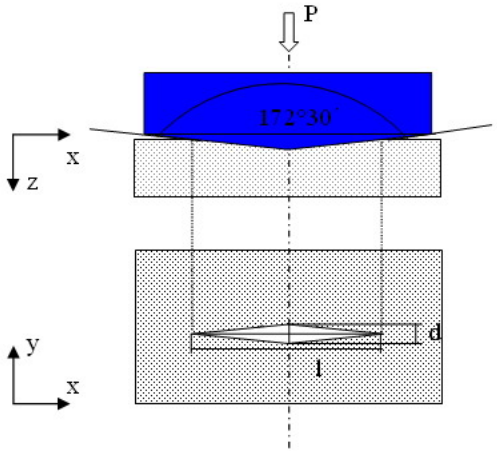

Fig. 3 Geometry of a Knoop indenter.

The projected area is:

$$A_{proj.} = 2\frac{l}{2}\frac{d}{2} \tag{5}$$

and

$$\frac{l}{\tan 86.25°} = \frac{d}{\tan 65°} \tag{6}$$

then

$$A_{proj.} = 2\frac{l}{2}\frac{l\cot 86.25°\tan 65°}{2} = \frac{l^2}{2}\cot 86.25°\tan 65° \tag{7}$$

so

$$HK = \frac{P}{\frac{l^2}{2}\cot 86.25°\tan 65°} = 14.229\frac{P}{l^2} \tag{8}$$

Similar to Vickers hardness numbers, **1000HK1** denotes a Knoop hardness of 1000 (dimensionless) determined from a test force of 9.807 N (1 kgf). Alternately, **10GPaHK9.807N** is described with the SI unit denoting a Knoop hardness of 10 GPa determined from a force of 9.807 N (1 kgf).

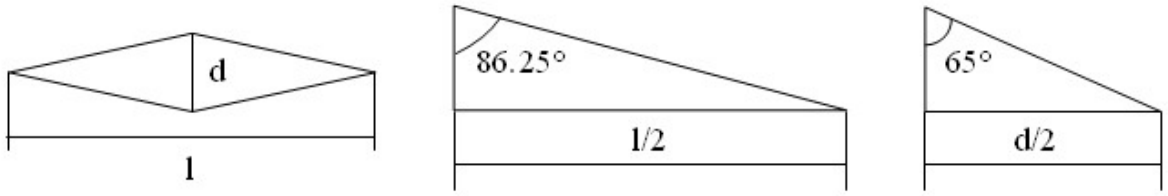

Fig. 4 Transverse section of a Knoop indenter.

3.1.4 Rockwell hardness

The Rockwell hardness was introduced by metallurgist Stanley Pickett Rockwell in 1920. In the Rockwell method of hardness testing, the depth of penetration of an indenter under certain test conditions is determined. The indenter may either be a steel ball of a specified diameter used for softer materials (Rockwell B scale), or a spherical diamond-tipped cone of 120° angle and 0.2 mm tip radius used for hard materials (Rockwell C scale).

The indenter is forced into the test material under a preliminary minor load (Fig. 5), which is usually 10 kgf, and causes an initial penetration. When equilibrium has been reached, an indicating device, which follows the movements of the indenter and so responds to changes in penetration depth, is set to a datum position. While the minor load is still applied, an additional major load is applied with resulting increase in penetration. When equilibrium has again been reached, the additional major load is removed but the preliminary minor load is still maintained. Removal of the additional major load allows a partial recovery, so reducing the depth of penetration. The permanent increase in depth of penetration, resulting from the additional major load is used to calculate the Rockwell hardness number:

$$HR = E - e \tag{9}$$

where e is permanent increase in penetration depth due to the major load measured in units of 0.002 mm, and E is a constant depending on the form of the indenter: 100 units for diamond indenter, 130 units for steel ball indenter.

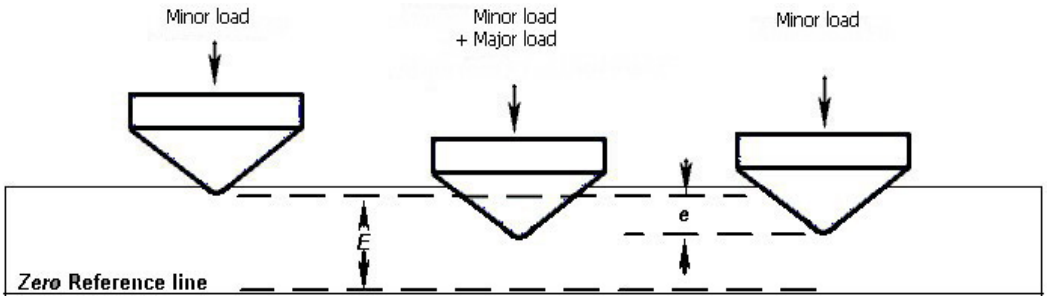

Fig. 5 Rockwell hardness testing.

For example, with a diamond indenter the final depth is 0.08 mm, and the Rockwell hardness number obtained from Eq. (9) is:

$$HR = 100 - \frac{0.08}{0.002} = 60$$

which will be written as **60HRC**.

The main advantage of Rockwell hardness testing is that the hardness number can be read directly on the dial gage without the necessity of measuring the indentation dimensions, as in other hardness testing methods such as Vickers or Knoop.

3.1.5 Problems with application of hardness testing

3.1.5.1 Hardness anisotropy

For anisotropic crystalline materials, orientation plays an important role in hardness values. [2]The effect of crystallographic anisotropy on the room-temperature Knoop [3]microhardness of silicon carbide single crystals has been studied on each of three major sections, namely $\{1\bar{1}00\}$ and $\{11\bar{2}0\}$ in Fig. 6. The hardness anisotropy on the prism planes $\{1\bar{1}00\}$ and $\{11\bar{2}0\}$ is more obvious than that observed on the basic plane. In each case the lowest hardness number was found along the axis of the indenter parallel to [0001].

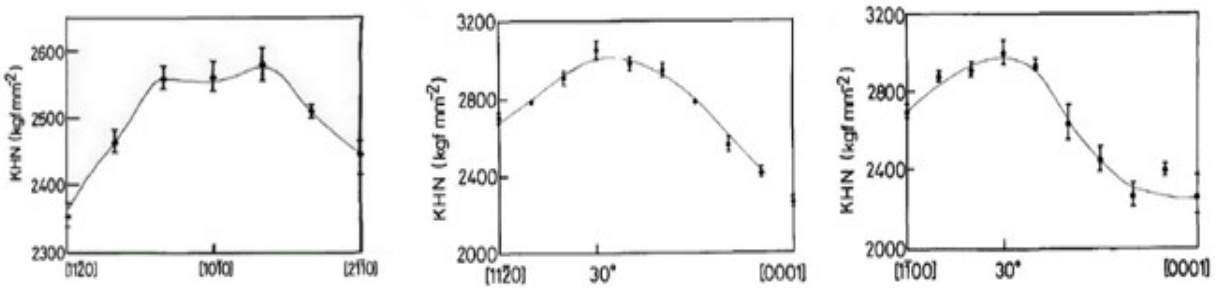

Fig. 6 Knoop hardness anisotropies determined on three different prominent planes for SiC single crystals. From left to right: {0001}, $\{1\bar{1}00\}$ and $\{11\bar{2}0\}$, respectively[2].

3.1.5.2 Hardness and microstructure

The hardness of ceramics depends on the microstructure of the materials, such as grain size, grain morphology, secondary phase and porosity (Fig. 7). These factors all influence the hardness testing. For example, the porosity dependence on hardness numbers can be expressed as [4]:

$$H = H_0 \exp^{-bP} \qquad (10)$$

where H_0 is the hardness without porosity, P is the volume fraction of porosity and b is a constant.

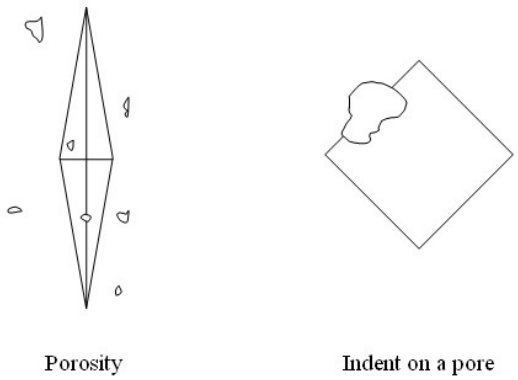

Fig. 7 Schematic drawing of porosity effect on hardness testing.

The effect of grain size on hardness of sintered alumina (ground with 0.3 μm diamond powder) given by Krell and Bland [5] was shown in Fig. 8. It is possible to increase the Vickers hardness of pure alumina by reducing its grain size.

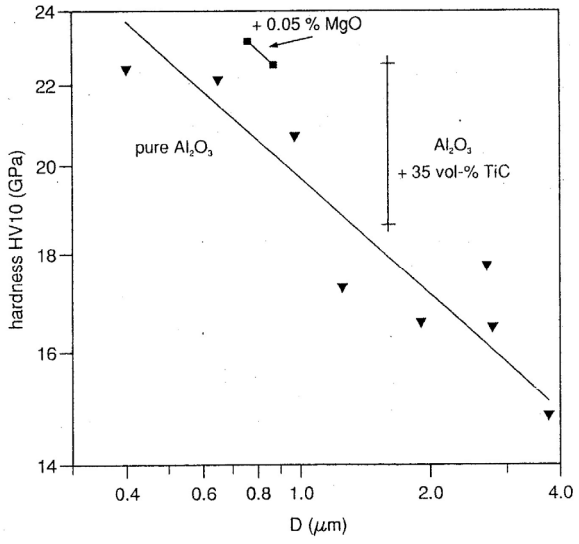

Fig. 8 Grain size dependence of the Vickers hardness of sintered alumina ceramics with ground surfaces[5].

3.1.5.3 Indentation size effect

The application of microhardness indentation techniques involves the law that the hardness decreases with increasing indentation load at low levels of the testing load; this is called indentation size effect and is described traditionally by a power law [6]:

$$P = ad^n \tag{11}$$

where P is the load, a is a constant, d is the diameter of the indentation produced, and n is the Meyer of logarithmic index. Equation (11) is sometimes referred to as Meyer's law. For most materials, the power law exponent, n, is experimentally observed between 1 and 2, which indicates that a low indentation load results in a higher microhardness number.

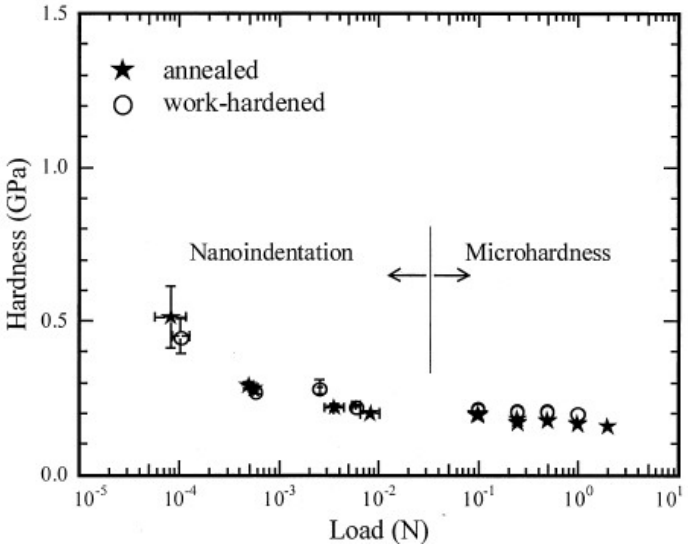

Fig. 9 Hardness vs. load for annealed and work-hardened aluminium[7].

The phenomenon of the indentation size effect exists in a variety of indentor geometries, including the Knoop, Vickers and Brinell. The relationship of Vickers hardness with an indentation load of 99.999% aluminium can be observed in Fig. 9 [7]. Vickers hardness increases when the load decreases.

A schematic diagram of the indentation size effect and microhardness results on the (100) in the [001] for both rutile and cassiterite are given in Fig. 10[7, 8]. The diagram proves that indentation size effect only contributes to the measured microhardness at test loads smaller than a critical value.

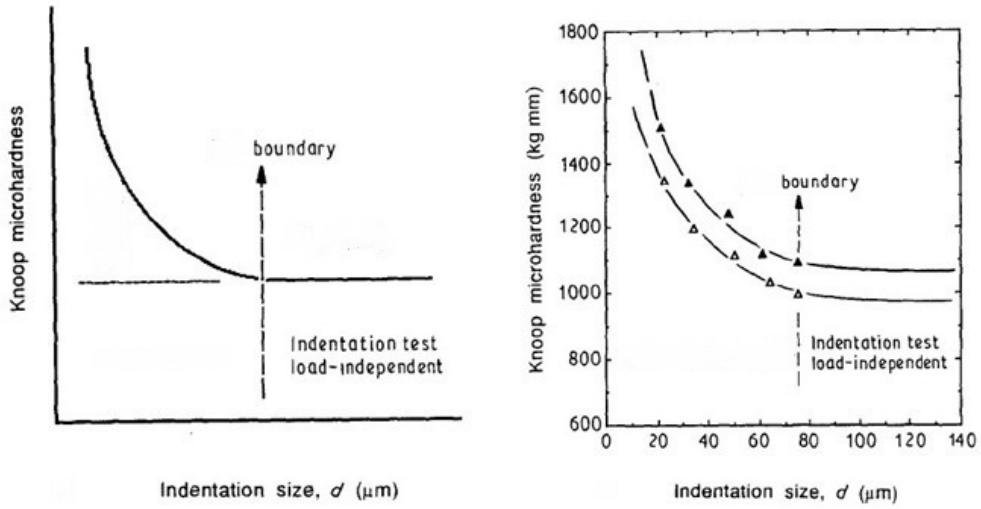

Fig. 10 Left: Schematic drawing of the indentation size effect; right: indentation size effect for single crystals of TiO_2 and SnO_2 for the (100) [001] crystallographic reference[7, 8].

In the past different explanations accounted for indentation size effect [7, 8]. Iost suggested that this phenomena is artificial, i.e. the variation of the hardness according to the applied load is only a result of the variation of the contact surface between the specimen and the indenter [9]. Li, et al.,

revealed that indenter/specimen interfacial friction has a significant effect on the low-test-load indentation microhardness [10]. Ma and Clarke regarded the changing of dislocation density as a reason for indentation size effect [11]. However, the mechanical and physical processes involved are still not fully understood.

3.1.5.4 Fracture toughness

Fracture may be defined as the mechanical separation of the solid due to the application of stress. Fractures of engineering materials are normally categorized as ductile or brittle, and fracture toughness is defined as the resistance to the propagation of crack, related to the amount of energy required to create fracture surfaces. The propagation is often regarded to be unstable for brittle materials, leading to a complete separation of the component into several pieces. Fracture toughness is one of the most important properties of materials for design applications.

There are three modes of applying a load to enable a crack to propagate: Mode I, opening or tensile mode, normal to the plane of the crack; Mode II**,** sliding or shear mode, acting parallel to the plane of the crack and perpendicular to the crack front; Mode III**,** tearing mode, acting parallel to the plane of the crack and parallel to the crack front (Fig. 11). However, the great majority of all actual cracking and fracture cases are Mode I problems, and fracture mechanics is generally confined to this mode.

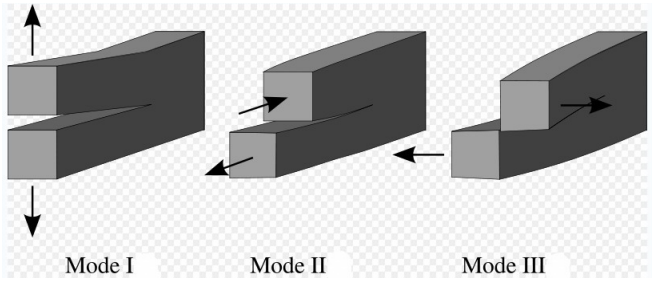

Fig. 11 Modes of loading.

For brittle materials, cracks may be generated in the surface by indentation contact. Five types of crack can be observed, shown in idealized form in Fig. 12 [12]. Cone cracks are typically generated by the elastic loading of spherical or flat-punch indenters. The cracks spread away from the surface at a certain angle to the load axis, after nucleation of a ring crack at the periphery of contact (Fig. 12(A)).

For sharp indenters like Vickers or Knoop, a remnant plastic impression in the surface is generated, which is known as elastic-plastic contact. In such a case, three types of crack are created (Fig. 12(B)-(E)) [1]:

i) Radial cracks, which are vertical half-penny cracks generated parallel to the load axis. Such cracks occur on the surface of the specimen outside the plastic contact impression (usually at the intention corner), and remain close to the surface. These radial cracks are generated by a hoop stress and extend downward into the specimen but are normally quite shallow.

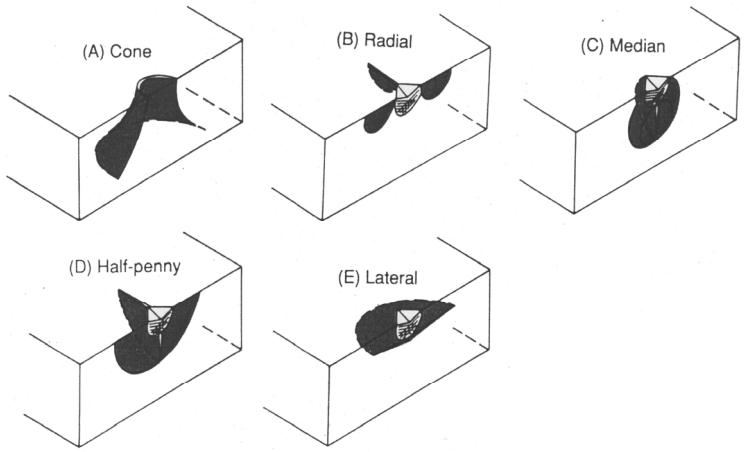

Fig. 12 Isometric sections of idealized crack morphologies observed at indentation contacts: (A) cone crack and associated nucleating ring crack, (B) radial cracks and associated contact impression and plastic deformation zone (Vickers indenter), (C) median crack, (D) half-penny cracks, and (E) lateral crack [12].

ii) Median cracks, which are vertical circles or circular penny cracks generated also parallel to the load axis, but just beneath the surface along the axis of symmetry, and have a direction aligned with the corners of the residual impression. Depending on the loading conditions, the median cracks may extend upward and attach to surface radial cracks, or radial cracks may grow downward, or the two sets of cracks coalesce, to form two half-penny cracks which intersect the surface. These cracks are generated due to the action of an outward stress.

iii) Lateral cracks, which are horizontal cracks also generated beneath the deformation zone, parallel to the surface. They arise due to a tensile stress, and often extend to the surface, leading to a surface ring which may cause the chipping of the surface of the specimen.

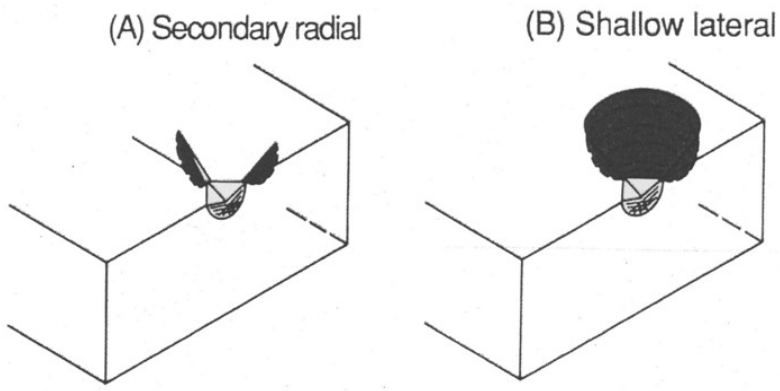

Fig. 13 Isometric sections of crack morphologies observed at indentation contacts: (A) secondary radial cracks and (B) shallow lateral cracks [12].

Two other important variations of the major types of cracks mentioned previously are shown in Fig. 13 [12]. Secondary radial cracks occur from the edge of the contact impression adjacent to the indentation corner, and grow into the surrounding material at an angle to the load axis, and stay very close to the surface (Fig. 12(A)). Shallow lateral cracks are created at the edge of the

contact impression and propagate into the material almost parallel to the surface, always bounded by radial or secondary radial cracks (Fig. 13(B)).

The type of crack observed depends on the material, the shape of the indenter, the loading rate, and the environment. Any or all of the above crack types may occur in different combinations as a result of these variables.

A crack in a loaded specimen generates its own stress field ahead of a sharp crack, which can be characterized by a single parameter called stress intensity. Stress intensity includes the effect of the stress applied to a sample as well as the effect of a crack of given size in the sample. It involves complex geometry factors for complex loading, various configurations of real structural components, and variations in crack shapes. Rapid crack propagation is controlled by critical stress intensity factor, which is a material constant. The greater value of this factor, the higher the stress required to produce rapid propagation and the greater the resistance of the material to brittle facture.

Fracture toughness is a nomenclature for critical stress intensity factor, including the loading mode. K_{IC} (unit: $MPa\sqrt{m}$) is the fracture toughness under Mode I loading, where index I denotes Mode I loading and C denotes critical. Fig. 14 shows a schematic of the indentation deformation/fracture pattern for the Vickers geometry: P is the peak load, l is the crack length, c and a are characteristic dimensions of the plastic impression and penny-like radial/median crack, respectively [13].

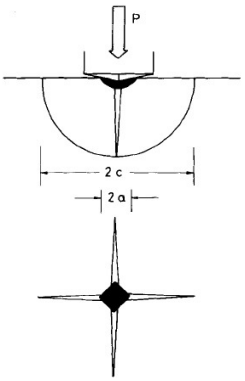

Fig. 1 Schematic of Vickers-produced indentation-fracture system[13].

From simplistic dimensional analysis, toughness K_{IC} can be expressed as:

$$K_{IC} = \frac{P}{\beta_0 c^{1.5}} \tag{12}$$

where β_0 is to be regarded as a numerical constant, corresponding to a complex geometrical factor for penny-like systems. This incorporates interaction effects due to the presence of the specimen-free surface, multiple-plane crack configuration, etc., and is normally determined by experimental calibration.

Lawn, Evans, and Marshall [14] gave a formula, where they treated the fully formed median/radial crack system and found that the ratio $P/c^{1.5}$ is a constant, and the value depends on the material of the specimen:

$$K_{IC} = 0.016\left(\frac{E}{H}\right)^{0.5}\frac{P}{c^{1.5}} \tag{13}$$

where E is Young's modulus, H is hardness and c is measured from the center of contact to the end of the corner radial crack.

Evans and Charles gave an expression for a Vickers test on radial crack [15]:

$$K_{IC} = \frac{0.15kH\sqrt{a}}{\Phi}\left(\frac{c}{a}\right)^{-1.5} \tag{14}$$

where k=3.2 at large c/a values, and Φ is a constraint factor (≈3).

Niihara et al. gave a formula for median cracks (c/a≥2.5) [16, 17]:

$$K_{IC} = \frac{0.129H\sqrt{a}}{\Phi}\left[\frac{E\Phi}{H}\right]^{0.4}\left(\frac{c}{a}\right)^{-1.5} \tag{15}$$

and for the Palmqvist cracks (0.25≤l/a≤2.5):

$$K_{IC} = \frac{0.035H\sqrt{a}}{\Phi}\left[\frac{E\Phi}{H}\right]^{0.4}\left(\frac{l}{a}\right)^{-0.5} \tag{16}$$

Shetty et al. [18]:

$$K_{IC} = 0.0889\left(\frac{HP}{4\bar{a}}\right)^{0.5} \tag{17}$$

where $\bar{a}$ is the mean radial crack length.

Lankford [19]:

$$K_{IC} = \frac{0.142H\sqrt{a}}{\Phi}\left[\frac{E\Phi}{H}\right]^{0.4}\left(\frac{c}{a}\right)^{-1.56} \tag{18}$$

Laugier gave an expression for half-penny crack [20]:

$$K_{IC} = 0.015\left(\frac{a}{l}\right)^{0.5}\left(\frac{E}{H}\right)^{2/3}\frac{P}{c^{1.5}} \tag{19}$$

and for Palmqvist crack [21, 22]:

$$K_{IC} = 2.15*10^{6}\left(\frac{E}{H}\right)^{0.6}\left(1+0.012\frac{E}{H}\right)^{-0.6}H^{-1.5} \tag{20}$$

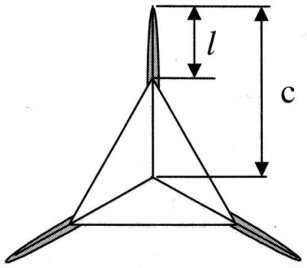

Fig. 15 Crack parameters for Berkovich indenter[23].

Most of the toughness determinations were performed using a Vickers diamond pyramid indentation technique. The advantages of a Berkovich (Fig. 15) indenter have become increasingly important, especially in ultra-micro-indentation. However, the loss of symmetry leads to some problems because the half-penny cracks can no longer join two corners of the indentation. Then a modifying factor is developed to account for the number of symmetric cracks [23]:

$$K_1 = \sqrt{\frac{n/2}{1+\frac{n}{2\pi}\sin\frac{2\pi}{n}}} \tag{21}$$

where n is the number of radial cracks, and for a Vickers indentation n=4 and for a Berkovich indentation n=3.

Then the Laugier expression is modified by Dukino et al. as:

$$K_C = 0.016\left(\frac{a}{l}\right)^{0.5}\left(\frac{E}{H}\right)^{2/3}\frac{P}{c^{1.5}} \tag{22}$$

3.1.6 Hertz theory of elastic contact

The analysis of the stresses from the contact between two elastic bodies was first studied by Hertz (1882). The assumptions made in the Hertz theory were [24]:

i) The surfaces of the bodes are continuous and non-conforming
ii) The strains are small
iii) Each solid can be considered as an elastic half-space
iv) The bodies are in frictionless contact

The pressure distribution proposed by Hertz is:

$$\sigma(r) = p_0\left[1-(r/a)^2\right]^{1/2} \tag{23}$$

where σ is the distribution of pressure, p_0 is the maximum pressure, a is the dimension of the contact area, and $r \le a$.
The total load compressing the solids is related to the pressure:

$$P = \int_0^a \sigma(r) 2\pi r dr = \frac{2}{3} p_0 \pi a^2 \tag{24}$$

Then the mean pressure p_m is:

$$p_m = \frac{P}{\pi a^2} = \frac{2}{3} p_0 \tag{25}$$

3.1.7 Indentation stress fields

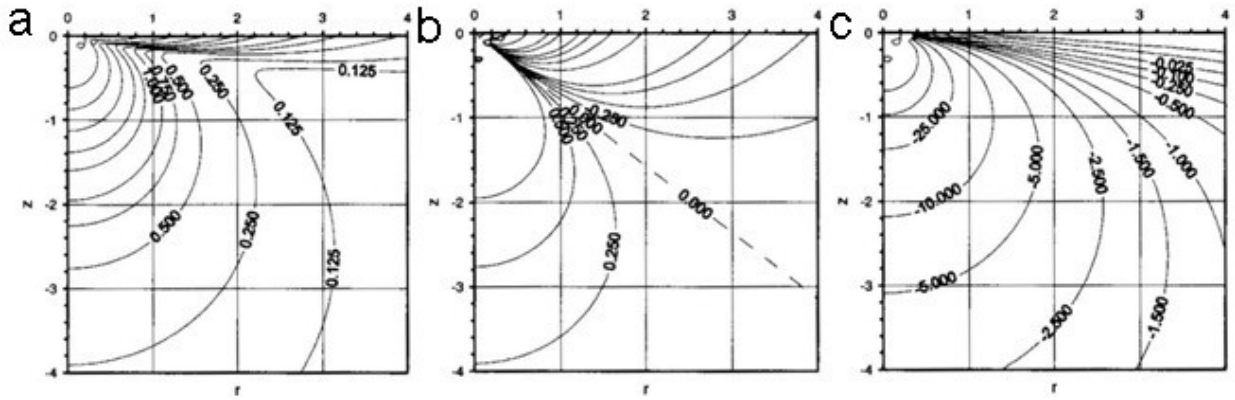

Fig. 16 Stress contours of equal stress in MPa for Boussinesq point load configuration: (a) σ_x (b) σ_y (c) σ_z [1].

The stresses within a solid loaded by a point contact were calculated by Boussinesq:

$$\sigma_x = \frac{P}{2\pi}\left[\frac{1-2\nu}{r^2}\left\{\left(1-\frac{z}{\rho}\right)\frac{x^2-y^2}{r^2}+\frac{zy^2}{\rho^3}\right\}-\frac{3zx^2}{\rho^5}\right]$$

$$\sigma_y = \frac{P}{2\pi}\left[\frac{1-2\nu}{r^2}\left\{\left(1-\frac{z}{\rho}\right)\frac{y^2-x^2}{r^2}+\frac{zx^2}{\rho^3}\right\}-\frac{3zy^2}{\rho^5}\right] \tag{26}$$

$$\sigma_z = -\frac{3Pz^3}{2\pi\rho^5}$$

where P is a concentrated point force, $\rho = \left(x^2+y^2+z^2\right)^{1/2}$ and υ is Poisson's ratio. Stresses for point load P=100N calculated using equations above are shown in Fig. 16 [1].

3.2 Zirconia materials

3.2.1 The polytypes of zirconia

The main source of zirconia is the mineral zircon ($ZrSiO_4$) which typically contains significant Al_2O_3, HfO_2 and TiO_2 impurity. Commercial zircon is normally mined from beach sand sources. Another source of zirconia is the mineral baddeleyite, which is 80-90% monoclinic zirconia with HfO_2, TiO_2, Fe_2O_3 and SiO_2 impurities. Commercial baddeleyite deposits are found in Brazil and South Africa.

Undoped zirconia has three solid polymorphisms of monoclinic, tetragonal, and cubic phases at atmospheric pressure. The coordination polyhedra of the polymorphs are shown in Fig. 17 by Yashima [25]. The low-temperature stable monoclinic phase of zirconia (space group $P2_1/c$) martensitically transforms into the tetragonal phase (space group $P4_2/nmc$) at about 1170 K, and then a phase transition occurs from this tetragonal phase to a cubic fluorite type structure (space group Fm3m) above 2370 K. Both monoclinic and tetragonal phases have distorted fluorite structures, and the phase transitions among them are diffusionless in nature. During this diffusionless phase transition, the oxygen O_1 atom has an important role, considering that the longest shift in the phase change should be the movement of the O_1 atom attached to the ZrO_7 group. Its coordination number changes from 3 (monoclinic) to 4 (tetragonal) [26].

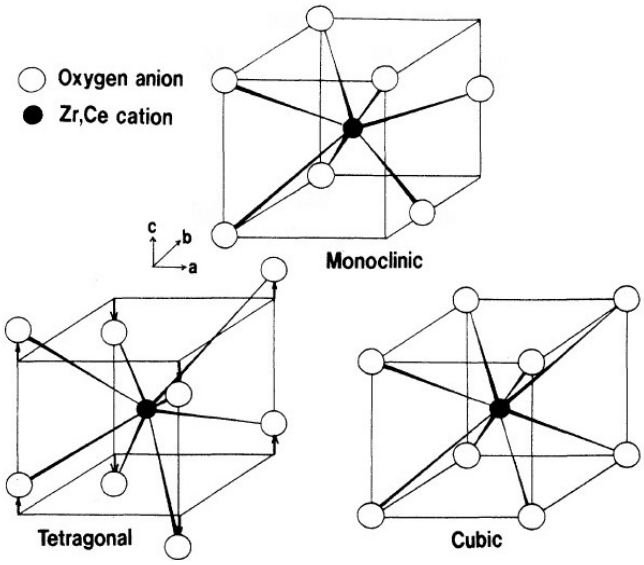

Fig. 17 Schematic cation coordination polyhedra in monoclinic, tetragonal, and cubic zirconias[25].

The transformation from monoclinic to tetragonal exhibits a hysteresis. The transformation from *t* to *m* on cooling occurs over a temperature range of about 100 °C to 1170 °C. The transformation from monoclinic is martensitic and it results in a volume increase on the order of 3-4% during cooling. This volume change is sufficient to exceed the elastic limit of the zirconia grains and to cause cracking.

When the temperature increases to 2370 °C, a face-centered cubic fluorite structure is formed, and the density increases. The melting point is approximately 2715 °C. Other metastable orthorhombic phases at higher temperature were discussed in section 3.2.7.1. Information about different

modifications of zirconia is listed in Table 1 [27-31]. Lattice parameters of the cubic, tetragonal, and monoclinic phases of zirconia are listed in Table. 2 [31-34].

Phase	Space group	Density	T (°C)	Coordination		
				Zr	O_1	O_2
Monoclinic	$P2_1/c$	5.6	<1170	7	3	4
Tetragonal	$P4_2/nmc$	6.1	1170-2370	8	4	4
Cubic	Fm3m	6.27	2370-2715	8	4	4

Table 1 The three low-pressure phases of zirconia. The last three columns give the coordination numbers of the Zr and O atoms[27-31].

	Cubic	Tetragonal	Monoclinic
a (Å)	5.09	3.571	5.192
c/a		1.451	1.032
b/a			1.012
β (°)			99.23

Table 2 Lattice parameters of different phases of zirconia[31-34].

3.2.2 The monoclinic-tetragonal phase transformation

The monoclinic to tetragonal phase transformation and its reverse are martensitic transformations and involve large shear strains because they are diffusionless, stress-assisted and athermal. This transformation, like most martensitic transformations, is stress-assisted because the local stress state can interact with the unit cell transformation strain to ease the nucleation of the martensite phase. The stress can be external, such as applied stresses during mechanical testing, or internal, such as thermal expansion mismatch or coherency stresses. The monoclinic phase nucleates preferentially at grain boundaries [35], where the stress concentration exists, and grows across individual grains. The martensite lath stops at a grain boundary after completing crossing, causing stress concentration again, which leads to a different oriented lath to nucleate and begin to grow. This is known as autocatalysis.

In addition to being stress-assisted and autocatalytic, the transformation could also be activated thermally, which involves either nucleation of the martensite phase, water transport for moisture-assisted transformation, or oxygen diffusion. The resulting isothermal transformation at low temperatures causes significant changes in the mechanical properties of the material, which will be discussed later.

The monoclinic variants are almost twin-related at $(100)_m$, with a junction plane between the variants parallel to $(100)_m$. There are two distinct orientation relationships (OR) for the monoclinic and tetragonal phases [27]:

OR1 $(100)_m \| (010)_t$ and $[001]_m \| [100]_t$

OR2 $(001)_m \| (100)_t$ and $[100]_m \| [010]_t$

The twinning mechanisms are responsible for the softness of the monoclinic form and the occurrence of the transformation, since the transformation is dependent on the sample grain size, and thus leads to changes in hardness.

Precise and qualitative investigation of the surface characteristics of martensitic transformation in zirconia was performed using atomic force microscopy by Deville et al. [36]. The grains' triple junctions appear as preferential nucleation sites during the formation of a self-accommodating variant pair.

3.2.3 Transformation thermodynamics

In order to better understand the relationship between transformation toughening and temperature behavior, transformation thermodynamics should be considered. This takes into account the martensitic transformation start temperatures and the critical transformation stress at a given temperature. In ceramic materials, the matrix constrains the tetragonal precipitates to undergo the volume expansive transformation, as follows:

$$\Delta U_T = \Delta G_c^{t\to m} + \Delta U_i = \Delta S(T_0 - T) + \Delta U_i \qquad (27)$$

where ΔU_T is the energy required for the transformation, $\Delta G_c^{t\to m}$ is the chemical free energy (zero at T_0), ΔU_i is the internal strain energy changes, and $\Delta S^{t\to m}$ (<0) is the entropy change for the tetragonal to monoclinic phase change, as shown in Fig. 18 [37, 38].

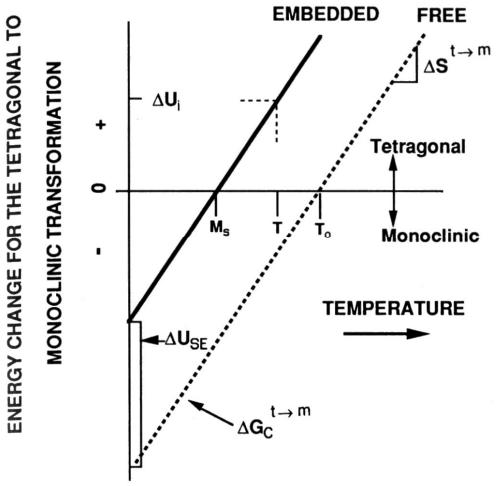

Fig. 18 The ability to transform the tetragonal phase of zirconia increases with decrease in temperature. Tetragonal zirconia particles and grains, which are prevented from transformation by the constraining effects of the surrounding matrix, transform on cooling to the martensite start temperatures, M_s. At temperatures above M_s, an external stress supplies the strain energy to initiate the transformation[37, 38].

During cooling, the tetragonal to monoclinic transformation can be initiated, even without applied external stress. Under such conditions, the transformation starts when the temperature T equals the martensite start temperature M_s, and ΔU_T is zero, thus:

$$\Delta U_i = \Delta H \frac{(M_s - T_0)}{T_0} = \Delta S^{t\to m}(M_s - T_0) \qquad (28)$$

When $T>M_s$ and $\Delta U_T>0$, the required additional energy to transform the tetragonal phase is:

$$\Delta U_T = \Delta S^{t\to m}(T_0 - T) + \Delta S^{t\to m}(M_s - T_0) = \Delta S^{t\to m}(M_s - T) \qquad (29)$$

For stress-induced transformations, the external strain energy, derived from the applied stress acting, can supply the additional energy on the matrix. The stain energy changes associated with the transformation are dilatation and shear strains which come from the tensile and shear stresses. The amount of required external strain energy ΔU_{SE} equals ΔU_T.

However, the scale of ΔU_{SE} and then the level of the external applied stress required to start the transformation can be reduced by internal tensile stresses existing in the materials, including thermal expansion anisotropy and the transformation stresses. In tetragonal polycrystalline zirconia, the anisotropy in crystallographic thermal expansion coefficients, α_A and α_C, provide additional local thermal expansion anisotropy (TEA) tensile stress to assist the transformation of tetragonal zirconia. In yttria stabilized tetragonal zirconia, $\Delta\alpha$, the thermal expansion anisotropy, and the associated TEA stresses decrease with increasing yttria content. For example, $\Delta\alpha$ becomes zero in the cubic phase. Therefore, under the same experiment and microstructural conditions, decreasing the ytrria content will increase the internal tensile stress and diminish the external stress required to transform the polycrystalline tetragonal zirconia.

Applied tensile stress, decreasing temperature, or combining can drive the martensitic transformation from tetragonal to monoclinic phase in zirconia. The applied tensile stress required to initiate the tetragonal to monoclinic transformation can be defined by equating ΔU_T to the applied strain energy. Then:

$$\sigma_a = \sigma_c^T = \Delta S^{t\to m} \frac{M_s - T}{\varepsilon^T} \qquad (30)$$

where σ_a is the applied stress, σ_c^T is the critical transformation stress, and ε^T is the transformation strain. σ_c^T approaches zero when M_s increases towards T. However, the measured value of σ_c^T is modified by the presence of internal residual stresses σ_i because of thermal expansion anisotropy or mismatch. The applied stress required is reduced in the presence of a tensile σ_i component:

$$\sigma_a = \sigma_c^T = (\sigma_c^T)_0 - \sigma_i \qquad (31)$$

where $\left(\sigma_c^T\right)_0$ is the stress required in the absence of internal tensile stresses.

The anisotropy in properties of tetragonal zirconia and in the matrix results in nonuniform stresses and local internal stress concentrations in the grains. The shape of the zirconia grains introduces re-entrant grain corners and edges, which further contribute to the local stress concentrations.

The related stress concentration profiles decay along x from the grain corner or edge. The thermal expansion anisotropy or mismatch σ_{TEA} is considered as the source of σ_i and the grain corner or

edge as the stress concentration feature. The resulting tensile stress concentration profile at a grain corner is:

$$\sigma_i = \sigma_{TEA}\frac{d}{x} \tag{32}$$

and

$$\sigma_i = \sigma_{TEA}\ln\left(\frac{d}{x}\right) \tag{33}$$

from a grain edge where d is the zirconia grain size.

For tetragonal zirconia, σ_{TEA} is a function of $E\Delta\varepsilon\Delta T$ where ΔT is $\left(T_{sr}-T\right)$, the difference between the temperature below which stress freezes, T_{sr}, and the temperature T at which the sample cools. For ZTC composites, σ_{TEA} is also a function of the zirconia content. For example, the magnitude of the internal stress in the zirconia grains embedded in an alumina matrix will increase with a decrease in zirconia content.

In the case of absence of internal stress, the critical transformation stress becomes:

$$\sigma_c^T = \left(\sigma_c^T\right)_0 = \Delta S^{t\to m}\frac{M_s^0 - T}{\varepsilon^T} \tag{34}$$

where M_s^0 is the transformation temperature in the absence of internal stress. Inserting equations (32), (33) and (34) into equation (31) and setting T equal to M_s, the M_s can be defined as:

$$M_s = M_s^0 - \left(\frac{\varepsilon^T E\Delta\alpha\Delta T}{\Delta S^{t\to m}}\right)f\left(\frac{d}{x}\right) \tag{35}$$

where $f\left(d/x\right)$ is the description of the stress concentration. Therefore, M_s exhibits a grain size dependence. When the transformation initiates on cooling, ΔT equals $\left(T_{sr}-M_s\right)$ and equation (35) becomes:

$$M_s = \frac{M_s^0 - \dfrac{\varepsilon^T E\Delta\alpha}{\Delta S^{s\to t}}T_{sr}f\left(\dfrac{d}{x}\right)}{1-\dfrac{\varepsilon^T E\Delta\alpha}{\Delta S^{s\to t}}f\left(\dfrac{d}{x}\right)} \tag{36}$$

or

$$M_s = \frac{M_s^0 - \beta T_{sr}}{1-\beta} \tag{37}$$

where β equals $\left(\varepsilon^T E\Delta\alpha/\Delta S^{t\to m}\right)f\left(d/x\right)$. To trigger an irreversible transformation simply by cooling the sample, the level of σ_i imposed over a region $2r$ in diameter within the grain must exceed the critical transformation stress. When $2r$ and T_{sr} are constants, M_s increases with increasing zirconia grain size because the internal stress changes with grain size, as shown in Fig. 19[37, 38]. In addition, increasing the internal stress with changes in composition, such as an increase in alumina content in ZTA, increases the rate at which M_s does with the growing of grain size.

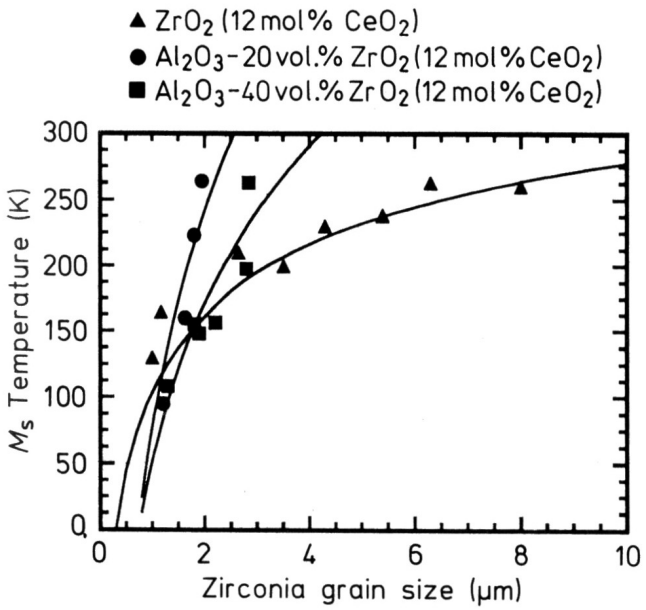

Fig. 19 Zirconia grain size vs. martensite start temperature. The martensite start temperature exhibits greater grain size sensitivity when zirconia is added to alumina, and grain size sensitivity increases with decrease in zirconia content[37].

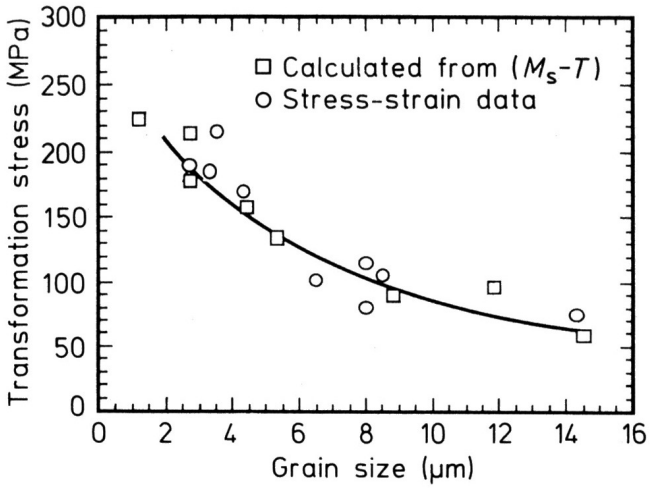

Fig. 20 The stress required to initiate the tetragonal to monoclinic transformation at 22 °C in the polycrystalline tetragonal zirconia (12 mol% CeO_2) ceramic vs. grain size[37].

According to equation (30), increasing the M_s to the test temperature T will decrease the measured critical transformation stress. Equations (35)-(37) reveal that increasing the tetragonal zirconia grain size will increase the M_s. The continuous decrease in the measured transformation stress with the increase in grain size for the 12 mol% CeO_2 polycrystalline tetragonal zirconia is shown in Fig. 20[37, 38]. In the figure, the change in the measured transformation stress with increasing grain size is compared to the transformation stress calculated from equation (30) using the measured M_s for each grain size. It is apparent that controlling the zirconia grain size can enhance the transformability of tetragonal zirconia grains, and the magnitude of the internal tensile stresses associated with grain size may be a major cause of the grain size effect.

3.2.4 Zirconia materials

There are different kinds of zirconia materials with different microstructures (Fig. 21) [39-41]. The commonly used zirconia in advanced ceramics applications includes partially stabilized zirconia (PSZ), zirconia toughened alumina (ZTA) and tetragonal zirconia polycrystals (TZP).

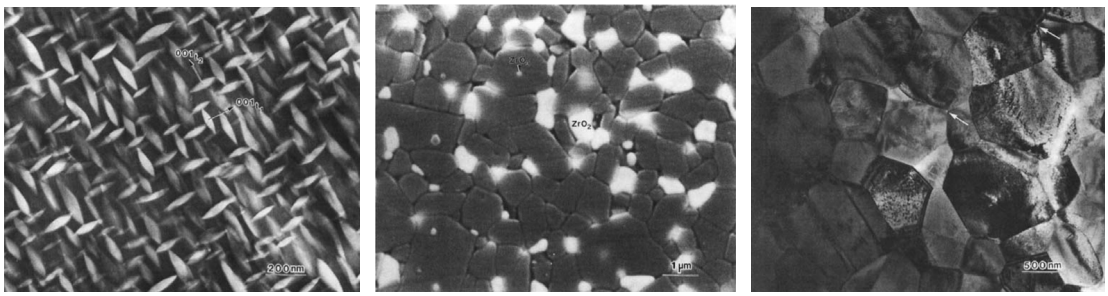

Fig. 21 Microstructural features of the three major categories of zirconia ceramics: (a) Mg-PSZ (b) ZTA (c) TZP[39].

3.2.4.1 MgO stabilized zirconia (Mg-PSZ)

For PSZ materials, typically MgO or CaO are used to stabilize zirconia, and have low solid solubility in zirconia. Commercial compositions for Mg-PSZ materials are in the range 8-10 mol% MgO-ZrO_2 (Fig. 22). This range is preferred because the solid-solution temperatures are too high when the compositions are below 8 mol% MgO, and the precipitation behaviour is not easily controlled. Compositions with >10 mol% MgO do not develop precipitate volume fractions that optimize the transformation-toughening capabilities of the system. Single-phase c-ZrO_2 can be achieved by heating above the phase boundary, and t-ZrO_2 is developed due to rapid cooling.

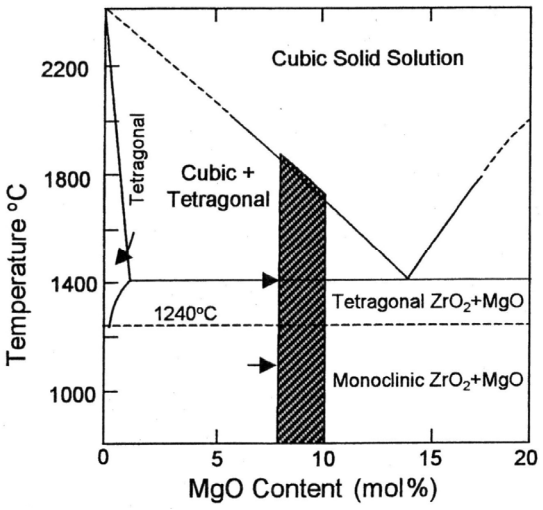

Fig. 22 Phase relations in the system ZrO_2-MgO [42].

The first step in processing involves a heat treatment in the cubic single-phase field, which stays for 2-4 hours at about 1800 °C depending on the composition. This is followed by a rapid cooling to promote homogeneous nucleation of very fine tetragonal precipitates. Reheating to 1400 °C and

holding isothermally leads to coarsening of the tetragonal particles by rejection of MgO into the cubic matrix. Coarser particles spontaneously transform to monoclinic symmetry during cooling. The microstructure of an optimally processed Mg-PSZ contains metastable tetragonal or monoclinic precipitates in a cubic matrix.

If the size of tetragonal precipitates is above critical value, they will transform to monoclinic phase either spontaneously or as a result of applied stress. This critical size depends on many factors including existing state (e.g. in a bulk matrix or powder form), temperature and composition.

The properties of commercial MgO-ZrO_2 at room temperature are improved by a further sub-eutectoid aging treatment at 1100 °C. Special heat treatment is applied to allow more heterogeneous nucleation of tetragonal particles, and then a thick grain boundary tetragonal film is produced, which then spontaneously transforms to monoclinic on cooling.

3.2.4.2 CaO stabilized zirconia (Ca-PSZ)

Many examinations of the CaO-ZrO_2 phase diagrams have been completed, but the version proposed by Hellmann and Stubican [43] is generally adopted, as shown in Fig. 23. The eutectoid temperature is about 1140±40 °C, and the content of CaO is about 17±0.5 mol%. A large cubic phase field exists, in conjunction with the eutectoid transformation, and allows a fully cubic structure to be attained by rapid cooling. This is the basis of calcia stabilized zirconia solid electrolytes. Specifically, the structure actually consists of the cubic phase, containing a fine distribution of homogeneously nucleated tetragonal particles, similar to Mg-PSZ.

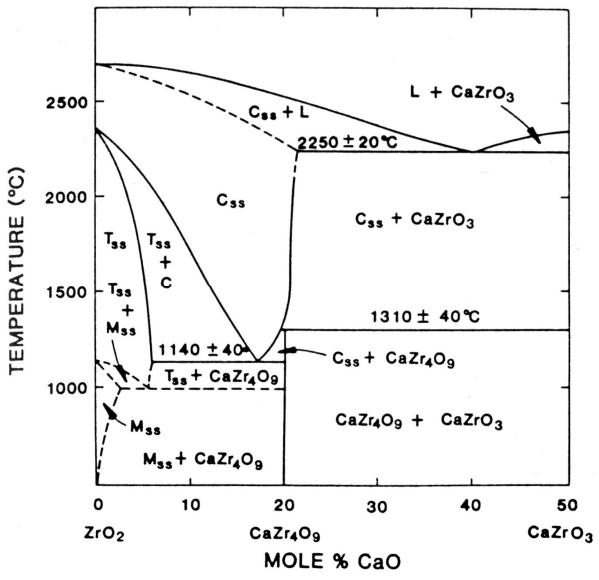

Fig. 23 Part of the ZrO_2-CaO phase diagram[43].

Commercially viable Ca-PSZ compositions are in the range of 3-4.5 wt% CaO-ZrO_2. 3.8 wt% (8.4 mol%) Ca-PSZ is formed at 1800° C, followed by a rapid cooling and subsequent reheating to 1300 °C for aging. The system is most sensitive to the t-ZrO_2 precipitate size and the corresponding level of metastability, a level which is strongly related to the mechanical properties.

Although Ca-PSZ was the first transformation-toughening system to be developed, little commercial application was predicted because of the sensitivity of microstructure to the isothermal tetragonal to monoclinic phase transformation at low and room temperature. This sensitivity leads to unstable aged materials, whereas greater versatility and better mechanical properties are achieved in the Mg-PSZ system.

3.2.4.3 Tetragonal zirconia polycrystals (TZP)

The important feature of the ZrO_2-Y_2O_3 phase equilibrium is the stabilisation of high temperature cubic and tetragonal phases at room temperature by the incorporation of Y^{3+} cations into the zirconia matrix. The widely accepted phase relationships found in high-temperature XRD experiments (Fig. 24) for the ZrO_2-Y_2O_3 system were given by Scott [44, 45]. Commercial Y-TZP materials are prepared in the composition range 1.75-3.5 mol% (3.5-8.7 wt%) Y_2O_3.

At 2000 °C the equilibrium is a two-phase mixture of tetragonal solid solution containing about 1 mol% Y_2O_3 and cubic solid solution containing about 4 mol% Y_2O_3; when this is quenched the tetragonal phase transforms to monoclinic and the cubic phase to tetragonal. At 1400 °C the equilibrium is again a two-phase mixture with the tetragonal phase containing about 2 mol% Y_2O_3 and the cubic phase containing about 9 mol% Y_2O_3. Upon quenching, the tetragonal phase transforms to monoclinic phase, but at this time the cubic phase contains sufficient yttria to retain that structure at room temperature, and it does not undergo any transformation.

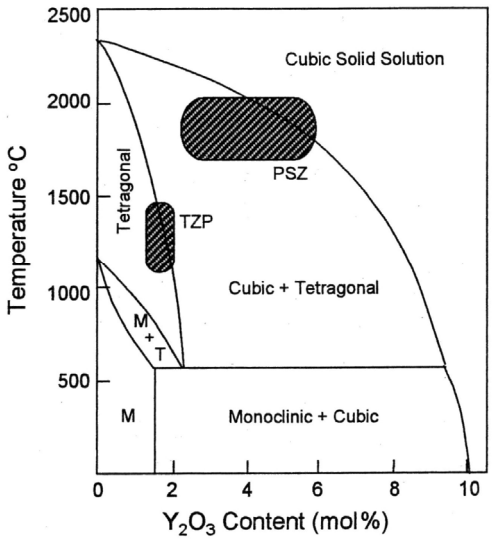

Fig. 24 Phase diagram of the zirconia-yttria system[44, 45].

TZP has a significant advantage over Mg-PSZ because with TZP sintering can be carried out at relatively low temperatures (1400-1550 °C compared to 1800 °C), bringing the production of TZP within the scope of existing furnaces in ceramic manufacturing plants.

A large cubic plus tetragonal phase field exists in the ZrO_2-Y_2O_3 system, permitting the formation of a PSZ structure. In this field, sintering must be conducted at higher temperatures, up to 1700 °C,

to ensure that sufficient yttria is added into a solution to generate fine and metastable tetragonal particles.

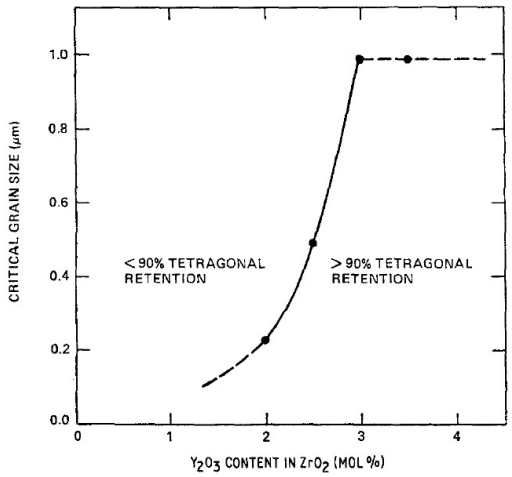

Fig. 25 Critical grain-size plotted against yttria content in tetragonal zirconia[46].

Similar to the critical precipitate size in PSZ materials, TZP ceramics exhibit a critical grain size dependant on the composition and the degree of mechanical constraint. Fig. 25 given by Lange [46] shows the relationship of critical grain size and the yttria content in tetragonal zirconia. High tetragonal-phase content cannot be achieved for the composition containing 1.5 mol% Y_2O_3, and the grain growth during sintering precludes an average grain size of less than 0.2 μm. The average critical grain size significantly increases between 2 and 3 mol% Y_2O_3. The composition containing 3.5 mol% Y_2O_3 contains a detectable amount of cubic phase, which indicates that this composition lies in the tetragonal plus cubic phase field above 1200 °C.

A major obstacle to TZP ceramics is the spontaneous surface transformation of tetragonal phase to monoclinic phase. This occurs if the ceramic is held at temperatures within the range of 150-2520 °C at times ranging from hours to days, conditions which can lead to severe degradation in strength. In the worst case, complete material disintegration occurs, which will be discussed in Chapter 3.2.7.6.

3.2.4.4 CeO_2 stabilized zirconia (Ce-TZP)

The ZrO_2-CeO_2 system given by Tani et al. [47] shows a very wide tetragonal phase field as shown in Fig. 26, and the preferred composition is 12 mol% Ce-TZP. The solubility limit of the tetragonal or cubic solid solution is about 18 or 70 mol% CeO_2, respectively, at 1400 °C, and decreases to about 16 or 80 mol% CeO_2, respectively, at 1200 °C. The tetragonal solid solutions decompose to monoclinic and cubic solid solutions by a eutectoid reaction between 1000 °C and 1100 °C, which is a higher temperature range than in the Y_2O_3 system. But due to the size of the tetragonal phase field, it is still possible to obtain a fully tetragonal structure as in the Y_2O_3 system. The solubility limit of the monoclinic or cubic phase is about 1.5 or 88 mol% CeO_2, respectively, at 1000 °C. The solubility limit of monoclinic solid solutions rarely changes from 1000 °C to 600 °C; however, that of cubic solid solutions decreases to about 97 mol% CeO_2 at 600 °C.

The common sintering temperature of Ce-TZP is about 1550 °C, another similarity to the Y_2O_3 system. The grain size after fabrication is within the range 2-3 μm, with microstructures of equiaxed grains similar to those of Y-TZP.

CeO_2-stabilized TZP materials display considerably greater moisture stability than Y-TZP under similar environmental conditions. In the case of similar fracture toughness value, the grain size is larger in Ce-TZP than in YTZP.

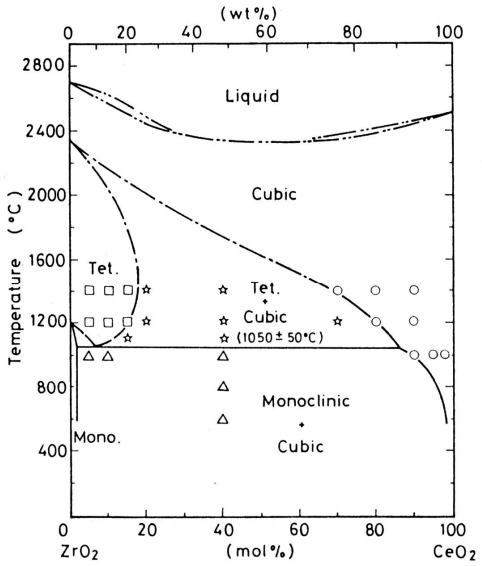

Fig. 26 ZrO_2-CeO_2 phase diagram[47].

The typical mechanical properties for commercial TZP are given in Table 3.

	Y-TZP	Ce-TZP
Mol% stabilizer	2-3	12-15
Hardness (GPa)	10-12	7-10
RT fracture toughness, K_{IC} (MPa*$m^{1/2}$)	6-15	6-30
Young's modulus (GPa)	140-200	140-200
Bend strength (MPa)	800-1300	500-800

Table 3. Typical physical properties of tetragonal zirconia polycrystals (TZP).

3.2.4.5 Zirconia toughened alumina (ZTA)

Zirconia is added into a variety of other oxide matrices such as mullite, spinel, cordierite, zircon and MgO as a toughening agent. ZrO_2-toughened Al_2O_3 (ZTA) is the most commonly exploited dispersed zirconia ceramics (DZC). This material demonstrates that the inclusion of unstabilized zirconia can lead to retention of tetragonal zirconia in the sintered product, if the particle size is small enough. The toughening mechanism mainly involves transformation and microcrack formation.

Less than 20 vol% zirconia unstabilized particles are typically used, although subsequent work has attempted to increase the zirconia content by partial stabilization of the zirconia with Y_2O_3, CeO_2 or TiO_2 by Lange [48]. Unstabilized ZTA can have strengths of 1200 MPa and toughnesses of 16 $MPam^{1/2}$ with about 15 vol% ZrO_2, compared to the values of 600 MPa and 4 $MPam^{1/2}$, respectively, for typical dense alumina.

ZTA is utilized primarily for grinding media, engine components and metal-cutting-tool applications, for which the zirconia addition takes the unstabilized or TZP form. The primary difference between the unstabilized form and TZP form of the ZTA system is that the former relies on microcrack toughening, whereas the latter involves transformation toughening as the primary toughening mechanism.

3.2.5 Toughening mechanisms

Transformation toughening occurs when tetragonal phase transforms to monoclinic phase for zirconia ceramics, with a volume expansion of 4-5%. The phase transformation provides the foundation for two toughening mechanisms that can interact with or complement each other.

3.2.5.1 Microcracks

Microcrack toughening in brittle materials arises from the energy dissipation as the microcracks nucleate and grow in the crack tip stress field [49, 50]. Localized stresses initiate from the volume effect in transforming from tetragonal to monoclinic phase. The shear stress involved in the martensitic transformation of tetragonal phase is released in the matrix, and then the microcracks nucleate at the grain boundaries of the transformed monoclinic grain, as shown in Fig. 27. Microcracks around a crack tip can increase toughness by the dissipation of the stress when they propagate into macrocrack, and also by their interaction with the crack tip stress field. These effects reduce the local stress concentration at the crack tip, which in turn shields and eventually toughens the matrix.

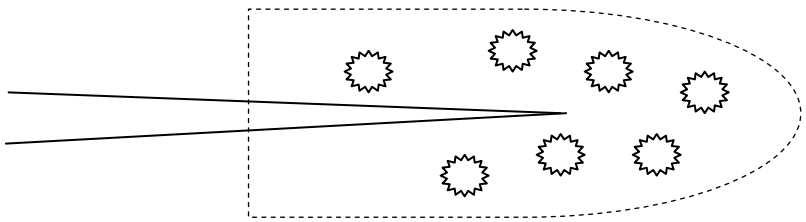

Fig. 27 Schematic diagram of transformation toughening by microcracks.

Zirconia particle size is an important factor in microcrack toughening [51, 52]. It is necessary to have a minimum size, which should be large enough to transform to the monoclinic phase and to induce a microcracked zone when the stress is applied. This critical value is related to the

interfacial energy, Young's modulus and the dilatational strain. However, at the same time, the particle size cannot be large enough to limit the size of the microcracks.

Thus, the volume or the density of the induced microcracks, as well as the orientation, are very important [51, 52]. For such reasons, the toughening increases with the increase in the density of microcracks, but will decrease with too-high density. The anisotropic distribution of microcracks also affects the elastic properties, such as Poisson's ratio, of the material [53].

3.2.5.2 Stress-induced transformation toughening

The metastable tetragonal zirconia will transform to the thermodynamically stable monoclinic form under an external tensile stress around a crack tip, which is known as stress-induced transformation toughening. In the matrix, the propagated macrocrack relaxes a zone around itself. The relaxed stress induces the transformation to the monoclinic state to stabilize the tetragonal phase (Fig. 28). Then the local crack tip stress intensity is reduced and thus the driving force for crack propagation, so increasing the effective toughness of the material.

This transformation toughening mechanism can be characterized by the change in stress intensity factor, and the crack tip shielding can only occur when the crack tip stress intensity is less than that due to the applied stress.

Effective transformation toughening requires the retention of the maximum amount of tetragonal zirconia at the current temperature. In some cases, the transformability is generally regarded as the ability of tetragonal zirconia to transform to monoclinic in the crack tip stress field [54, 55].

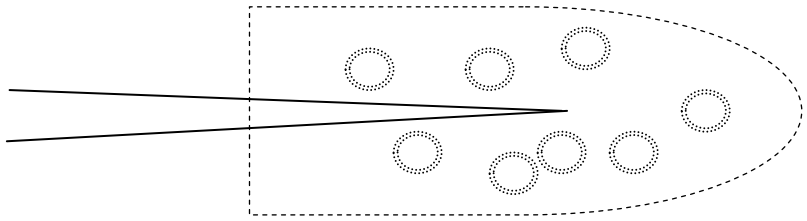

Fig. 28 Schematic diagram of stress-induced transformation toughening.

3.2.6 R-Curve

The phenomenon of resistance to crack growth, or toughness, which increases during crack extension, is called the resistance (R) curve. The R-curve typically consists of three stages (Fig. 29)[40]: (1) Frontal zone. For purely dilatational transformation, there is no contribution from the frontal zone to the crack-tip field, and, thus, the initial crack growth occurs without toughening. (2) Partially-developed zone. When the transformation zone extends to the crack surface, the crack tip shielding will occur, and partial transformation from tetragonal to monoclinic occurs. (3) Extended transformation zone. The crack tip shielding reaches an asymptotic maximum in the formed transformation zone, inside which the maximum number of tetragonal particles are assumed to have transformed to monoclinic phase [40, 51, 54, 56].

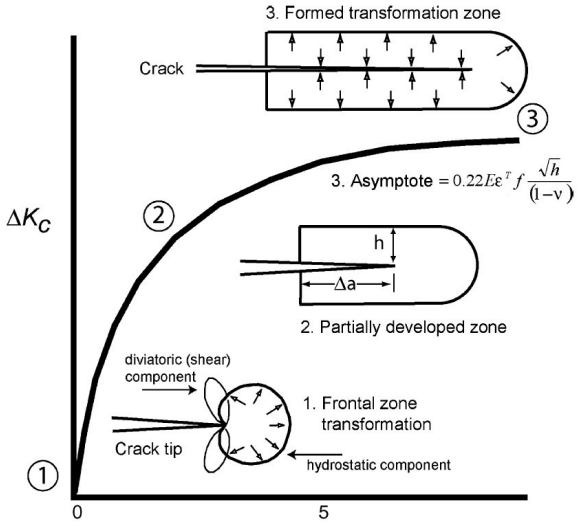

Fig. 29 Schematic representation of R-curve in transformation toughened ceramics[40].

McMeeking and Evans gave an analytical model to predict the toughness increment [55]:

$$\Delta K_c = 0.22 f E \varepsilon^T \sqrt{h}/(1-\nu) \tag{38}$$

in which E is Young's modulus, f is the volume fraction of the transformed material, ε^T is the dilatational strain associated with the transformation, h is the transformation width, and ν is the Poisson's ratio. From the studies of Mg-PSZ by Marshall et al. [57], the shape of the transformation zone ahead of the crack tip is approximately semicircular, and the volume fraction of the transformation from tetragonal to monoclinic phase is not uniform within the transformation zone.

The built model above is helpful to relate the toughness increment directly to the characteristics of the transformation, such as volume expansion, shear strain, and transformation zone size; it is also helpful to explain the R-curve behaviour, which presents the increase in toughness with increasing crack length.

3.2.7 Phase transformation by external influence

3.2.7.1 Isostatic high-pressure investigations

Since the toughening mechanism of zirconia is explained by the phase transitions induced by stress field, the high-pressure behaviours of zirconia have been widely investigated. Much research has been done with contradictory results about the transformation pressures and crystal structures [58-64]. The difficulties of high pressure experiments cause such varying results. XRD, instead of neutron diffraction, is impossible to give a detailed structure determination of the oxygen network, because the oxygen atoms have a very small x-ray scattering factor. Such results can also be attributed to the fact that zirconia may or may not be doped [59, 61, 62].

Pressure-temperature phase diagram of zirconia is shown in Fig. 30 [64]. The lower arrow corresponds to experimental excursion performed using Raman spectrometry on pure monoclinic zirconia, and the higher arrow corresponds to the high-pressure excursion for room-temperature nanocrystalline zirconia. This will be discussed in detail in Chapter. 3.3.5.3.

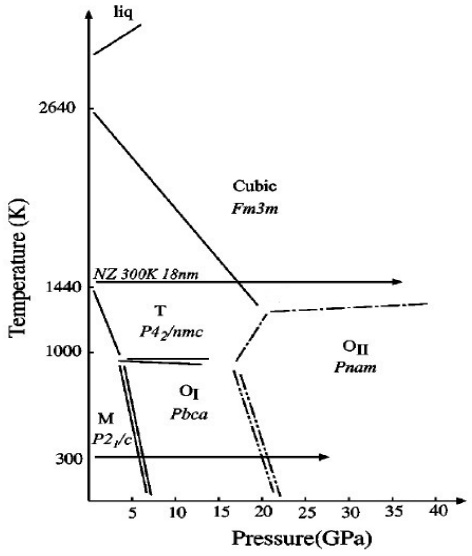

Fig. 30 Pressure-temperature phase diagram of zirconia[64].

Monoclinic zirconia (baddeleyite) transforms to two distorted fluorite (CaF_2) type phases by compression of 3-4 GPa. Depending on the temperatures, an orthorhombic phase (O_I) below 600 °C or a tetragonal phase over 600 °C will occur. Both transform into O_{II}, with a cotunnite ($PbCl_2$) type of structure above 12.5 GPa, which is stable to a pressure of 100 GPa and a temperature of 2500 K. No post-cotunnite phase was observed after that [59, 61, 62]. Phase boundaries between the O_I and O_{II} were determined, which is almost independent of temperature by Ohtaka et al. [59, 61, 62].

A tetragonal structure, which is different from the high-temperature tetragonal phase, was reported for the high-pressure phase observed above 4.4 GPa for zirconia [60]. At pressure higher than 16.6 GPa, a different orthorhombic phase with the cotunnite type structure was also reported by Block et al. [60]. However, from Arashi et al. [58], a different conclusion was reached, where the crystal structure for high-pressure phase observed above 13 GPa is of the cotunnite type, but has a lower symmetry in orthorhombic phase (O_{II}). A new phase occurs over 35 GPa, and is stable until 60 GPa, which was regarded as tegtragonal high-pressure phase.

Leger et al. [64] used in situ powder XRD to investigate the phase transformations and the pressure dependence of crystal structures at room temperature. At about 10 GPa, the monoclinic I (baddeleyite) transforms to O_I, which is stable until 26 GPa, and a new phase O_{II} occurs. Over 42 GPa, a third phase occurs with tetragonal symmetry.

Partial back conversion to the lower-pressure phases was observed during quenching experiments. The cotunnite-, $PbCl_2$-type, structure proposed for O_{II} appearing in zirconia could not be detected by Leger et al. [64].

Undoped tetragonal nanocrystallized zirconia at room temperature was investigated by Raman spectrometry under high pressure by Bouvier et al. [63]. A continuous transformation towards the ideal fluorite cubic structure was observed, and the zirconium atoms reached this cubic structure

as soon as 8 GPa. The pressure of the oxygen atoms to achieve the ordered fluorine structure should be over 30 GPa (Fig. 30).

3.2.7.2 Ferroelastic toughening

Reorientation of the (002) peak in 2-mol% ytrria-stabilized tetragonal ZrO_2 using XRD polycrystals after mechanical and thermal treatments and compressive stress was studied by Kitano et al. [65]. The domain switching was observed by compressive stress above 70 MPa due to a preferred transformation of the tetragonal phase, which led to a remnant c-axis orientation normal to the compressive direction. Tetragonal grains with their a-axis parallel to the stressing direction more readily transform than those with the c-axis.

This phenomenon in Zirconia is known as ferroelasticity. Toughening by this mechanism can occur in addition to transformation toughening and also explains high toughness of some zirconia, which exhibit no transformation to the monoclinic form [66]. Ferroelastic toughening differs from stress-induced transformation in that there is no change in crystal structure, but a reorientation of the ferroelastic domains. The microstructure in polydomain tetragonal zirconia was studied using high-voltage electron microscopy by Baither et al. [67], and in situ deformation experiments by a transmission electron microscope were completed by Baufeld et al. [68]: both of which provided insight into the process of domain switching.

Hysteresis on Ce-TZP was measured by Virkar and Matsumoto [66] in compression by attaching a strain gage and continuously recording strain vs. stress using XRD, shown in Fig. 31. Rapid increase in strain was noted at a stress of about 1.65 GPa. When the specimen was completely unloaded, there was a permanent compressive strain of 0.64%.

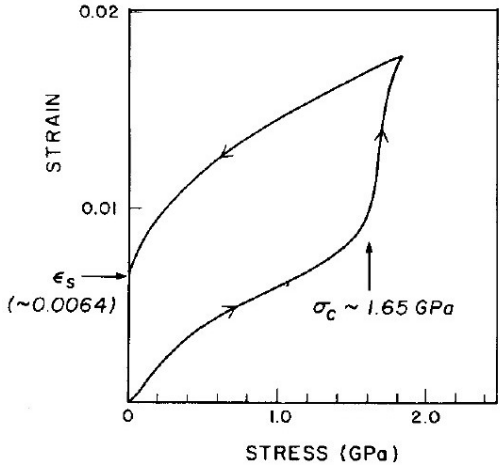

Fig. 31 Partial hysteresis loop measured on Ce-TZP in compression by a strain gage technique[66].

Srinivasan et al. [69] investigated the ferroelastic phenomenon in 4-mol% Y_2O_3 doped zriconia single crystals at room and high temperatures. XRD indicated that ferroelastic domains underwent reorientation in compression. Upon observing fracture surfaces of notched specimens, it was clear that domain reorientation had occurred and no monoclinic phase was observed on fracture or ground surfaces. These results indicated that ferroelastic domain switching could occur during fracture and may contribute to toughness.

Chan et al. [70] studied the detailed microstructure of domain switching in polydomain tetragonal zirconia single crystals under a unidirectional compressive stress at 1000 °C and 1400 °C. Dark-field imaging of the three {112} tetragonal twin variants in a [111] zone indicated that two sets of twin variants grow at the expense of the third set under compression. The diminishing variant is the one with its c-axis parallel to the compression axis. Since domain reorientation is an energy-absorbing process, its occurrence around the crack surface may absorb work from the loading system and therefore enhance the fracture toughness of the material.

3.2.7.3 Flexural testing

Four-point-bend flexural testing (Fig. 32) done by Hannnink and Swain [71] of a single-phase tetragonal zirconia polycrystal containing 12 mol% cerium dioxide showed the transformation from tetragonal to monoclinic phase under deformation and fracture. At an applied stress of 295 MPa on the tensile surface of flexure bars, two bands nucleated from a localized stress concentration site at one edge and propagated completely across the specimen, while two more bands extended to about half the specimen width. These partially propagated bands extended across the specimen, other bands initiated with increasing loading, and the specimen finally fractured at about 380 MPa. This stress-induced transformation implied that the system requires a continual application of stress to complete the transformation and hence the tetragonal and monoclinic phases are near equilibrium at room temperature, and there exists no driving force to complete the transformation once nucleated.

Fatigue properties of 9 mol% CeO_2-stabilized tetragonal zirconia were studied by Grathwohl and Liu [72] with different grain sizes. The transformation from tetragonal to monoclinic phase started as early as at about 50% of the ultimate strength, and the size of the transformation band increased with increasing load, except in the case of the specimen with the smallest grain size. The strength values ranged from 350 to 570 MPa, and the critical stress for stress-induced transformation ranged from 230 to 290 MPa.

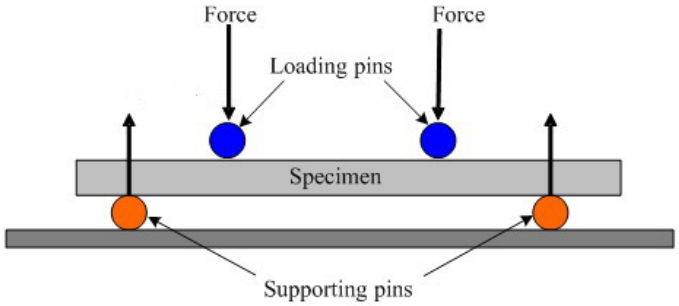

Fig. 32 Schematic diagram of four-point-bend system.

3.2.7.4 Phase transformations and indentation

Indentation techniques are commonly used to study the hardness and toughness of different ceramics, and involve elastic and plastic deformations, cracks and phase transformations. A

review of indentation fracture theory about development, principles and limitations of different indenter geometries is given by Ostojic and McPherson [73]. The influence on the behavior of cracks coming from anisotropy, particle size, environment and residual stress effects is also discussed.

Transformation zone size of single phase zirconia-3.5% yittria was presented by Clarke and Adar [74] using Raman spectroscopy to show that a partial monoclinic transformation was found 12 μm away from a radial crack in a Vickers indentation The size of the transformation zone was approximately 5 μm.

Vickers indent-induced cracks of yittria stabilized zirconia were studied by Kaliszewski et al. [75], who showed that the plastic zone directly beneath the indent is uncracked, and a significant portion of the plasticity induced by indentation occurs by martensitic transformation. 3 and 4 mol% yittria stabilized zirconia was used to research the growth of indentation cracks in four-point bend tests by Dransmann et al. [76]. Both materials exhibited steeply rising R-curves, and the magnitude of the toughness reflected the fraction of tetragonal grains which contributed to transformation toughening. Magnesia partially-stabilized zirconia was studied by Dauskardt et al. [77], in particular the transformed zones surrounding cracks.

The martensitic tetragonal to monoclinic transformation in 3Y-TZP, induced with Vickers indentation of 500 N, was studied with Raman spectroscopy by Behrens et al. [78]. The distribution of monoclinic phase on a surface a few micrometers below the base of the indent is shown in Fig. 33.

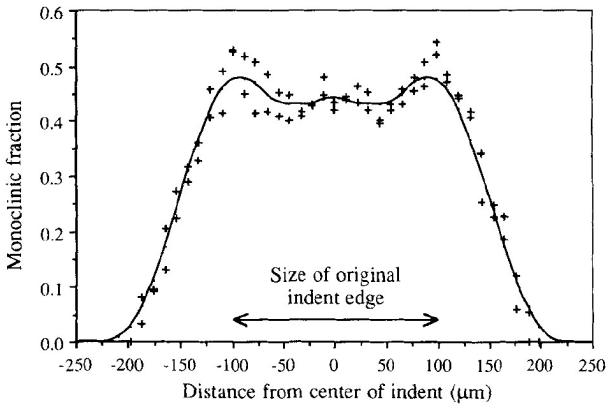

Fig. 33 Extent of transformation under a polished-away indenter[78].

The zone of stress-induced transformation is about 400 μm in diameter. Directly underneath the indent, in the core, the content of monoclinic phase is about 43%. The maximum of monoclinic fraction at a distance of about 100 μm from the center of the indent is about 48%, approximately the position of the edge of the indent at the original free surface. The content of monoclinic phase gradually decreases to zero within a zone extending about 100 μm from the indent edge.

The extent of transformation is slightly lower in the hydrostatically-compressed zone directly below the indent than it is in the surrounding area. This is most likely because the tetragonal to monoclinic phase transformation is more easily induced by tensile and shear stresses than by the compressive stresses, due to the transformation dilatation of about 4%.

The significant changes in the monoclinic fraction annealing at 400 to 1300 K are shown in Fig. 34[78]. Annealing up to 500 K increases the size of the transformation zone and the amount of

monoclinic phase within the zone. Further transformation occurs with 600 K but the monoclinic content in the core decreases slightly. Higher temperature annealing causes gradual decreases in the monoclinic content; above 900 K results in a lower monoclinic content than in the as-indented sample. No monoclinic zirconia remains after the 1300 K annealing, which means the reverse monoclinic to tetragonal transformation occurred at higher temperatures.

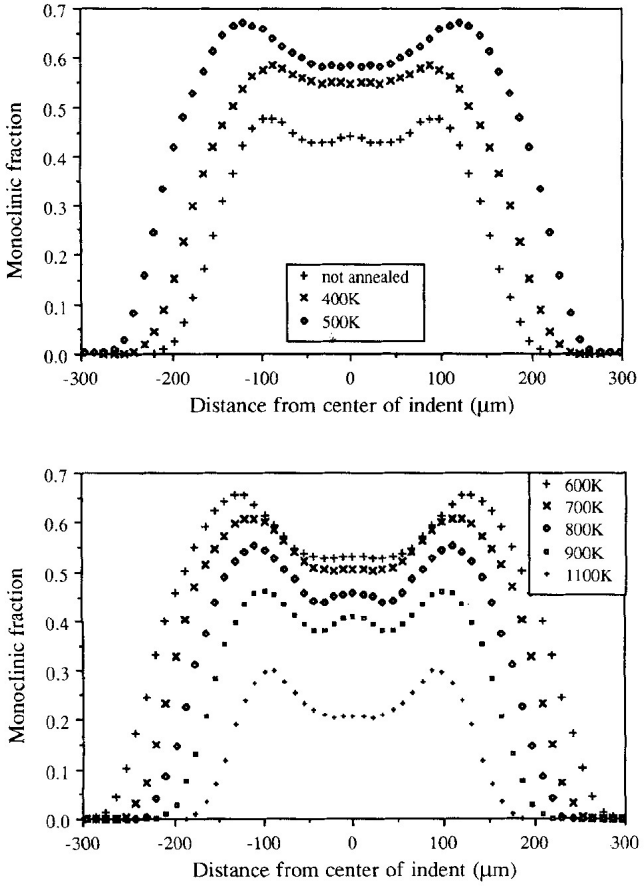

Fig. 34 Extent of transformation (fitted curves) under polished-away indents annealed for 75 min at various temperatures[78].

3.2.7.5 Scratch and machining damage

Zirconia-based ceramics have good wear-resistance properties, which accounts for its wide use in engineering applications, including many kinds of engine components and biomechanical components. In such cases, contact, scratch and wear damage are critical factors in lifetime performance.

Contact and scratch damage in zirconia-based ceramics: Mg-PSZ, Y-TZP and Ce-TZP were investigated by Lee et al. [79]. Upon contact damage of each material with a tungsten carbide sphere indenter, all specimens showed a residual depression at the contact center on the top surface. There were faint traces of incipient ring cracks in all specimens. Subsurface damage depended strongly on the material, with surface rumpling characteristic of phase transformations. The Mg-PSZ was the most transformable of the three, Y-TZP the least, and Ce-TZP intermediate. Mg-PSZ was characterized by limited diffuse subsurface microcracks, Y-TZP by more well-defined surface ring cracks, and Ce-TZP intermediate. All exhibited a plastic-brittle transition in

scratching. Mg-PSZ showed the least smooth scratch track, with extensive microcracking. Y-TZP showed the smoothest track, and lowest wear rate, and Ce-TZP was intermediate. Bending strength properties in the scratching of Mg-PSZ, Y-TZP and Ce-TZP as a function of load is shown in Fig. 35. In the Mg-PSZ and Ce-TZP, strength fell off slowly, indicating high damage tolerance. Y-TZP, on the other hand, showed a typical brittle response: no perceptible degradation in initially high strength up to about 80 N, but with subsequent abrupt drop-off at higher loads.

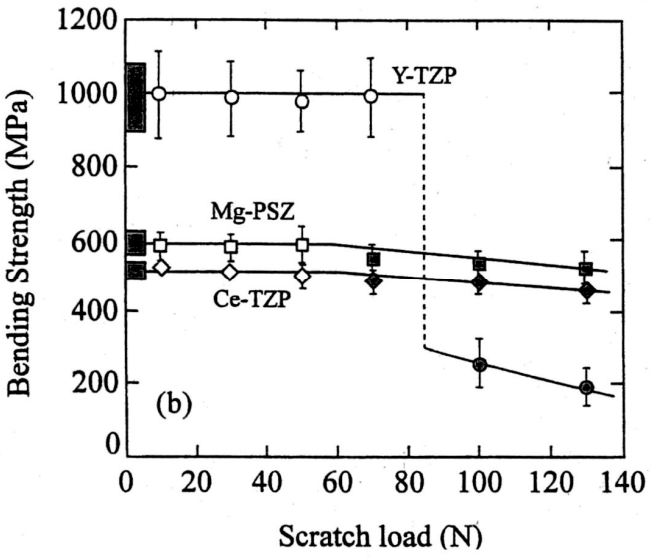

Fig. 35 Wear and strength properties in scratching of Mg-PSZ, Y-TZP, and Ce-TZP as a function of load[79].

The effect of grain size on scratch damage in Y-TZP ceramics was examined by Lee et al. [80]. For the fine Y-TZP sample with grain size of 0.3 μm, the damage appeared to be fully plastic along the entire scratch groove over 125N, indicating that plastic deformation predominates. Fine Y-TZP also showed a smoother surface track with microcracking with a load of 100N. Large grains lead to a rougher scratch track and a higher material removal rate.

The wear characteristics associated with a scratch of 4.7 wt% yttria stabilized zirconia were investigated as a function of sliding speed and normal load in dry air, deionized water, purified paraffin oil and a commercial formulated oil by Lee et al. [81]. In mild-wear regions, plastic deformation and microcutting were dominant wear mechanisms, while thermal-shock-induced brittle fracture resulted in severe wear in the high speed regions. Moisture-induced destabilization of the material can be investigated specifically under water-lubricated conditions. In humid air, an increase in relative humidity reduces the friction coefficients of zirconia, and the wear rates increase when the sliding velocity increases in water [82].

The steady state coefficient of friction of the Y-TZP strongly depends on the grain size and the toughness of the zirconia materials, tougheness increasing with an increase in tetragonal grain size and concomitant toughness. The tetragonal to monoclinic phase transformation seemed to cause extensive microcracking at the worn surfaces [83].

The effect of temperature on surface damage caused by scribing was investigated by Asif et al. [84]. A 150 °C diamond conical indenter was loaded on the samples with 100 N and a sliding speed of $1.3*10^{-4}$ m/s. The hardness of both 3Y-TZP and Mg-PSZ first increased from -196 °C to 25 °C and then decreased with increasing temperature. The track width was minimal at room temperature. For 3Y-TZP the friction coefficient increased with temperature, while Mg-PSZ had a

minimum friction coefficient at room temperature. The peak monoclinic percentage of Mg-PSZ decreased from -196 °C to 25 °C, then increased up to 200 °C and once again decreased. For TZP the peak monoclinic percentage increased with increasing temperature.

The production of notch cuts is very similar to scratching because both cause non-isostatic stress in the specimen. Nagarajan et al. [85] studied such notch cut on 3Y-TZP. The broadness and distortion of the tetragonal phase peak corresponding to the unannealed as-received specimen may be due to the inhomogeneity of the residual stress introduced during the processing. This inhomogeneity is removed when the specimen is cut or annealed. The enhancement of the monoclinic phase after annealing occurs because of low temperature degradation, which will be discussed in detail in the next chapter.

The transformation caused by the notches is more likely caused by the removal of the compressive stresses, which keep the zirconia in the metastable state in the matrix, rather than by the appearance of shear stresses.

3.2.7.6 Low temperature degradation

The most positive aspects of the transformation toughening ability of zirconia ceramics result in high strength and toughness, as well as reduced brittleness. Furthermore, much attention has also been paid to another characteristic of zirconia: low temperature degradation (LTD), which leads to the reduction of strength and fracture toughness, along with microcracks and macrocracks.

The low temperature degradation has such features as follows:
(1) The reaction occurs at low temperatures between 100 °C to 500 °C.
(2) The tetragonal to monoclinic transformation progresses from the surface to the interior.
(3) Water of water vapour plays a great role in the degradation.
(4) Smaller grain size and higher stabilizer content can retard the transformation.

Until now there existed no study conclusive enough to explain the degradation mechanism, although several main models have been proposed by different researchers.

Sato and Shimada [86] studied the phase changes and the microstructure resulting from yttria-doped tetragonal zirconia polycrystals annealed between 65 °C and 120 °C using XRD and SEM. They argued that water reacts with Zr-O-Zr bonds at the crack tip and Zr-OH bonds are formed. The strain which acts to stabilize the tetragonal phase is released on the surface along the growth of preexisting flaws, and consequently the transformation to monoclinic phase happens. Similar to water, the nonaqueous solvents with lone-pair electron orbital also accelerate the degradation.

Another model proposed by Lange [87] suggested that there is a reaction between the water vapor and yttria that produces clusters of small (20 to 50 nm) crystallites of $Y(OH)_3$. The water vapor draws out sufficient amounts of yttrium from a small volume element on the surface of the grain, which destabilises the material and causes the transformation to monoclinic phase. By further depletion of yttrium the monoclinic nucleus continuously grows, and reaches a critical size where it can spontaneously grow without further yttrium diffusion. If the transformed grain is large enough, microcracks will be produced, providing a path for water to penetrate, and leading to further spontaneous transformation. If the transformed grain is smaller than the critical size

necessary for microcracks to occur, then the transformation will be limited by the long-range diffusion of yttrium to the surface.

The third model given by Yoshimura et al. [88] can be described in four steps:
1st step: The chemical adsorption of water at the surface.
2nd step: The formation of Zr-OH and/or Y-OH at the surface at which points stressed sites are created.
3rd step: The accumulation of the stresses by the migration of OH^- at the surface and in the lattice, to prepare nucleating defects.
4th step: The nucleation of monoclinic phase in the tetragonal grains; then the t-m transformation yields micro- and macro-cracking.

This phenomenon is supported by the infrared absorption studies and the changes in lattice volume and weight. The increases in weight suggested that about 60% oxygen vacancies were occupied by OH^-.

A varied model by Guo [89, 90] consists of five steps: (1) chemical adsorption of water on the zirconia surface, (2) reaction of water with O^{2-} on the zirconia surface to form hydroxyl ions OH^-, (3) penetration of OH^- into the inner part by grain boundary diffusion, (4) filling of oxygen vacancies by OH^- ions, and therefore the formation of proton defects, and (5) occurrence of a tetragonal to monoclinic transformation when the oxygen vacancy concentration is reduced to the extent where the tetragonal phase is no longer stable. This mechanism requires only the diffusion of proton defects at low temperatures, which are a few orders of magnitude higher than that of oxygen vacancies, supported by the experimental results from X-ray photoelectron spectroscopy, infrared adsorption spectroscopy and Fourier transform infrared transmission spectrometry.

The study from Schmauder and Schubert [91] emphasized that the transformation begins mostly at grain corners, where residual tensile stresses are the largest. Transmission electron microscopy revealed that protruding grains at the surface of Y-TZP specimens do not transform under corrosive conditions (250 °C, humid atmosphere) even after an annealing time of 168h.

To retard the low temperature degradation, one important parameter is density [92]. Low density with the presence of open porosity offers a path for water molecules to easily access the bulk of the material, resulting in aging both on the surface and the internal surfaces. In such cases, the material rapidly loses its cohesion, and experiences dramatic decrease in mechanical properties.

Grain size and dopant concentration are also crucial for degradation [92-96]. Lower sintering temperatures result in smaller grain size, and below a critical grain size no transformation occurs. However, decreases in the grain size also lead to a decrease in toughness and slow crack propagation threshold, mostly because of less efficient phase transformation toughening. Increasing the dopant concentration can also retard the degradation. But cubic phase increases with an increase in yittria content, which has larger grain size, and pumps the yittria out of the tetragonal phase. The tetragonal grains neighboring the cubic phase are therefore depleted in yttria and act as preferential nucleation sites for aging.

The introduction of other compounds is also possible to overcover the degradation [94]. The formation of the monoclinic phase from the tetragonal phase decreased with increasing concentration of dispersed alumina. Roy et al. revealed that Mg-PSZ has excellent resistance to environmental degradation, and is also resistant to roughening and loss of hardness [97]. Zirconia-toughened alumina is regarded as the most promising zirconia, which offers an exceptional balance between slow crack growth resistance and aging resistance [92].

3.2.7.7 Transformation by ball milling

Different oxides are added into zirconia at higher than 1000 °C to retain high temperature cubic phase at room temperature. However, cubic or tetragonal single-phase can be synthesized by high energy ball milling [98]. 10 mol% Y_2O_3 and 25 mol% CoO were investigated to show the phase transformation. Incomplete transformation from monoclinic to tetragonal was observed after 3 hours of milling of pure zirconia. The Raman spectrum of cubic structure with a broad band at about 600 cm^{-1} can be seen after 3 hours' milling of 10 mol% Y_2O_3, while for 25 mol% CoO is entirely tetragonal structure.

The advantage of mechanical alloying is to provide a simple method for the synthesis of nanocrystalline zirconia doped with various oxides, thus avoiding high temperature sintering processes.

3.3 Raman spectroscopy and the application of zirconia

3.3.1 Overview

Very early research between 1880 and 1910 indicated that molecules possess a very complex and special vibrational phenomenon. In 1923 Smekdal was one of the first scientists to predict that molecules could scatter light inelastically. He also suggested that molecular polarisability often changes as particular vibrations occur. This led him to propose that the shift in frequency between the incident and scattered light would be characteristic of molecular vibrations. In 1928, the Indian physicist C. V. Raman discovered this radiation effect, which was named after him. This was reported almost concurrently by L. Mandelstamm. Raman received the Nobel Prize in 1930 for his work on the scattering of light and for the discovery of the effect named after him.

Early instruments used a mercury arc lamp as the light source, a spectrograph to separate the different colours of light and photographic film to record the spectrum. Photographic film was replaced by photomultiplier tubes for detection, providing superior radiometric accuracy and greater ease of use. During the 1960's the laser replaced the mercury arc as the excitation source and Raman microscopy was introduced in the 1970s.

During the early 1990's one major advance for Raman spectroscopy was the use of charge-coupled device (CCD) detection with dispersive Raman spectrographs. With CCD detectors Raman spectroscopy became a faster technique, which reduced the collecting time to a few seconds or even less. CCD detection still maintained the radiometric accuracy and ease of use offered by the photomultiplier.

Instrument manufacture continued developing better filters, lasers, and gratings. During the 1990's it became possible for scientists and engineers to use high performance Raman instruments to solve analytical problems, despite little or no expertise in Raman spectroscopy.

3.3.2 Principal

Raman Spectroscopy is a non-destructive technique of probing a material with a laser light source and obtaining the Raman spectra of the material. When a beam of light interacts with a material, part of it is transmitted, part is reflected, and part is scattered.

The Raman effect is based on molecular deformations in electric field determined by molecular polarisability. The laser beam can be considered as an oscillating electromagnetic wave with electrical vector E. Upon interaction with the sample, it induces electric dipole moment P=aE, which deforms molecules. Periodical deformation molecules begin vibrating with characteristic frequency u_m. The amplitude of vibration is known as nuclear displacement. In other words, monochromatic laser light with frequency u_0 excites molecules and transforms them into oscillating dipoles. Such oscillating dipoles emit light of the following three frequencies (Fig. 36):

i. Elastic Rayleigh scattering: A molecule absorbs a photon with the frequency u_0. The excited molecule returns back to the same basic vibrational state and emits light with the same frequency u_0 as an excitation source. Over 99% of the scattered radiation experiences this phenomenon. This type of signal is useless for practical purposes of molecular characterization.

ii. Stokes frequency: A photon with frequency u_0 is absorbed by a Raman-active molecule which is in the basic vibrational state. Part of the photon's energy is transferred to the Raman-active mode with frequency u_m and the resulting frequency of scattered light is reduced to $u_0 - u_m$. This is the most often used in Raman spectroscopy.

iii. Anti-Stokes frequency: A photon with frequency u_0 is absorbed by a Raman-active molecule, which at the time of interaction is already in the excited vibrational state. Excessive energy of an excited Raman-active mode is released, the molecule returns to the basic vibrational state and the resulting frequency of scattered light rises to $u_0 + u_m$. This is only used in specialized research domains.

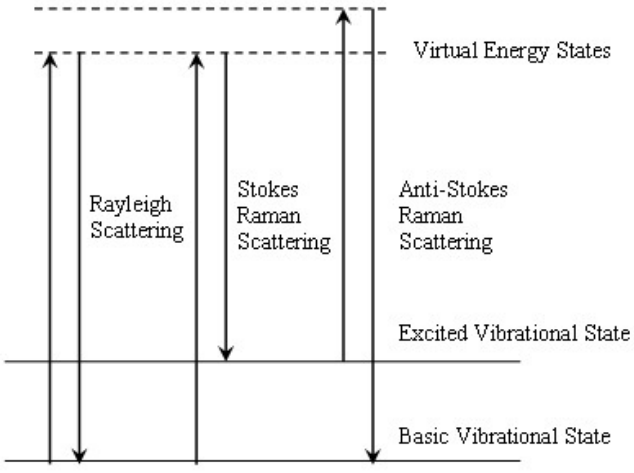

Fig. 36 Energy level diagram of Rayleigh scattering, Stokes Raman scattering, and anti-stokes Raman scattering.

Only about 0.001% of the incident light produces an inelastic Raman signal with frequencies $u_0 \pm u_m$. Because spontaneous Raman scattering is very weak, special measures should be taken to

distinguish it from the predominant Rayleigh scattering. Instruments such as notch filters, tunable filters, laser stop apertures, and double and triple spectrometric systems are used to reduce Rayleigh scattering for obtaining high-quality Raman spectra.

A Raman spectrum is a plot of the intensity of Raman scattered radiation as a function of its frequency difference from the incident radiation (usually in units of wavenumbers, cm^{-1}). This difference is called the Raman shift. Additionally, because it is a difference value, the Raman shift is independent of the frequency of the incident radiation. As an example, Fig. 38 shows the Raman spectrum of Baddeleyite from Sukulu, Uganda, extracted from residual soil overlying carbonate.

3.3.3 Raman instrumentation

Raman spectroscopy was not successful at its beginning due to poor availability of monochromatic light sources and data acquisition devices. With today's lasers, charge coupled device, and computer aided data acquisition devices it is a state-of-the-art technique. A typical Raman system consists of four major components (Fig. 37):

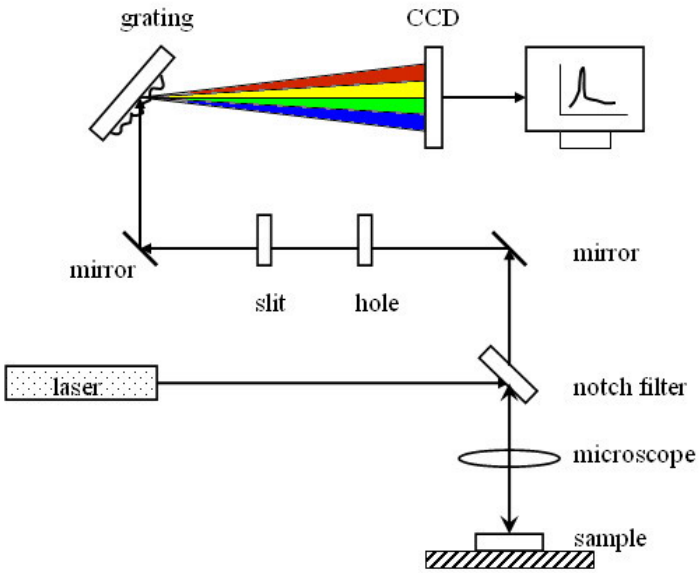

Fig. 37 Schematic diagram of a Raman spectrometer.

i. Excitation source (Laser): Raman offers the possibility to select the optimal laser excitation wavelength to permit the recording of the best Raman information. Nowadays, laser lines of ultra-violet, visible, or infrared can be chosen, with voltage from microwatts up to several Watts. In conventional Raman spectroscopy, visible lasers are used (e.g., Ar+, Kr+, He-Ne, diode) to stimulate the molecules to high-energy "virtual" states of excitation.

ii. Wavelength selector: Since spontaneous Raman scattering is very weak, the main difficulty of Raman spectroscopy is to separate it from the intense Rayleigh scattering. However, the major problem here is not Rayleigh scattering itself, but the fact that the intensity of stray light from the Rayleigh scattering may be one million times stronger than Raman scatter. If this light is allowed to pass into the spectrograph, it will be almost impossible to see any Raman spectrum at all. For

this reason Rayleigh scatter must be removed. There are two main techniques for the removal of this light: (1) rejection filters like dilelectric filters, holographic notch filters and colored glass filters; (2) subtractive double spectrographs.

iii. Detector: Most of the current Raman spectroscopies are equipped with multichannel two-dimensional CCD detector. The main advantages of such detectors are the high quantum efficiency, the extremely low level of thermal noise, low read noise and the large spectral range available.

iv. Spectrograph: A spectrograph is an instrument used to separate and measure the wavelengths and the relative amounts of radiation at each wavelength, in other words, to obtain and record the spectral content of light.

3.3.4 Advantages of Raman spectroscopy

Raman spectroscopy has several advantages as a useful method to perform chemical analysis:

i. Specificity: Because Raman detects the fundamental vibrations, the Raman bands have a good signal-to-noise ratio and are non-overlapping. This allows a Raman spectrum to be used for very wide-ranging materials.

ii. Analysis of aqueous systems: The Raman spectrum of water is weak and unobtrusive, which allows good spectra to be acquired of species in aqueous solution.

iii. No special preparation of the sample: Unlike most other chemical analysis techniques, Raman requires no special preparation of the sample. In fact, no contact with the sample is needed at all, because Raman involves only illuminating a sample with a laser and collecting the scattered photons, which makes Raman spectroscopy non-destructive.

iv. Short timescale: Because a Raman spectrum can be acquired in as little as a few seconds, Raman can be used to monitor chemical reactions in “real time”.

3.3.5 Raman bands of zirconia phases

Raman spectra of the most important phases - with the effects of pressure, temperature, grain size, and dopants on the band position - of zirconia will be discussed here (Fig. 38). Typical spectrum of monoclinic zirconia has 18 characteristic bands, and the bands at 180/190 cm^{-1} and 476 cm^{-1} are very distinct because of the high intensity. Compared with monoclinic phase, only six bands can be seen from the Raman spectrum of tetragonal zirconia. The bands at 259 cm^{-1} and 642 cm^{-1} are the two most significant bands. Cubic zirconia has just one broad band at about 600 cm^{-1} with high background. The Raman bands of different zirconia phases can be easily distinguished from each other.

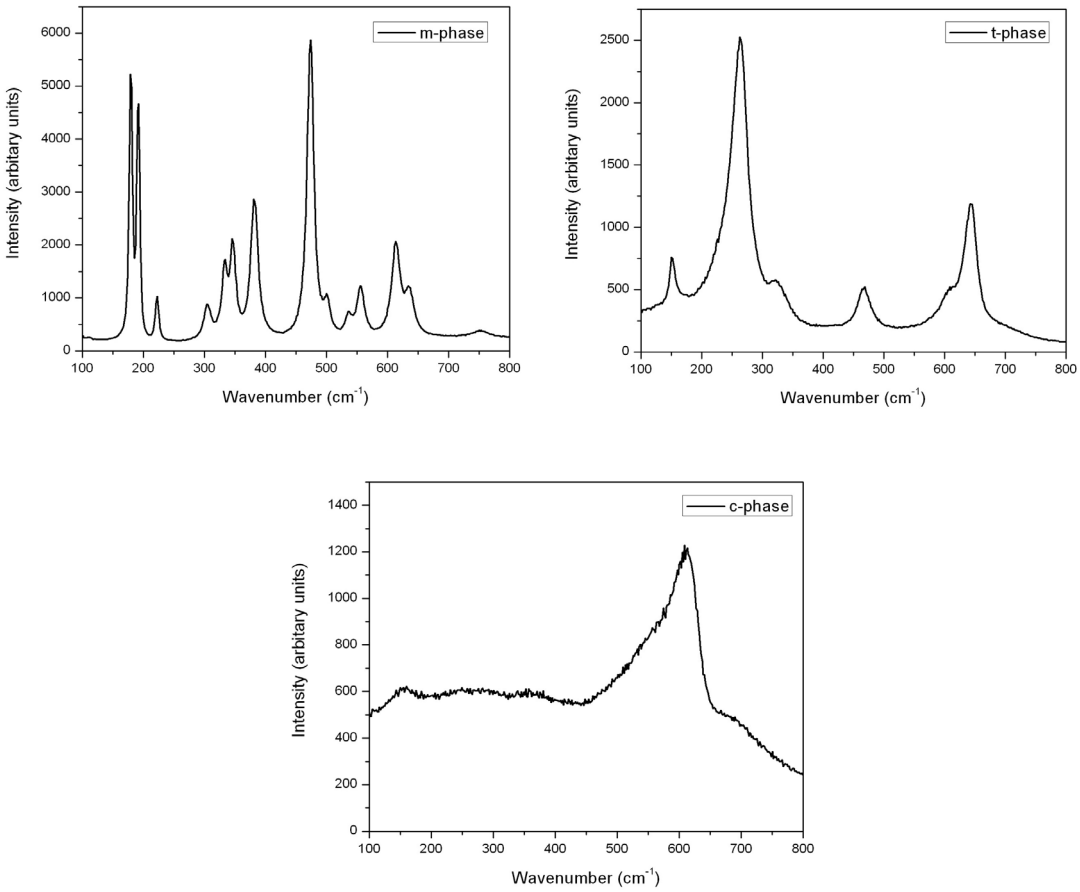

Fig. 38 Typical Raman spectra of monoclinic (m-), tetragonal (t-) and cubic (c-) zirconia.

3.3.5.1 Vibration modes

The vibration generated from a Raman band is divided into different classes of vibration modes. The types are designated according to the symmetry operations [99, 100]:

A	symmetric with respect to the principal axis of symmetry
B	antisymmetric with respect to the principal axis of symmetry
E	doubly degenerate with respect to the principal axis of symmetry
F	triply degenerate with respect to the principal axis of symmetry
g and u (subscripts)	symmetric or antisymmetric with respect to the center of symmetry (taken from the German words *gerade* and *ungerade* meaning even and uneven, respectively)
1,2,3 (subscripts)	symmetric or antisymmetric with respect to a rotation axis (C_p) or rotation-reflection axis (S_p), or if the other symbols are not sufficient to specify different species other than the principal axis or in those point groups with only one symmetry axis with respect to a plane of symmetry

3.3.5.2 Spectra of the different phases

The Raman active modes of monoclinic zirconia, which belong to the space group C_{2h}^5 and have four formula units per unit cell, were calculated to be 18 (9Ag+9Bg) in a group theoretical analysis [26, 101-103]. The bands at about 181/190 cm^{-1} and 476 cm^{-1} have significantly high intensities. In order to make mode assignments of the Raman bands, the Raman spectra of the anionic- as well as the cationic-labelled monoclinic $^{91.22}Zr^{16}O_2$ was investigated by Kim and Hamaguchi [101]. ^{16}O is partially replaced by ^{18}O and $^{91.22}Zr$ is replaced by $^{93.80}Zr$. The Raman spectra were quantitatively analyzed and three modes were assigned. Four bands at 180, 192, 224 and 334 cm^{-1} were not influenced by the replacing of ^{18}O, but shifted to lower wavenumbers by the replacing of $^{93.80}Zr$, then they were assigned to Zr-Zr vibrations. Three bands at 308, 349 and 380 cm^{-1} were influenced by both $^{91.22}Zr$-$^{93.80}Zr$ and ^{16}O-^{18}O substitutions and shifted to lower wavenumbers, because of which they were assigned to Zr-O vibrations. The remaining eight Raman bands from 382 to 800 cm^{-1} and at 105 cm^{-1} shifted to lower wavenumbers by the ^{16}O-^{18}O substitution and shifted to higher wavenumbers by the $^{91.22}Zr$-$^{93.80}Zr$ substitution, from which they were assigned to O-O vibration. The results are listed in Table 4.

ω_0 (cm^{-1})	Vibration	ω_0 (cm^{-1})	Vibration
105	(O-O)	385	(O-O)
180	(Zr-Zr)	476	(O-O)
192	(Zr-Zr)	503	(O-O)
224	(Zr-Zr)	539	(O-O)
308	(Zr-O)	558	(O-O)
334	(Zr-Zr)	616	(O-O)
349	(Zr-O)	638	(O-O)
380	(Zr-O)	757	(O-O)

Table 4 Monoclinic Raman bands and their vibrations[101].

The Raman active modes of tetragonal zirconia, which belong to the space group C_{4h}^{15} or $P4_2/nmc$ and have two formula units per unit cell, were calculated to be 6 (A_{1g}+$2B_{1g}$+$3E_g$) [26, 102-104]. The bands at 609 (B_{1g}) and 639 (E_g) cm^{-1} are categorized as Zr-O_I stretching. Bands at 321 (B_{1g}) and 465 (E_g) cm^{-1} are assigned to the coupling of O_I/O_{II}-Zr-O_I/O_{II} bending and Zr-O_I/O_{II} stretching. The band at 259 cm^{-1} (A_{1g}) is mainly Zr-O_{II} stretching. The band at 147 cm^{-1} (E_g) is assigned to O_I-Zr-O_I and Zr-O_I-Zr bending.

The difference given by Feinberg and Perry [105] is located at: 155 cm^{-1} (B_{1g}), 266 cm^{-1} (E_g) and 616 cm^{-1} (A_{1g}). The more recent research [106, 107] discusses these assignments and gives different Raman band modes.

The cubic zirconia has a fluorite structure with a very broad band at about 600 cm^{-1}. The space group is O_h^5 and the Raman active mode is F_{2g} [108]. This band position changes with the type of stabilizing oxide [109-111].

The crystal structures of the cotunnite-type phases (space group, Pnam, z=4) of pure zirconia and hafnia were detected by Haines et al. [112], who gave the Raman spectral data in detail for both. According to the calculation of Mirgorodsky and Quintard [113], there are 18 Raman active modes ($6A_g$+$3B_{1g}$+$6B_{2g}$+$3B_{3g}$), of which six are lower-frequency modes due to the heavy metal cations and 12 are due to the anions. Bulk modulus value of cotunnite-type zirconia was estimated

as 254 GPa, which is about 50% and 30% higher than those of cubic and monoclinic zirconia, respectively. The Raman bands of different phases and their active modes are shown in Table 5.

Monoclinic ω_0 (cm^{-1})	Tetragonal ω_0 (cm^{-1})				Cubic ω_0 (cm^{-1})	Cotunnite structure ω_0 (cm^{-1})
102 (A_g) m	146 m	(B_{1g}) [d]	(E_g) [e]	(B_{1g}) [f]	150 [g]	149 (B_{3g}) m
175 (B_g) [a]	270 s	(E_g) [d]	(A_{1g}) [e]	(E_g) [f]	250 [g]	163 (A_g) s
179 (A_g) s	318 m	(B_{1g}) [d]	(B_{1g}) [e]	(B_g) [f]	360 [g]	167 (B_{1g}) m
190 (A_g) s	458 m	(E_g) [d]	(E_g) [e]	(E_g) [f]	480 [g]	201 [i] vvm
222 (B_g) w	602 m	(A_{1g}) [d]	(B_{1g}) [e]	(A_{1g}) [f]	~600 (F_{2g}) [h]	239 (A_g) w
305 (A_g) w	648 m	(E_g) [d]	(E_g) [e]	(E_g) [f]		279 (B_{2g}) w
317 (A_g) [b]						341 (B_{1g}) vw
334 (B_g) m						362 (B_{2g}) m
348 (A_g) m						378 (A_g) m
381 (B_g) m						387 (B_{3g}) m
476 (A_g) s						413 [i] m
500 (B_g) w						436 (A_g) s
534 (B_g) w						561 (A_g) m
556 (A_g) w						569 (B_{3g}) m
615 (B_g) m						601 (B_{2g}) m
638 (A_g) m						622 (B_{1g}) m
748 (B_g) [c]						661 (B_{2g}) m

Table 5 Raman bands of the different phases and their modes

Note: s=strong, m=medium, w=weak, v=very
Monoclinic phase [26, 106, 114-118], tetragonal phase [103, 105, 107, 114], cubic phase [108, 117], and cotunnite structure [112, 113].
[a] only observed by Zhao and Vanderbilt [26], and Quintard et al. [106].
[b] only observed by Zhao and Vanderbilt [26].
[c] not observed by Alzyab and Perry [114], Kourouklis and Liarokapis [115], and Phillippi and Mazdiyasni [117], Ishigame and Sakurai [116].
[d] Raman modes by Feinberg and Perry [105].
[e] modes by Quintard et al. [106] and Merle et al. [107].
[f] modes by Alzyab and Perry [114].
[g] observed by Phillippi and Mazdiyasni in cubic stabilized cubic [117].
[h] mentioned by Cai et al. [108].
[i] not mentioned by Mirgorodsky and Quintard [113].

3.3.5.3 Pressure-induced phase transformation

The investigation of the phase transformation at high pressure in ZrO_2 is important to understand the toughening mechanism. Raman spectroscopy is utilized to characterize the phase transformation and transition pressure using a diamond anvil pressure cell by the ruby fluorescence method. Monoclinic ZrO_2, which is the stable phase of ZrO_2 at room-temperature and atmospheric pressure, was used for the research [58, 115].

The phonon frequencies of ZrO_2 as a function of pressure up to 16 GPa are presented in Fig. 39. What can be clearly seen is that, the phonon frequencies change abruptly at 3.5 GPa, indicating a phase transition. The new phase appears to be stable at least up to 16 GPa [115]. The observed phonon frequencies, along with their pressure derivatives ($d\omega/dP$), for both monoclinic and

tetragonal phases are tabulated in Table 6. In the study of Arashi et al. [58], the phase transformation of pure ZrO_2 at 13 GPa was confirmed from micro-Raman scattering and XRD experiments. This high-pressure phase belongs to crystal system with lower symmetry such as orthorhombic. Another phase transformation of ZrO_2 was found at 35 GPa, and stable up to 60 GPa.

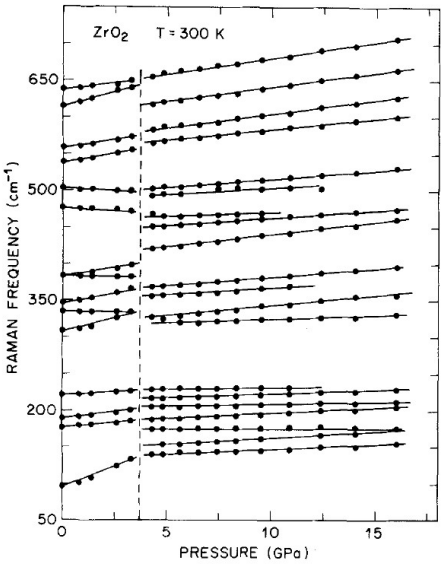

Fig. 39 Pressure dependence of Raman spectra of ZrO_2[115].

Phase I (monoclinic)		Phase II (tetragonal)	
ω_0 (cm^{-1})	(dω/dP) (cm^{-1}/GPa)	ω_0 (cm^{-1})	(dω/dP) (cm^{-1}/GPa)
97	7.8	135	1.2
177	2.5	145	1.7
190	3.3	174	0.2
222	1.5	181	1.5
306	7.8	202	0.6
335	-0.3	212	1.0
347	5.8	228	0.4
383	-0.3	313	1.0
383	4.7	346	2.1
477	-1.4	359	2.4
503	-1.2	405	3.5
538	5.3	441	2.1
558	4.7	463	0.6
615	7.9	489	1.4
638	3.5	493	2.3
		553	3.0
		568	3.7
		600	4.0
		638	4.3

Table 6 Phonon frequencies and their slopes (dω/dP) of ZrO_2 for both the low-pressure (monoclinic) and high-pressure (tetragonal) phase[115].

Pure and doped zirconia containing 3 and 4wt% Y_2O_3 were studied by Alzyab and Perry [114] using Raman spectroscopy to indicate the pressure-induced phase transformation. A quantitative determination of the percent of the tetragonal phase x(T) present in each sample was estimated using $x(T) = I(T)/[I(T) + I(M)]$. I(T) represents the added intensities (integrated areas) of the two bands at about 148 and 262 cm^{-1} which are characteristic of the tetragonal phase; I(M) denotes the added intensities of the two bands at 178 and 190 cm^{-1}, which are associated with the monoclinic phase (Fig. 40). Pure ZrO_2 has pressure-hysteresis behaviour in the transformation from monoclinic to the tetragonal structure. The monoclinic phase transforms to the tetragonal phase at P=4.10 GPa for ZrO_2-3 wt% Y_2O_3, and at P=3.35 GPa for ZrO_2-4 wt% Y_2O_3.

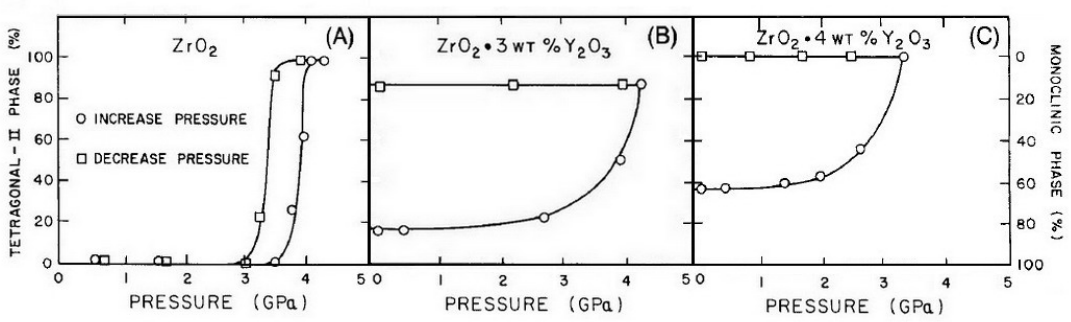

Fig. 40 Phase transitions in the ZrO_2-Y_2O_3 system as a function of pressure[114].

Yttria-stabilized cubic zirconia and polycrystalline yttria-stabilized tetragonal zirconia were studied at 300K with the use of Raman spectroscopy under uniaxial stress by Cai et al. [108]. The frequency shifts of the Raman band at about 610 cm^{-1} of cubic zirconia vary linearly with the applied stress, and tend to increase with the dopant concentration. Five main bands of tetragonal zirconia under stress were measured, and the results of bands at 147, 261, 320, 464 and 642 cm^{-1} are shown in Table 7. The values are smaller than that of the cubic crystal. The negative slope of the band at 261 cm^{-1} attributes to the softening of the mode with the hydrostatic component of uniaxial stress, which is associated with an approaching phase transition, possibly to a disordered structure.

ω (cm^{-1})	147	261	320	464	642
dω/dP(cm^{-1}/GPa)	0.98	-0.92	1.3	2.1	1.1

Table 7: Pressure dependence of the band positions for the tetragonal phase[108].

3.3.5.4 Temperature and grain size dependence of the Raman spectra

A microcrystallinity with a grain size of 15 to 30 Å was found for dehydrated amorphous ZrO_2 by Keramidas and Whit [103]. Raman spectra characteristic of the metastable tetragonal polymorph were obtained, and the recrystallization into first a metastable tetragonal phase and then the stable monoclinic phase induced by heating the amorphous materials was found. Up to a temperature of 200 °C, only dehydrated amorphous zirconia existed. Further heating at 500 °C caused a metastable tetragonal phase and then a mixture of the monoclinic and tetragonal phases. At 1000 °C there was complete conversion to the stable monoclinic phase.

Sixteen distinct frequencies and two weak shoulders were observed in monoclinic zirconia, and six frequencies could be attributed to the tetragonal phase obtained from heated amorphous zirconia, which is not identical with the results from Phillippi and Mazdiyasni [117]. There was additional existence of monoclinic phase in the spectra of Phillippi and Mazdiyasni, which were regarded as Raman bands of the tetragonal phase. These misinterpreted tetragonal bands are in fact the strongest bands of the monoclinic phase.

The Raman spectra of monoclinic zirconia at 300 K to 1600 K were obtained by Ishigame and Sakurai [116], as shown in Fig. 41. The Raman spectra lines show red shift and increase in line width as the temperature increases. The frequency shift is almost proportional to the temperature from 300 K to 1250 K. The spectrum obtained at 1250 K shows a shift of about 10 cm^{-1} compared with that obtained at 300 K. At 1420 K, the width of the line at 90 cm^{-1} increases conspicuously and a broad band appears at about 250 cm^{-1}. The lines originating from the monoclinic phase become faint and barely visible at 1455 K. At 1475 K, six tetragonal Raman bands appeared. With the change of temperature, there are spectra of monoclinic ZrO_2 at low temperature, tetragonal ZrO_2 at high temperature, and complex spectra observed at phase-transformation temperatures, spectra which consist of Raman lines originating from both the monoclinic and tetragonal phases.

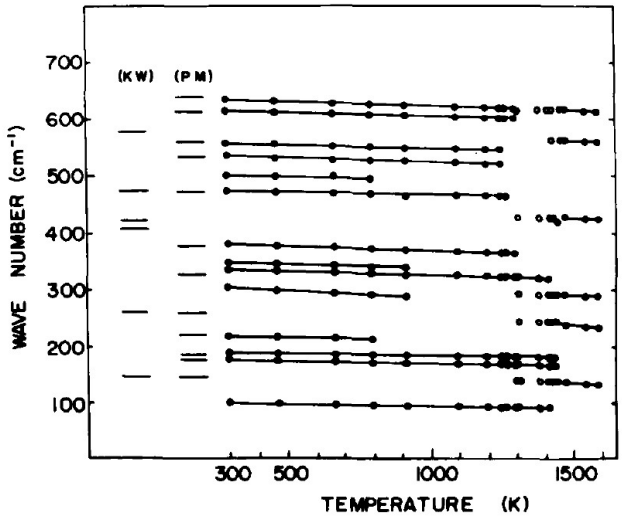

Fig. 41 Temperature dependence of Raman frequencies of ZrO_2[116].

The cracks from preparation did not show further cracking when the specimen was heated to high temperatures by the phase changes. Since the phase transformation in zirconia involves changes in the Zr-O bond lengths and bond angles, along with a volume change, large strains are set up in the crystal. The structure at phase transformation temperatures would be expected to be disordered if it were undergoing a reconstructive transformation. Therefore, the line-broadening might result from the breakdown of the k=0 selection rule (k = wave vector) for structures, as seen for a compositional disordered crystal [116, 119].

Raman spectroscopy was used by Perry et al. [120] to characterize phase transformations and transition temperatures in partially stabilized zirconia containing ≤20 wt% yttria. The completeness of martensitic transition and its thermal hysteresis followed in specimens with ≤4 wt% yttria, and the variation of the transformation temperatures are summarized in Table 8. Between 5 and 12 wt% the spectra indicated that a tetragonal modification precipitated in a disordered cubic fluorite matrix. Above 15 wt% the spectra is characteristic of the fully stabilized disordered cubic phase.

Composition (wt% Y_2O_3)	Transition temperature (°C)			
	Heating		Cooling	
	Monoclinic→Tetragonal		Tegragonal→Monoclinic	
	(start)	(finish)	(start)	(finish)
0	1070	1150	1000	950
3	410	590	500	330
4	400	570	490	320

Table 8 Phase transition temperature during heating and cooling of ZrO_2-Y_2O_3 through the tetragonal-monoclinic transformation[120].

The Raman spectra of 5 wt% yttria-stabilized tetragonal zirconia from 25 to 1250 °C were reported by Lughi and Clarke [121]. All the six bands characteristic of tetragonal zirconia broaden and shift toward lower wave numbers with increasing temperatures. The shift of all bands mainly contributes to the thermally-induced volume changes, which, however, cannot explain the unexpected negative value of the thermospectroscopic coefficient found for the band at 260 cm^{-1} (at room temperature), as shown in Fig. 42. The solid lines through the data correspond to the best fitting with a quadratic function. The dashed lines correspond to the contribution to the shift due to volume expansion. The dotted line corresponds to the calculated volume expansion for the band at around 260 cm^{-1} if the sign of the piezospectroscopic coefficient is disregarded. The noticeable scatter in the position of the band at about 610 cm^{-1} arises from the poor reliability of the fitting for this specific band, which only appears as a shoulder on the much more intense band at 640 cm^{-1}.

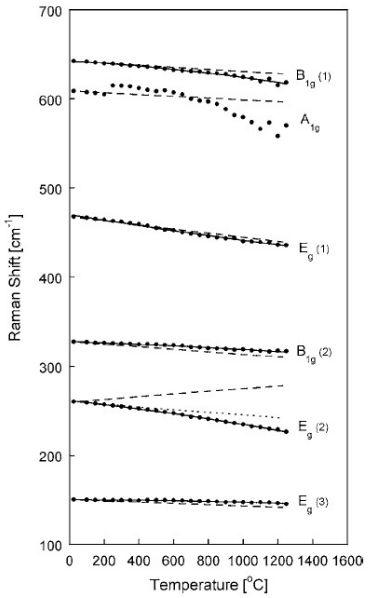

Fig. 42 Raman peak position as a function of temperature[121].

Monoclinic zirconia with nanometer-sized grains ranging from 5 to 80 nm was studied by Liu et al. For the specimen, which contains grains as small as 14 nm, a new asymmetric and broad peak at 1040 cm^{-1} appears, which is not observed in the Raman spectra of single-crystal or polycrystalline zirconia. The new peak shifts toward higher frequency and the intensity increases gradually with decrease of grain size, as suggested, resulting from a surface phonon mode [119].

The other peaks observed in the Raman spectra shift to lower frequencies, and their bandwidths broaden when the grain size decreases. The peak broadening makes neighboring peaks overlap. The 616 and 638 cm^{-1} band lines for specimen with grain size over 1 μm overlapped into a single peak 608 cm^{-1} and shifted to lower frequency with a grain size decrease. As the grain size decreases to 5 nm, the peak frequency of 616 cm^{-1} line shifts to a lower frequency by about 8 cm^{-1}. The full width at half maximum (FWHM) of the specimen with 14 nm is several cm^{-1} wider than that of the specimen with over 1 μm. This phenomenon can be explained by a phonon confinement model, and the increase of disorder degree can also lead to the peak broadening for the nanocrystallite, like the broadening Raman peaks of an amorphous phase.

These results were partially confirmed by Siu et al. [118] in their study. By the observing the Raman spectra range from 80-1250 cm^{-1}, the red shift with grain-size reduction is common, but blue shift also occurs. The research by Jouanne et al. [122] indicates that the frequency shift of the Raman peaks is primarily due to the increasing size of the zirconia crystallites, but the mixture of the metastable tetragonal phase with the monoclinic phase obscures the effect.

3.3.5.5 Dependence on dopants

Phase transitions in zirconia doped with different rare earth oxidations were studied using Raman spectroscopy [123-125]. XRD is not very sensitive to oxygen-induced transitions, because the oxygen has a smaller scattering factor than zirconium and rare earth ions. The ZrO_2-Xmol%$RO_{1.5}$ (R=Nd, Sm, Y, Er, Yb; X=0, 2, 4….22, 24) were investigated to show the cubic-tetragonal phase transition [124].

The pure ZrO_2 without any rare earth dopants showed many sharp bands characteristic of the monoclinic phase. The tetragonal man monoclinic phases coexisted at X=2 and 4 for Nd, Y, Er and Yb, and at X=2 for Sm. The tetragonal single phase is obtained in the specimens with high content, and shows six typical bands.

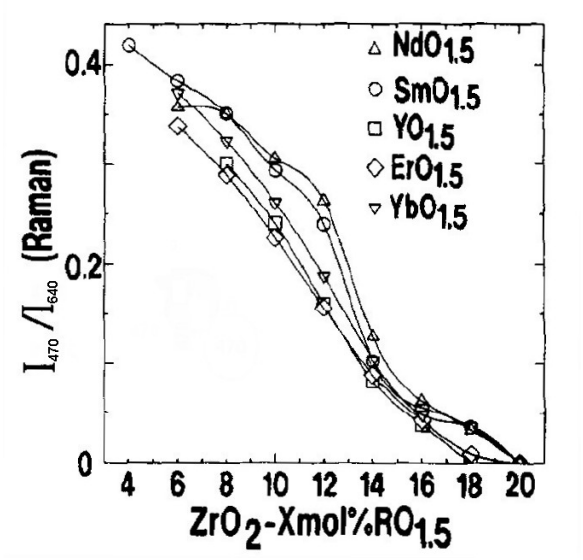

Fig. 43 Variation of the Raman peak height ratio I_{470}/I_{640} with the $RO_{1.5}$ content [124].

The Raman peak intensity at about 470 cm^{-1}, which is characteristic of the tetragonal phase, decreased with an increase of $RO_{1.5}$ content. The decrease of I_{470}/I_{640} with increasing $RO_{1.5}$ content

corresponds to that of the oxygen displacement (Fig. 43) [124].. The cubic-tetragonal phase boundaries are located between 18 and 20 mol% $RO_{1.5}$. The phase boundaries and the formation region are almost independent of the dopant species. A tetragonal phase, whose axial ratio c/a is unity, is interpreted to exist at about 16 mol% $RO_{1.5}$ using XRD.

2 mol% Y_2O_3 stabilized tetragonal zirconia solid solutions doped with ceria, titania, germania, and cassiterite were investigated to prove the effect of the dopant size on the changes in Raman spectra [123]. The shift of the 259 cm^{-1} mode, as a function of dopant concentration, is consistently greater than that of the 640 cm^{-1} mode for all undersized dopants and is somewhat smaller for the Ce^{4+} ion (Fig. 44). The deviations in the Raman spectra are influenced by the cation mass and the force constant. The frequencies of the 259 and 640 cm^{-1} Raman modes increase as doping with the undersized cations increases, and decrease as doping with the undersized cation decreases.

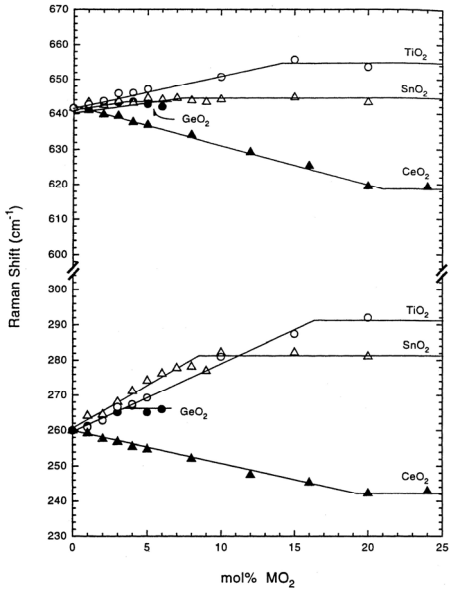

Fig. 44 Shifts of 259 cm^{-1} and 640 cm^{-1} Raman modes, as a function of tetravalent dopant concentration in 2Y-TZP[123].

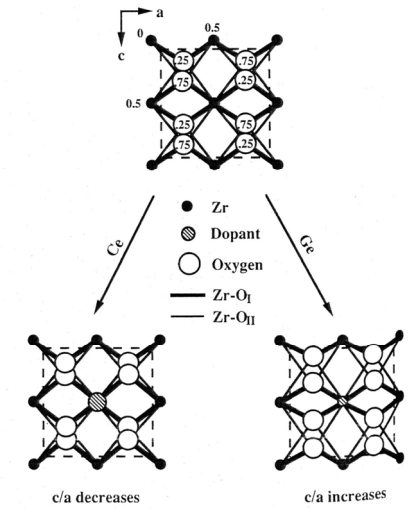

Fig. 45 Schematic illustration for variation of tetragonality of zirconia solid solutions (numbers indicate atom positions in b direction)[123, 126].

Zirconia solid solutions with tetravalent oxides, including Ce^{4+}, Ti^{4+} and Ge^{4+} have been studied to show that the crystallographic variations are dependent on dopant sizes [123, 126]. Ce^{4+} was chosen as the most commonly used oversized tetravalent stabilizer and Ge^{4+} was chosen as the most effective undersized tetravalent dopant for stablilizing tetragonal zirconia at room temperature. Two types of host cation-O bonding exist in tetragonal zirconia: $Zr\text{-}O_I$ and $Zr\text{-}O_{II}$. Both O_I and O_{II} form a tetrahedron, though of different size, around Zr. The introduction of Ce^{4+} ions, which adopt a more symmetric 8-fold coordination because of their larger size, has an effect of assimilating these two types of bonding, and accounts for the decrease in the c/a ration. The tetragonality of the zirconia solution increases with increasing concentration of the undersized Ge^{4+} dopant and enhances the anisotropy of the tetragonal structure (Fig. 45)[123, 126].

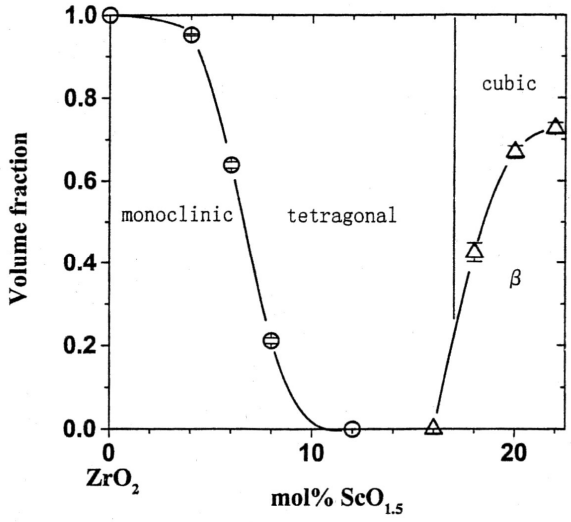

Fig. 46 Variation of the volume fraction of m-phase and β-phase with $ScO_{1.5}$ content[127].

Monoclinic, tetragonal, cubic, and rhombohedral ($Sc_2Tr_7O_{17}$, β-phase) phases are found using XRD and Raman spectroscopy for Scandia-doped zirconia solid solution $ZrO_2\text{-}XScO_{1.5}$ (X=0-22 mol %), as shown in Fig. 46 [127]. The compositional regions of m-phase, m- and t-phases, t-phase, β- and c-phases were 0, 2-10, 12-16, and 18-22 mol % $ScO_{1.5}$, respectively. The m-phase fraction decreased as the content of $ScO_{1.5}$ increased, while the β-phase increased as the content increased. Closed to typical peaks of m-phase and t-phase for the samples with X>18 mol %, many small peaks were attributable to the β-phase, because the c-, t-, and m-phases of zirconia do not show such spectra.

3.3.5.6 Polarisation dependence of the band intensities

Irreducible components of the Raman spectra obtained from polarisation measurements at room temperature were discussed by Ishigame and Sakurai [116], as shown in Fig. 47. The A_g and B_g symmetries were determined by measuring the intensity ratios for equal intensities of incident light, except the line at 179 cm^{-1}. This line has different ratios to suggest that it consists of two Raman lines which degenerate in frequency but have different symmetries.

The research of the Raman active modes of tetragonal zirconia began more than 20 years ago [105, 128]. Voronko et al. assigned A_{1g} mode with the Raman band at 262 cm^{-1}, while Feinberg and Perry assigned this mode position as near 616 cm^{-1}.

Polarised light scattering from single crystal grains of epitaxial films of pure tetragonal zirconia grown on monocrystalline alumina was analyzed by Merle et al. [107], as shown in Fig. 48. Six main bands for t-zirconia have been marked, and the lines near 146 and 270 cm^{-1} are related to different polarisability tensor elements, xy and zz, respectively.

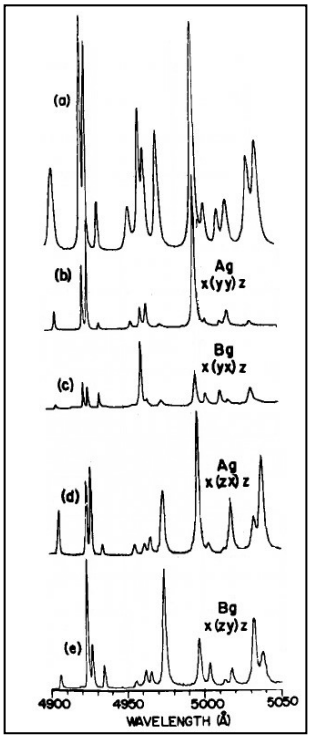

Fig. 47 Raman spectra of monoclinic zirconia at 300 K. Curve (a) represents polycrystalline zirconia fused in solar furnace, (b), (c), (d) and (e) are polarized spectra obtained from single crystal[116].

The orientation-dependent intensity of the tetragonal Raman band at 265 cm^{-1} was investigated by observing the ratio of the t-band with maximum change at 265 cm^{-1}, normalized to the band with the lowest change at 648 cm^{-1} by Dorn and Nickel [129]. It was indicated that a rotation of ±30° is necessary, and if the polarisation cannot be rotated, the information from the Raman spectra is reduced.

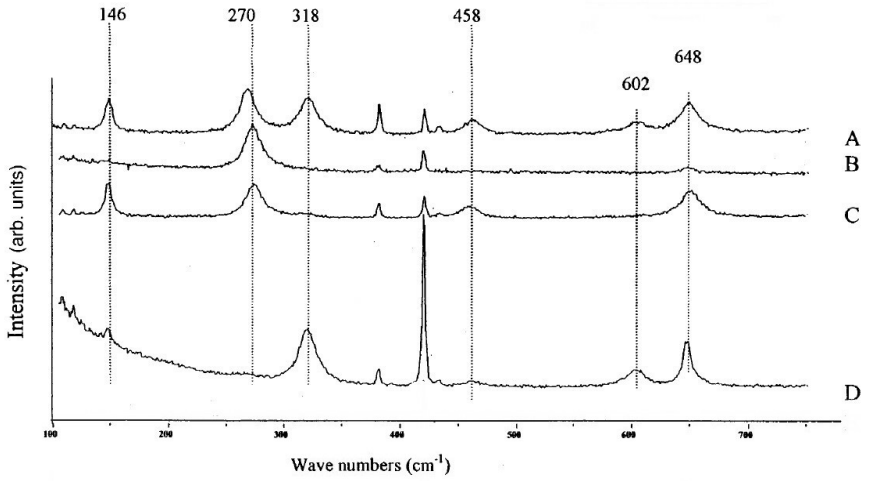

Fig. 48 Raman spectra of zirconia / alumia samples. A, unpolarized scattering; B, x(zz)-x; C, x(zy)-x; D, z(xx)-z[107].

3.4 Finite element method

3.4.1 Introduction

When the complex stress problems cannot easily be solved using classical mechanics, finite element method (FEM) is commonly used, which is a numerical approximation technique for the analysis of mechanical systems. The development of FEM can be traced back to the work of Alexander Hrennikoff and Richard Courant. Over the past decades, FEM has evolved from a structural analysis tool used for civil engineering and aeronautical engineering to a set of refined commercial programs, due to the availability of much faster, more powerful computers and improved numerical methods.

The excellent features of FEM are: (1) It can readily handle very complex geometry, which is the heart and power of FEM; (2) It can deal with a wide variety of engineering problems such as solid mechanics, dynamics, heat problems, fluids and electrostatic problems; (3) It can treat complex restraints as indeterminate structures; (4) It can handle complex loading like nodal point loads, element load (pressure, thermal or inertial forces) and time- or frequency-dependent loading. The disadvantages of the FEM are that it obtains only approximate solutions and contains inherent errors.

3.4.2 The fundamental equations of elasticity

Elasticity is the physical property of a material; the material returns to its original shape after the stress, under which it deforms, and is removed. The fundamental equations of elasticity and the equivalent variational principles are always used in finite element methods, and the following parts will discuss the corresponding description by means of matrix and tensor.

3.4.2.1 Balance equations

It is supposed that the space of a material is completely and continuously filled with the substance of the body, and then the stress of a continuous medium can be created by the actions of an external body force and the contact force (or surface force). The stress tensor $\boldsymbol{T}$ at an arbitrary point of the body can be represented as following:

$$\begin{Bmatrix} \sigma_x & \tau_{xy} & \tau_{xz} \\ \tau_{yx} & \sigma_y & \tau_{yz} \\ \tau_{zx} & \tau_{zy} & \sigma_z \end{Bmatrix}$$

The total resultant force is:

$$\mathbf{F} = \mathbf{F}_b + \mathbf{F}_c = \int_v \mathbf{b} dv + \int_s \mathbf{t}_n ds \tag{39}$$

where the first part is body force and the second part is contact force, and $\boldsymbol{b}$ is body force per volume and $\boldsymbol{t}_n$ is stress vector, assuming n is the exterior unit normal vector at the point. The stress vector can be written as:

$$\mathbf{t}_n = \mathbf{n} \bullet \mathbf{T} = \mathbf{t}_x n_x + \mathbf{t}_y n_y + \mathbf{t}_z n_z \tag{40}$$

Integration is made for the formula above on the contact surface:

$$\int_s \mathbf{n} \bullet \mathbf{T} ds = \int_s \left(\mathbf{t}_x n_x + \mathbf{t}_y n_y + \mathbf{t}_z n_z \right) ds = \int_v \left(\frac{\partial \mathbf{t}_x}{\partial x} + \frac{\partial \mathbf{t}_y}{\partial y} + \frac{\partial \mathbf{t}_z}{\partial z} \right) dv = \int_v div\mathbf{T} dv \tag{41}$$

Considering Newton's second law,

$$\int_v \left(\mathbf{b} + div\mathbf{T} \right) dv = 0 \tag{42}$$

That is:

$$div\mathbf{T} + \mathbf{b} = 0 \tag{43}$$

This formula can also be written in an expanded form:

$$\begin{aligned} \frac{\partial \sigma_{\mathbf{x}}}{\partial x} + \frac{\partial \tau_{yx}}{\partial y} + \frac{\partial \tau_{zx}}{\partial z} + b_x = 0 \\ \frac{\partial \tau_{xy}}{\partial x} + \frac{\partial \sigma_{\mathbf{y}}}{\partial y} + \frac{\partial \tau_{uy}}{\partial z} + b_y = 0 \\ \frac{\partial \tau_{xz}}{\partial x} + \frac{\partial \tau_{yz}}{\partial y} + \frac{\partial \sigma_{\mathbf{z}}}{\partial z} + b_z = 0 \end{aligned} \tag{44}$$

These are three independent equations with six independent unknowns (stresses) for balance equations. Using the summation convention, the general form of balance equations can be written as:

$$\sigma_{ij,j} + b_i = 0 \tag{45}$$

where suffix "$,j$" means the derivative of coordinate x_j. There are three independent equations with six independent unknowns.

3.4.2.2 Strain-displacement equations

Regarding small displacement and small deformation, the squares and products of the derivatives of displacement components can be ignored, and then the relationship of strain and displacement is described as following:

$$\varepsilon_x = \frac{\partial u}{\partial x}, \gamma_{xy} = \frac{\partial u}{\partial y} + \frac{\partial v}{\partial x}$$
$$\varepsilon_y = \frac{\partial v}{\partial y}, \gamma_{yz} = \frac{\partial v}{\partial z} + \frac{\partial w}{\partial y} \quad (46)$$
$$\varepsilon_x = \frac{\partial w}{\partial z}, \gamma_{zx} = \frac{\partial u}{\partial z} + \frac{\partial w}{\partial x}$$

where *u, v, w* are the projections of a displacement vector in a rectangular coordinate system. This can also be written in the form of tensor:

$$\varepsilon_{ij} = \frac{1}{2}\left(u_{i,j} + u_{j,i}\right) \quad (47)$$

There are six independent equations relating strains and displacements, and nine independent unknowns (strains and displacements) for the strain-displacement equations.

3.4.2.3 Constitutive equations

In elasticity, constitutive equations connect the stress and strain. The stress-strain constitutive relation for isotropic linear materials is commonly known as Hooke's law:

$$\sigma_{xx} = 2G\varepsilon_{xx} + \lambda\left(\varepsilon_{xx} + \varepsilon_{yy} + \varepsilon_{zz}\right), \sigma_{xy} = 2G\varepsilon_{xy}$$
$$\sigma_{yy} = 2G\varepsilon_{yy} + \lambda\left(\varepsilon_{xx} + \varepsilon_{yy} + \varepsilon_{zz}\right), \sigma_{yz} = 2G\varepsilon_{yz} \quad (48)$$
$$\sigma_{zz} = 2G\varepsilon_{zz} + \lambda\left(\varepsilon_{xx} + \varepsilon_{yy} + \varepsilon_{zz}\right), \sigma_{zx} = 2G\varepsilon_{zx}$$

where G is shear modulus and λ is Lamé's coefficients:

$$G = \frac{E}{2(1+\upsilon)}, \lambda = \frac{E\upsilon}{(1+\upsilon)(1-2\upsilon)} \quad (49)$$

Here E is elastic modulus and υ is poisson's ratio. Using the summation convention, the general form of Hooke's law can be written as:

$$\sigma_{ij} = C_{ijkl}\varepsilon_{kl} \quad (50)$$

The tensor $\boldsymbol{C}$ is called the stiffness tensor, which is 4^{th} order in three-dimensional stress state. These are six independent equations in constitutive equations to relate strains and stresses.

3.4.2.4 Principle of virtual work

The combination of all the three principles leads to the formulation of initial boundary value problems. Variational methods replace the solution of the corresponding boundary value problem.

Finite element method is based on the variational principles for minimizing some potential, for example, the potential energy of elastic body or a mechanical system.

$$\sigma_{ij,j} + b_i = 0 \tag{51}$$

This balance equation is multiplied by virtual displacement δu_j and integrated over the volume V:

$$\int_v \delta u_i \left(\sigma_{ij,j} + b_i\right) dv = 0 \tag{52}$$

According to the product rule,

$$\int_v \delta u_i \sigma_{ij,j} dv = \int_v \delta u_i \frac{\partial \sigma_{ij}}{\partial x_i} dv = \int_v \frac{\partial}{\partial x_i}\left(\sigma_{ij} \delta u_j\right) dv - \int_v \sigma_{ij} \frac{\partial\left(\delta u_j\right)}{\partial x_i} dv \tag{53}$$

Consider $\sigma_{ij} n_j - t_i = 0$,

$$\int_v \frac{\partial}{\partial x_i}\left(\sigma_{ij} \delta u_j\right) dv = \int_s n_i \sigma_{ij} \delta u_j ds = \int_s t_i \delta u_j ds \tag{54}$$

and

$$\int_v \sigma_{ij} \frac{\partial\left(\delta u_j\right)}{\partial x_i} dv = \int_v \sigma_{ij} \delta \frac{\partial u_j}{\partial x_i} dv = \int_v \sigma_{ij} \delta \varepsilon_{ij} dv \tag{55}$$

Then,

$$\int_s t_i \delta u_j ds + \int_v \delta u_i b_i dv - \int_v \sigma_{ij} \delta \varepsilon_{ij} dv = 0 \tag{56}$$

The first two parts are the virtual work of external forces, defined as δA; the third part is the virtual work of stresses or virtual strain energy, defined as δW. For a system in equilibrium, the principle of virtual work is:

$$\delta A - \delta W = 0 \tag{57}$$

This principle is also valid in the system of nodal displacements in a finite element analysis and governs the mechanical behaviour of the whole structure. An approximate solution of the system, including displacements, strains and stresses can be reached through the solution of the system of this virtual work equation.

3.4.3 Meshing

The principle of FEM is to subdivide the geometry of a solid into two-dimensional or three-dimensional elements (Fig. 49) [4], which are connected together at nodes (Fig. 50). All elements are governed by the same principles of equilibrium in different loading situations and by the material behaviour described through constitutive and Hooke's law.

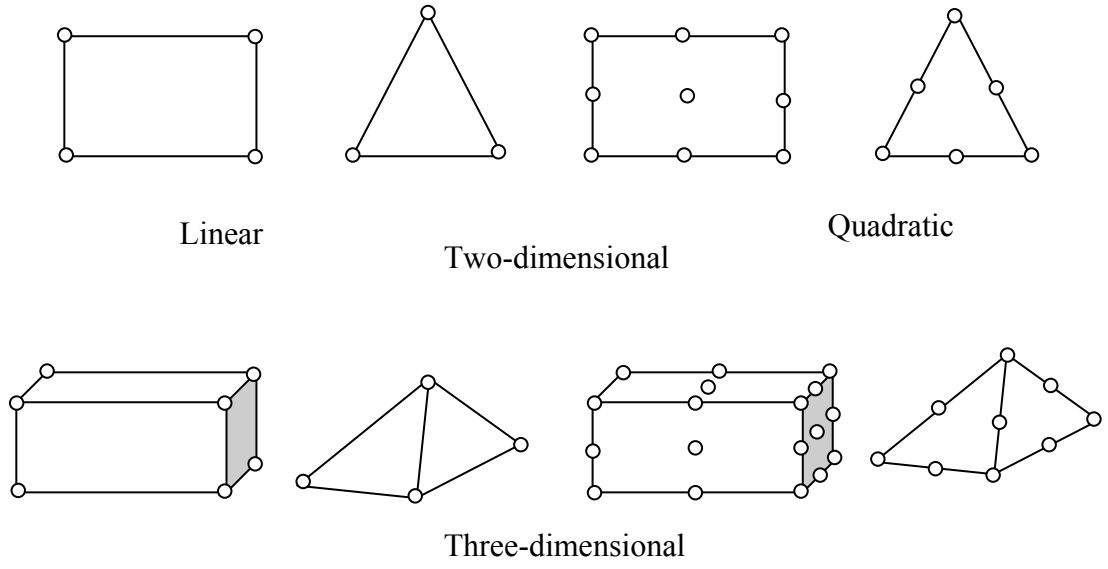

Fig. 49 Examples of element geometries used for finite element models.

The continuous body is divided by imaginary lines into a certain number, and the elements are assumed to be interconnected by the nodal points, which are located on their boundaries. All the systems of nodal displacements, created for the whole structure in which all the elements participate, automatically satisfy the condition of compatibility.

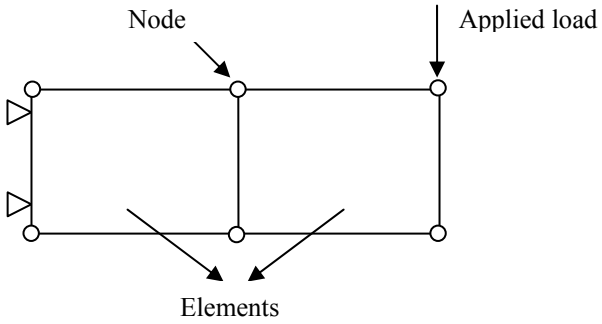

Fig. 50 Division of the geometry of a solid body into elements connected together at nodes.

3.4.4 Introduction to ABAQUS

In 1964 the first commercial finite element software appeared, and now there are hundreds of commercial software packages from which to choose. The ones dominating today's market include: ABAQUS (Hibbitt, Karlsson & Sorensen), ANSYS (Ansys, Incorporated), SDRC-Ideas (structural Data Research Corp.), RASNA (Parametric Technology, Inc.), MSC/NASTRAN (MSC Software Corp.)

In this thesis ABAQUS, founded in 1978, was used for FEM simulating. ABAQUS solves problems ranging from relatively simple linear analysis to the most challenging nonlinear simulation. It consists of two main analysis products: ABAQUS/Standard (static, dynamic,

thermal, or electrical response of components problems) and ABAQUS/Explicit (transient dynamic or highly nonlinear, involving changing contact conditions, problems).

Simulation process flow was listed as: (1) Select analysis type (structural static analysis, transient dynamic analysis, steady-state thermal analysis, coupled thermal-electrical analysis or coupled pore fluid-stress analysed); (2) Select element type (2-D or 3D; linear or quadratic; truss, beam, shell or solid); (3) Define material properties (elastic modulus, Poisson's ratio or density…); (4) Meshing; (5) Apply boundary conditions and loads; (6) Process; (7) Postprocess (displacement, strain, stress, temperature or time history…), as shown in Fig. 51 [130].

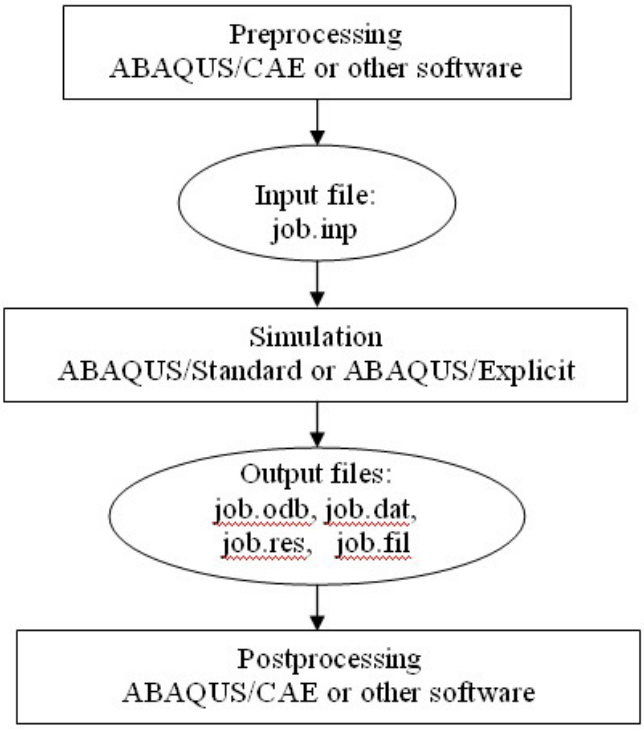

Fig. 51 The stages of ABAQUS analysis.

ABAQUS/CAE or other preprocessors are used to create the model representing a physical problem, and create an ABAQUS input file. ABAQUS/CAE is divided into functional units called modules:

Part: Sketch a two- or three-dimensional geometry
Property: Create section and material definitions and assign them to regions of parts
Assembly: Create instances of the parts, and position the instances relative to each other in a global coordinate system
Step: Create and configure analysis steps and associated output requests
Interaction: Specify mechanical and thermal interactions between regions of a model or between a region of a model and its surroundings
Load: Specify loads, boundary conditions and fields
Mesh: Generate a finite element mesh on an assembly
Job: Submit a job for analysis and monitor its progress
Visualization: Provide graphical display of finite element models and results
Sketch: Create a sketch to be extruded, swept or revolved to form a 3D part

ABAQUS has no built-in system of unit. Which system of units should be used must be decided before starting to define the model. All input data must be specified in consistent units.

3.4.5 Defining plasticity in ABAQUS

Plastic property is important for the modelling of a contact problem, so ABAQUS requires such values to interpret the property of the material correctly. Often material test data are supplied using values of nominal stress and strain. In such situations the expressions presented below must be used to convert the plastic material data from nominal stress/strain values to true stress/strain values [130].

For finite deformations, strains in compression or tension can be defined as: ($\Delta l \to dl \to 0$)

$$\varepsilon_{true} = \int_{l_0}^{l} d\varepsilon = \int_{l_0}^{l} \frac{dl}{l} = \ln\left(\frac{l}{l_0}\right) \tag{58}$$

Where l is the current length, l_0 is the original length, and ε is the true strain or logarithmic strain.

The true stress is defined as:

$$\sigma_{true} = \frac{F}{A} \tag{59}$$

where F is the force in the material and A is the current area. A ductile metal subjected to finite deformations will have the same stress-strain behaviour in tension and compression if true stress is plotted versus true strain.

The relationship between true strain and nominal strain is established by expressing the nominal strain as

$$\varepsilon_{nom} = \frac{l - l_0}{l_0} = \frac{l}{l_0} - 1 \tag{60}$$

Adding unity to both sides of this expression and taking the natural log of both sides provides the relationship between the true strain and the nominal strain:

$$\varepsilon_{true} = \ln(1 + \varepsilon_{nom}) \tag{61}$$

The relationship between true stress and nominal stress is formed by considering the incompressible nature of the plastic deformation and assuming the elasticity is also incompressible:

$$l_0 A_0 = lA \qquad \Rightarrow \qquad A = A_0 \frac{l_0}{l} \tag{62}$$

Substituting equation (54) into equation (59):

$$\sigma_{true} = \frac{F}{A} = \frac{F}{A_0}\frac{l}{l_0} = \sigma_{nom}\left(\frac{l}{l_0}\right) \tag{63}$$

Then

$$\sigma_{true} = \sigma_{nom}(1 + \varepsilon_{nom}) \tag{64}$$

By joining the given data points, the smooth stress-strain behaviour of the material can be approximated with a series of straight lines in ABAQUS. The plastic data define the true yield stress of the material as a function of true plastic strain. The first piece of data given defines the initial yield stress of the material and, therefore, should have a plastic strain value of zero.

The strains provided by material test data used to define the plastic behaviour normally are not likely to be the plastic strains in the material. Instead, they are probably the total strains in the material, which must be decomposed into the elastic and plastic strain components. The plastic strain is obtained by subtracting the elastic strain, defined as the value of true stress divided by the Young's modulus, from the value of total strain (Fig. 52).

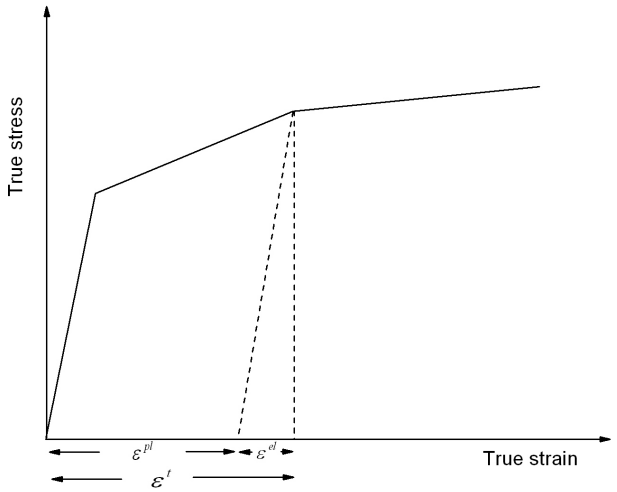

Fig. 52 Decomposition of the total strain into elastic and plastic components.

This relationship is written

$$\varepsilon^{pl} = \varepsilon^{t} - \varepsilon^{el} = \varepsilon^{t} - \frac{\sigma_{true}}{E} \tag{65}$$

where

ε^{pl} is true plastic strain,
ε^{t} is true total strain,
ε^{el} is true elastic strain,
σ_{true} is true stress, and
E is Young's modulus.

However, in practical engineering design, the stress situation is always very complex, so it is necessary to find some effective stresses to represent values that still give the correct failure conditions.

The von Mises effective stress is most widely used in this case both in the low and high temperature ranges. The physical interpretation of von Mises criterion suggests that yielding begins when the elastic energy of distortion reaches a critical value. For this reason, the von Mises criterion is known as the maximum distortion strain energy criterion.

It has been found that the deformation of materials under complex loading conditions, the creep rupture associated with large deformations and a ductile failure mechanism at high stress are all normally controlled by von Mises criterion.

However, the rupture in long-term situation is controlled either by maximum principal stress (MPS) or a combined MPS-von Mises criterion. Especially for brittle materials, the rupture tends to be more MPS controlled [4].

For the distortional energy (von Mises) criterion, the effective stress and strain are given by:

$$\bar{\sigma} = C_1\left[(\sigma_1-\sigma_2)^2+(\sigma_2-\sigma_3)^2+(\sigma_3-\sigma_1)^2\right]^{1/2}$$

and

$$d\bar{\varepsilon} = C_2\left[(d\varepsilon_1-d\varepsilon_2)^2+(d\varepsilon_2-d\varepsilon_3)^2+(d\varepsilon_3-d\varepsilon_1)^2\right]^{1/2} \qquad (66)$$

The constants C_1 and C_2 are chosen so that the effective stresses and strains are identical to the stresses and strains in uniaxial tension (or compression). For uniaxial tension:

$$\begin{aligned} &\sigma_1=\sigma_0 \qquad d\varepsilon_1 = d\varepsilon_1 \\ &\sigma_2=0 \qquad d\varepsilon_2 = \frac{-d\varepsilon_1}{2} \\ &\sigma_3=0 \qquad d\varepsilon_3 = \frac{-d\varepsilon_1}{2} \end{aligned} \qquad (67)$$

Substituting (67) into (66) gives:

$$C_1 = \frac{1}{\sqrt{2}} \qquad \text{and} \qquad C_2 = \frac{\sqrt{2}}{3}$$

Thus, the effective stresses and strains become:

$$\bar{\sigma} = \frac{1}{\sqrt{2}}\left[(\sigma_1-\sigma_2)^2+(\sigma_2-\sigma_3)^2+(\sigma_3-\sigma_1)^2\right]^{1/2}$$

and

$$d\bar{\varepsilon} = \frac{\sqrt{2}}{3}\left[(d\varepsilon_1-d\varepsilon_2)^2+(d\varepsilon_2-d\varepsilon_3)^2+(d\varepsilon_3-d\varepsilon_1)^2\right]^{1/2} \qquad (68)$$

4 Experiments and results

4.1 Equipment

4.1.1 Indentation machine

Contact experiments with controllable load rates and loading values were done with a universal testing machine (Instron Model 4502), as shown in Fig. 53. The sample is fixed onto a metal block with glue, which is clamped by the holders. A diamond indenter is mounted on the pedestal, which can be pushed up to the sample surface by moving upward. The loading value and rate are controlled by an electronic operating board. The machine allows accurate load rate between 0.001 mm/min and 25.4 mm/min.

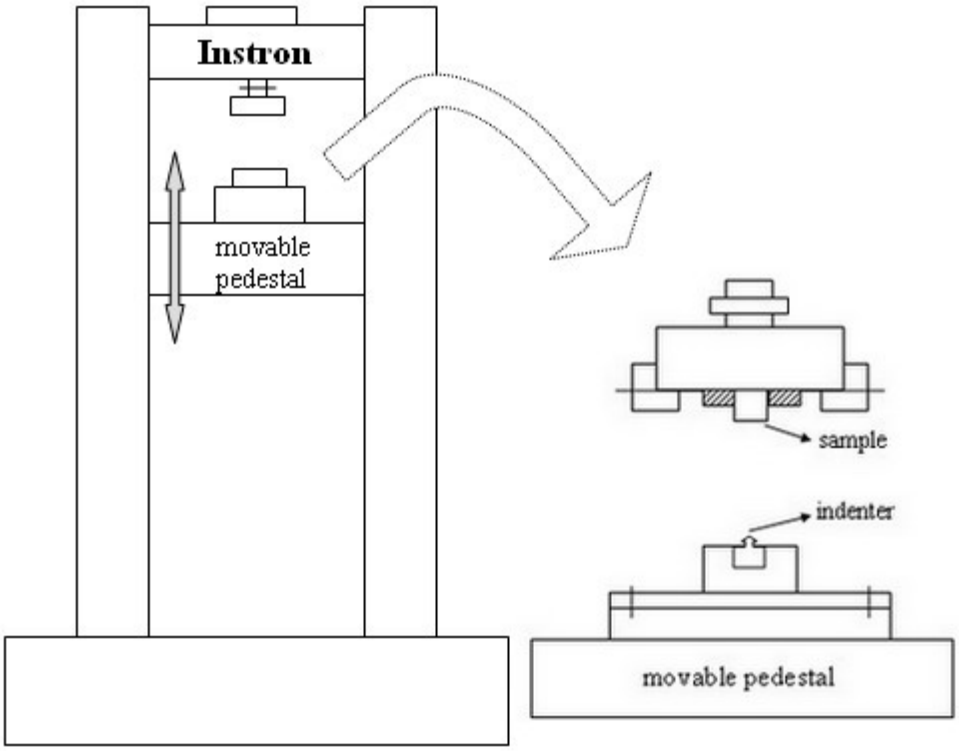

Fig. 53 Schematic drawing of universal testing machine (Instron Model 4502).

4.1.2 Material

The material used for this dissertation is tetragonal stabilized zirconium oxide ceramic (Vita, Germany). The samples are doped with 5 wt% Y_2O_3 (about 3 mol% Y_2O_3) and have a purity (Zr/Hf/Y) of 99.9 % and a density of > 6.05 g/cm³. The texture has a middle grain size of < 0.6

μm and no measurable open porosity (Table 9). These samples were cut to 10×20 mm and 3 mm thick pieces using standard techniques, and polished with 1 μm diamond polishing paste [131].

ZrO2 / Y2O3	95 / 5 wt%
Purity (Zr/Hf/Y)	99.9 %
Density	> 6.05 g/cm³
Average grain size	< 0.6 μm
Vickers hardness	1200 HV
Compression strength	2000 MPa
Bending strength	900 MPa
Elasticity modulus	210 GPa
Fracture toughness	7 MPa√m
Coefficient of linear expansion α	9.8 10^{-6}/°C
Heat conductivity λ	2.5 W/mK

Table 9 Material properties of 3Y-TZP[131].

4.1.3 Hardness testing

Vickers indentations with loads of 10 N, 20 N, 50 N, 100 N, 200 N and 500 N were made to determine the hardness of the material of the specimen. The loading rate is 0.01 mm/min., and the unloading rate is 0.1 mm/min. The edge lengths, diagonals and crack lengths of the indentations were measured and the hardness was calculated according to equation 3 (Chapter 4.2).

4.1.4 Microscopy

The indentations were investigated with optical microscopy (Olympus BH2-HLSH, Japan), with magnification of 5 times to 50 times. The software used to define the dimensions of indentations is Lucia Mutech-Version 4.61 for Nikon GmbH.

4.1.5 Raman spectrometer

Raman measurements were performed at room temperature in ambient using an optical spectrometer (Model HORIBA Jobin-Yvon, Dilor, France) with a CCD (charge coupled device)

detector (P358, 1152X298 pixel, Wright Instruments Ltd.). The Raman spectroscopy is equipped with two different lasers which make it possible to use three different excitation wavelengths (632.8 nm provided by the HeNe-laser; 488.0 and 514.5 nm provided by the Ar-Ion-Laser). Six available objectives (5x, 10x, 20x, 50x, 50xULWD, and 100x, BX40, Olympus) allow the micro-analysis with spot size ≥ 1 µm (Fig. 54). The Silicon Raman line at 520 cm^{-1} and diamond Raman line at 1330 cm^{-1} were used for wavelength calibration of the Raman lines. Wavenumbers ranged from 100 to 800 cm^{-1}. The obtained Raman spectra were analyzed using software Labspec.

To achieve a Raman measurement, the monochromatic laser light was focused onto the surface of the specimen. The scattered light was gathered by an objective, analyzed by a CCD camera and electronically evaluated.

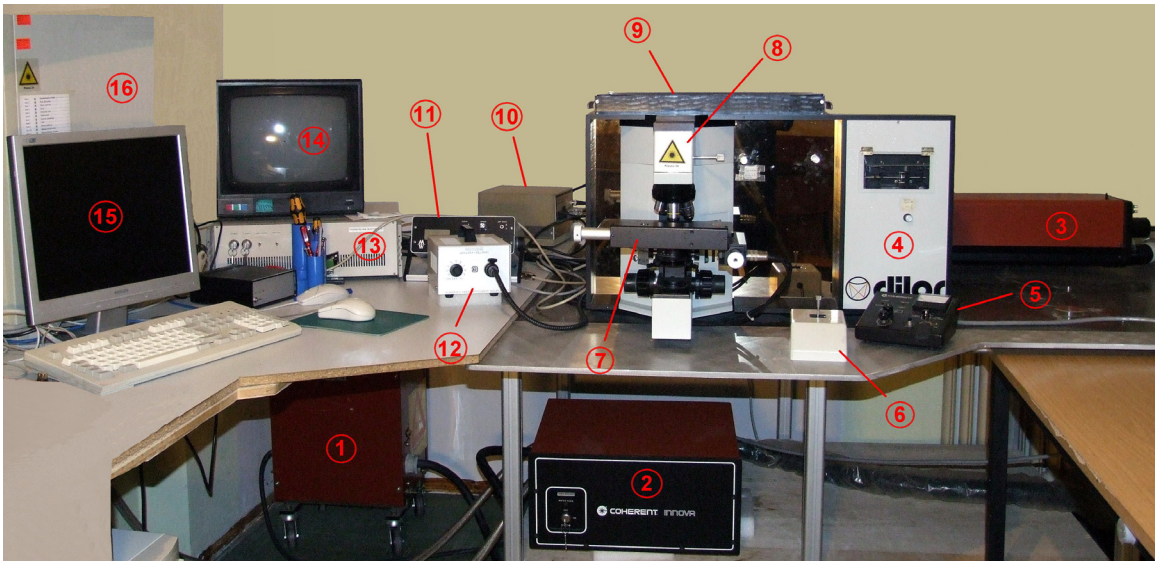

Fig. 54 Raman spectroscopy: (1)power transformer for external laser (2)control unit for external laser (3) external laser tube (4) spectrograph compartment (5) control panel for external laser (6) joystick (7) automatic XY-stag (8) microscope (9) optics compartment (10) control unit for CCD-detector (11) control unit for XY-stage (12) cold light source (13) control unit for spectrometer & internal laser tube (14) observation screen (15) computer screen (16) controlling computer.

Such a single-shot Raman measurement can take one second or several minutes, depending on the sample's Raman activity and further measurement parameters (radiation intensity, aperture and objective). For transparent samples it is also possible to measure the volume by focusing down into the interior as well as on the surface of the sample.

When operating with a scan mode, an area (multiple points, line or area) is selected from the optical picture and may be scanned by achieving multiple single measurements. But a correction of the focus position is not possible. Since the deviations from the focus position have extensive influence on the intensity of the Raman bands, scans are only reasonable for relatively even areas.

4.2 Results and discussions

4.2.1 Hardness and fracture toughness

The indentation depths at full loading were recorded during the testing. The behaviour of the depth according to the load was polynomial (Fig. 55 (a)). The dimensions of the indentation according to different forces, like edge and diagonal, are shown in Fig. 55 (b) and (c). The Vickers hardness was calculated at different loading forces (Fig. 55 (d)). The theoretical value of Vickers hardness (1200 HV) was proved. The average of the values is 1239.7 HV, with an error of 3.3%, which is acceptable. Indentation size effect, described in Chapter 3.1.5.3 cannot be seen here, because the forces used for this thesis were macro level.

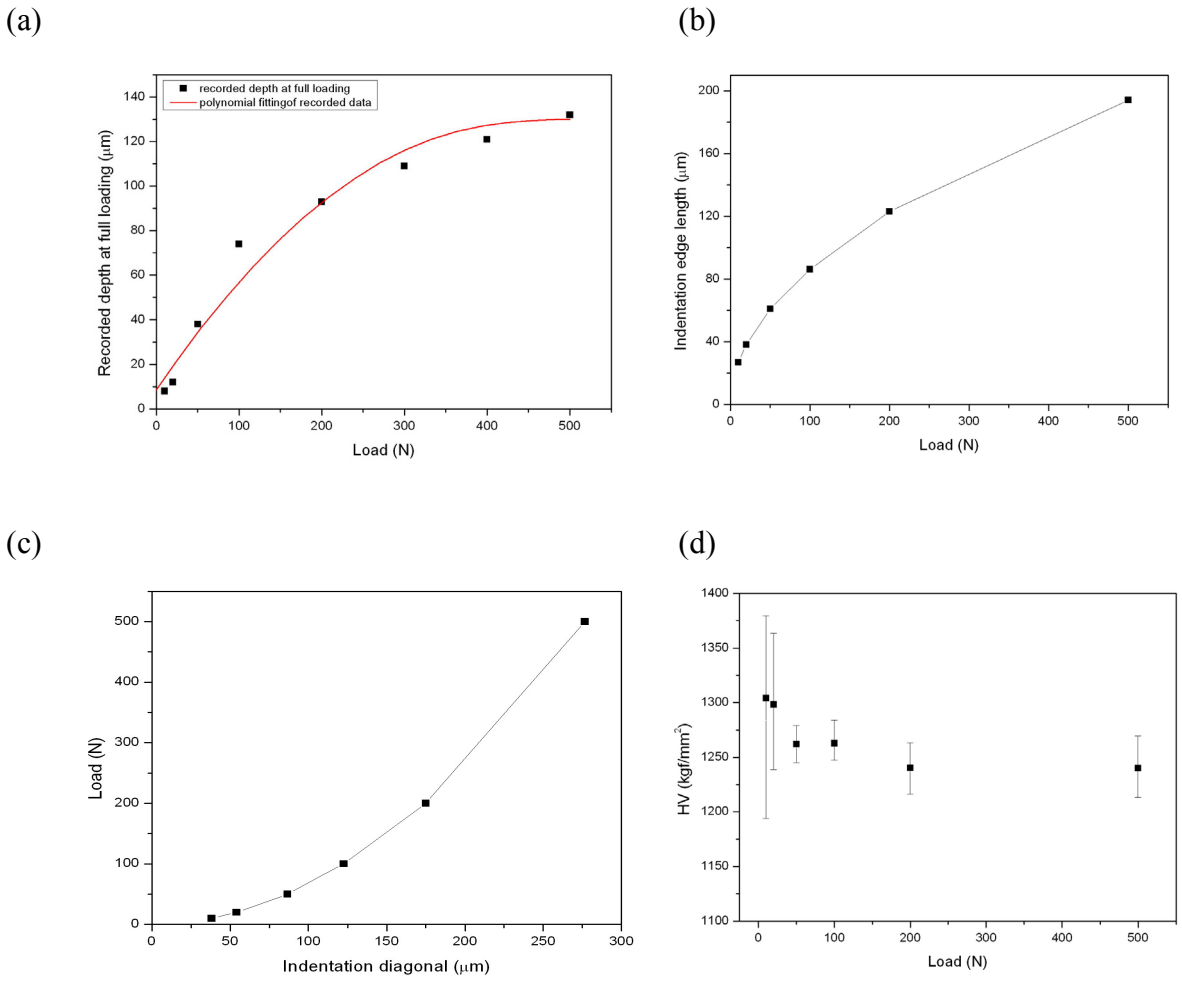

Fig. 55 (a) Depth at full loading vs. load, (b) indentation edge length vs. load, (c) load vs. indentation diagonal, and (d) Vickers hardness vs. load.

As a comparison to Vickers indentations, Rockwell indentations were also made. Fig. 56 (a) is the plotting of Rockwell indentation radii against loads, and (b) is the comparison of the projected

areas for Vickers and Rockwell indentations. At the same load, the projected area for Rockwell is larger than Vickers.

(a) (b)

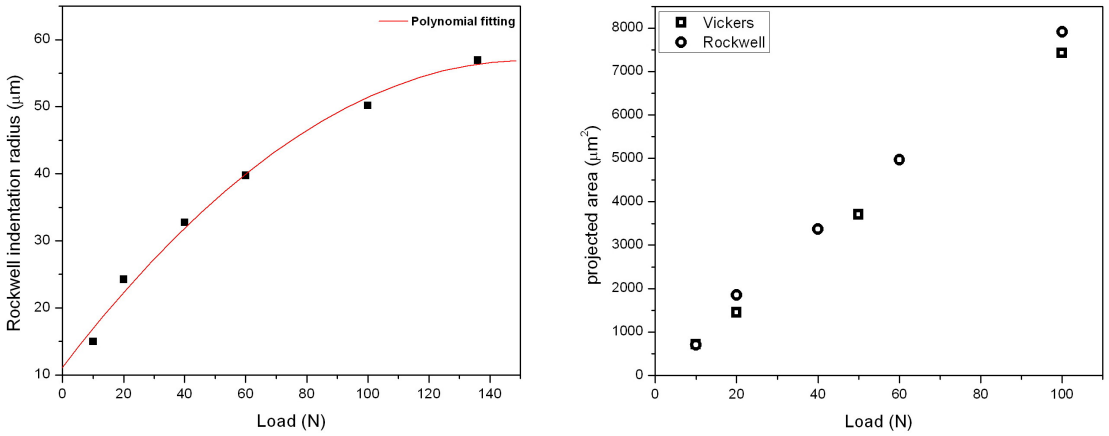

Fig. 56 (a) Rockwell indentation diameter vs. load, and (b) projected area vs. load.

Kaliszewski et al. [75] studied the relationship of surface crack length and the load for 3-mol% yttria-stabilized zirconia ceramic, and revealed that the crack length varied with $P^{2/3}$ at high indent loads (>500 N, logP~2.7), and the slope of linear fitting is 0.71. The log-log plot of indentation load (10~500 N) and the surface crack length is shown in Fig. 57, combined with the results from Kaliszewski et al. at higher loads. The slope of the linear fitting is about 1.1, larger than the ones for higher loads.

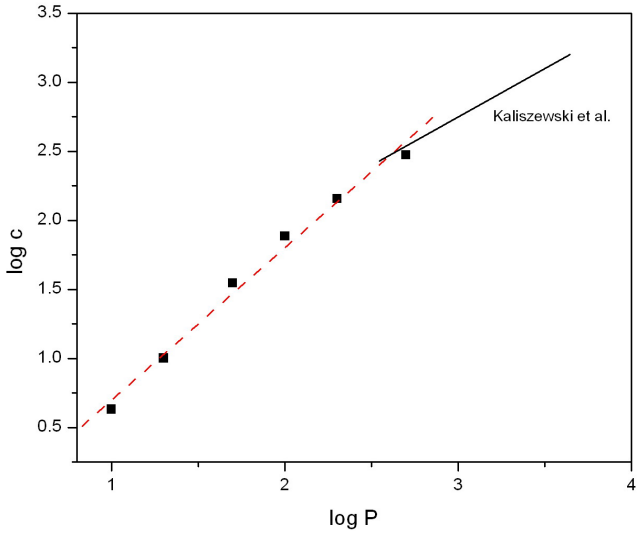

Fig. 57 Log-log plot of indentation load vs. crack length.

The ratio of $P/c^{1.5}$ is a constant as mentioned by Lawn et al., which is about 36.5 $MPa\sqrt{m}$. There have been various formula built for different kinds of cracks using different indenters to calculate

the fracture toughness, which is discussed in Chapter 3.1.5.4. It is important to choose the suitable one for the Vickers indenter, with a ratio of *c/a* less than 2.5. It is accepted here that only radial cracks occur, which can be combined with the extended median cracks to produce half-penny cracks.

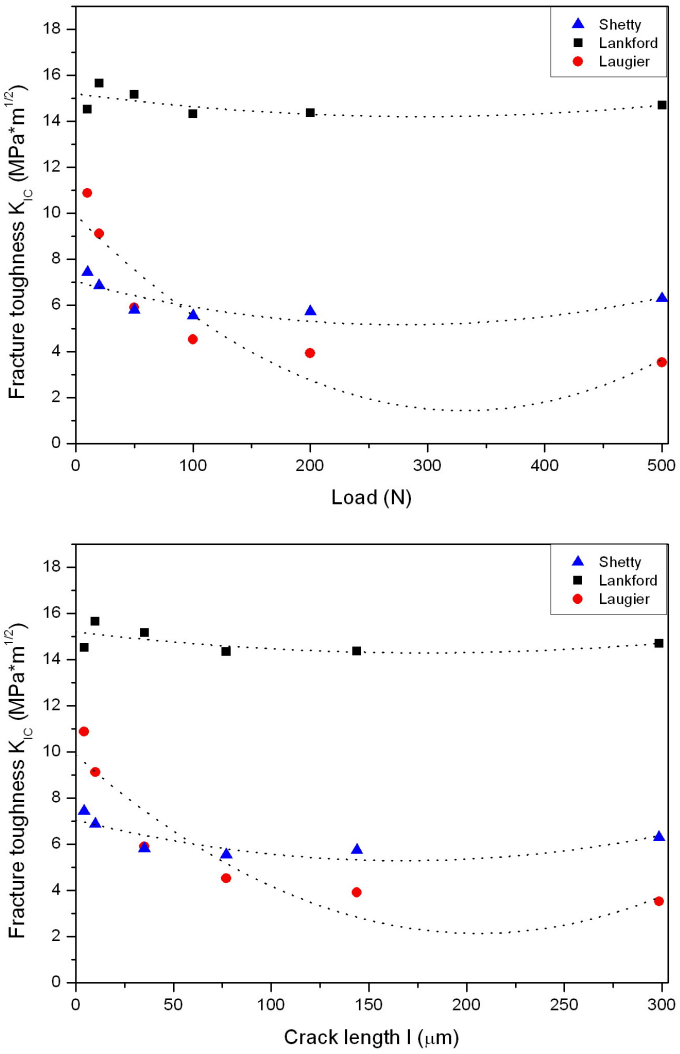

Fig. 58 Fracture toughness vs. load (upper) and crack length (lower).

Fracture toughness as a function of loads and crack length is shown in Fig. 58. The fitted plots of the fracture toughness values from equation (17) and (18) are nearly parallel, while the latter is double the former. The result from equation (19) shows a different behaviour for half-penny crack, where the fracture toughness decreases with increasing load and crack length. However the K_{IC} results from equations (17) and (18) do not depend on load and crack length as in equation (19), and are almost horizontal.

The average value of fracture toughness according to equation (17) is 6.3 $MPa\sqrt{m}$, which is very close to the theoretical number (K_{IC}=7 $MPa\sqrt{m}$), with an error of 10%. This amount comes from the error of measuring; at the end of the crack, the trail is too weak to define the precise length.

R-Curve, which shows the increasing of the toughness during crack extension, has an effect on the calculation of K_{IC} (Chapter 3.2.6). When the crack length is longer, the transformed zone will be larger, thus the change of the fracture resistance is greater. When the R-Curve is a constant, it has no influence on the value of fracture resistance. Under the circumstance of resistance increase, the crack cannot only be described through fracture toughness, because now it may be closed due to two mechanisms: microcracks and stress-induced transformation toughening, discussed in Chapter 3.2.5. The fracture toughness cannot be zero, because the resistance itself cannot be zero. The most suitable formula used in calculating fracture toughness was never decided until recently, and the current finding is still only comparably reasonable.

4.2.2 Analysis of Raman spectroscopy

4.2.2.1 Determination of integral band intensities

Fig.59 shows the method used to determine band intensities by means of two boundaries used in the LabSpec analysis software. This method is necessary when the phase percentage must be calculated on the basis of the intensities of Raman bands, which are influenced by different phases. Therefore, the area under the line will be calculated generally. The difference spectrum shows the exact differences of the two spectra. Intensities below the y=0 line show the decrement of the tetragonal intensities, and the above ones show the increment of the monocline intensities. Additionally, the tetragonal Raman band at 640 cm^{-1} was used as an example to show the determination of the intensities. In order to avoid error, the restrictions should be put down preferentially at the zero positions of the difference spectrum.

There are three different ways to calculate:

(1) The junctures of the boundary intersections in the spectrum form the base line of the embedded area (I), which is denoted by the LabSpec software as Raman intensity.
(2) The intersections of the boundaries and the x-axis form the base line of the embedded area. The perpendiculars from the intersections to the x-axis delimitate the area in addition. This is denoted as Fluo intensity (I+II).
(3) The particular band intensities are determined by fitting using Gauss-/Lorentz-curves (band fitting, see also chapter 4.2.2.4).

The first two methods contain inaccuracies in the determination of band intensities. Usually there are no Raman bands, which show perfect Gauss-Lorentz-distribution and moreover unequivocal difference from other Raman bands, such as the characteristic spectra of diamond or silicon. Though, in the superimposition of two widened and narrowly-joined Raman bands, the base line

can move upward (Fig. 57, at 150 and 350 cm^{-1}) when using the first method, and thus a much inferior intensity is determined. The application of the second method, however, also cannot deliver exact calculation of the intensity because the use of vertical restrictions of the base line of a Gauss-Lorentz-distribution is cut off on both sides. Ideally the determination of band intensities should be carried out by means of a band fitting, in which every Raman band is modelled in intensity, FWHM, Gauss/Lorentz-ratio and position.

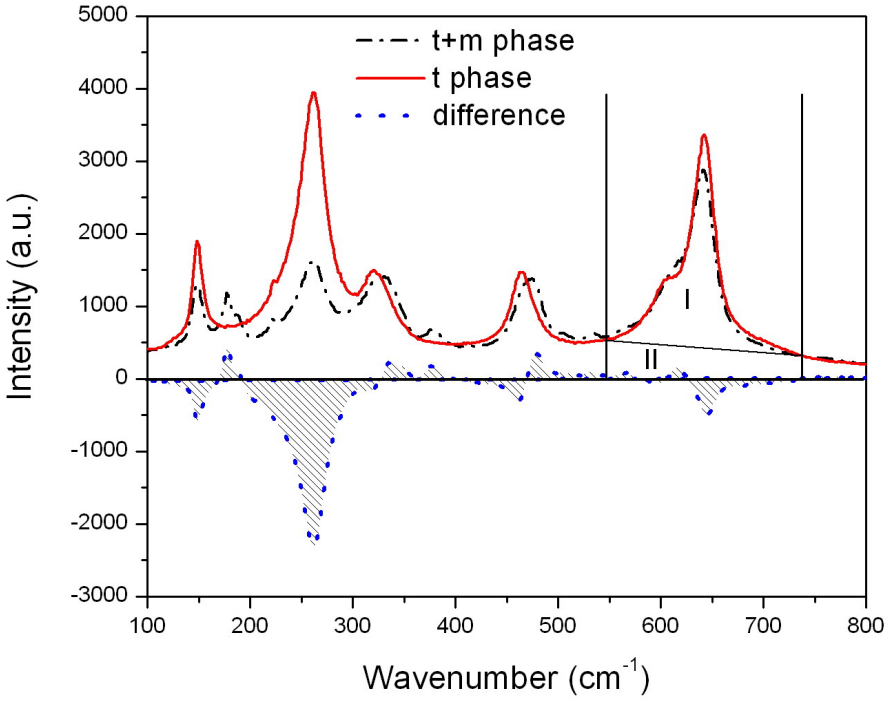

Fig. 59 Raman spectra of tetragonal phase and spectrum with an additional fraction of monoclinic phase (black dash dot line is t+m phase, red solid line is tetragonal phase, blue dot line is the difference of the two spectra).

The measurement and evaluation software LabSpec offers, as mentioned, three possibilities to determine band intensity. All can be applied to single spectra as well as to line or area measurements. In order to prove the precision of the controversial band intensities, a theoretical Lorentz function can be generated:

$$y = \frac{aw^2}{w^2 + 4(x-p)^2} \tag{69}$$

where a is the amplitude of the band, w is the width at half-maximum, and p is the position of the band. With the obtained x and y values, a spectrum is simply generated in the LabSpec software, and the intensity determination under application of the different possibilities is executed.

4.2.2.2 Overlaps in Raman spectra

In Raman spectra of a mixture of monoclinic and tetragonal phases after a transformation from tetragonal to monocline with mechanical exposure, for example, after indentation experiments, both phases can be observed simultaneously. Because of overlaps with tetragonal bands, not all known monocline bands can be clearly observed in the Raman spectrum. Overlaps can also cause widening of bands and formations of shoulders when bands with high intensities lie narrowly together. However, the monocline bands at 181/190 cm^{-1}, 379 cm^{-1} and 538/557 cm^{-1} can be easily identified in the monocline-tetragonal spectrum. Overlaps of the tetragonal bands at 322 and 464 cm^{-1} and the monocline bands at 333 and 475 cm^{-1} lead to the mentioned band widening. Many monocline bands are low in intensity so that they can influence the spectrum by a slight increment of the underground. These bands cannot be identified in monocline-tetragonal spectra. An example of a spectrum with monocline and tetragonal fractions is given in Fig. 59.

The spectrum of the tetragonal phase far away from an indentation in the 3Y-TZP sample serves as a reference measurement. At the edge of an indentation, where a tetragonal-monocline transformation takes place, additional monocline Raman bands, intensity fluctuations, band shifts and band widening can be observed.

The magnitude of these effects depends on the degree of transformation and on the quantity of monocline phase. By subtracting the band intensities of the mixed m-t spectrum by the reference substance, alterations in the Raman spectrum can be shown very clearly. Intensities below the y=0 line show the decrement of the tetragonal intensities, and the above ones show the increment of the monocline intensities.

4.2.2.3 The background noise in Raman spectra

Algorithms are always used to calculate the intensities of Raman signals, which create distribution curves with reference to their type (Gauss/ Lorentz function), their intensities and their FWHM (full width at half maximum). The greatest error that can arise is caused by the subtraction of the background noise, because the base of the distribution, and thus relatively large intensity, is influenced.

4.2.2.3.1 Linear background subtraction

The easiest way to subtract the background from the spectrum is to use a constant and linear line (Fig. 60 upper). This background fits the Raman spectrum very well at lower wavenumbers and at higher wavenumbers than 1000 cm^{-1}. But the band fitting (Fig. 60 lower) for Raman signals of tetragonal phase is not satisfying, because the obtained intensities of the individual band around 200, 400, 550 and 750 cm^{-1} are too low compared with the measured spectrum.

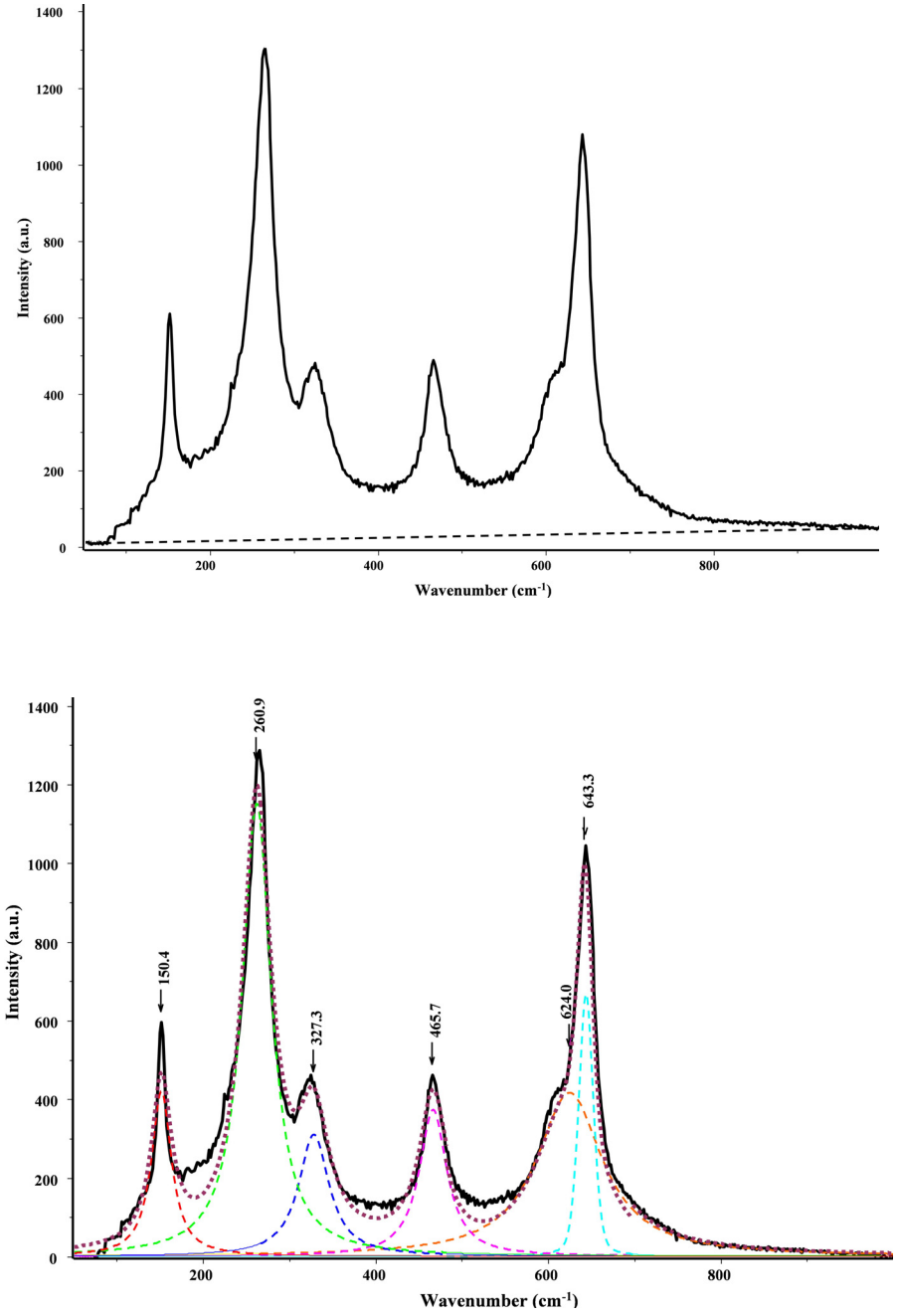

Fig. 60 Linear background subtraction (upper) and Gauss/Lorentze fitting (lower) of a ZrO_2 spectrum.

4.2.2.3.2 Polynomial background subtraction

By using a polynomial background profile it is possible to raise the range between 200 and 700 cm^{-1} in order to decrease the error described for linear fitting. However, it is apparent that in the band fitting there still exists a relatively large error (Fig. 61). This comes from the fact that not enough of the background was subtracted in this area.

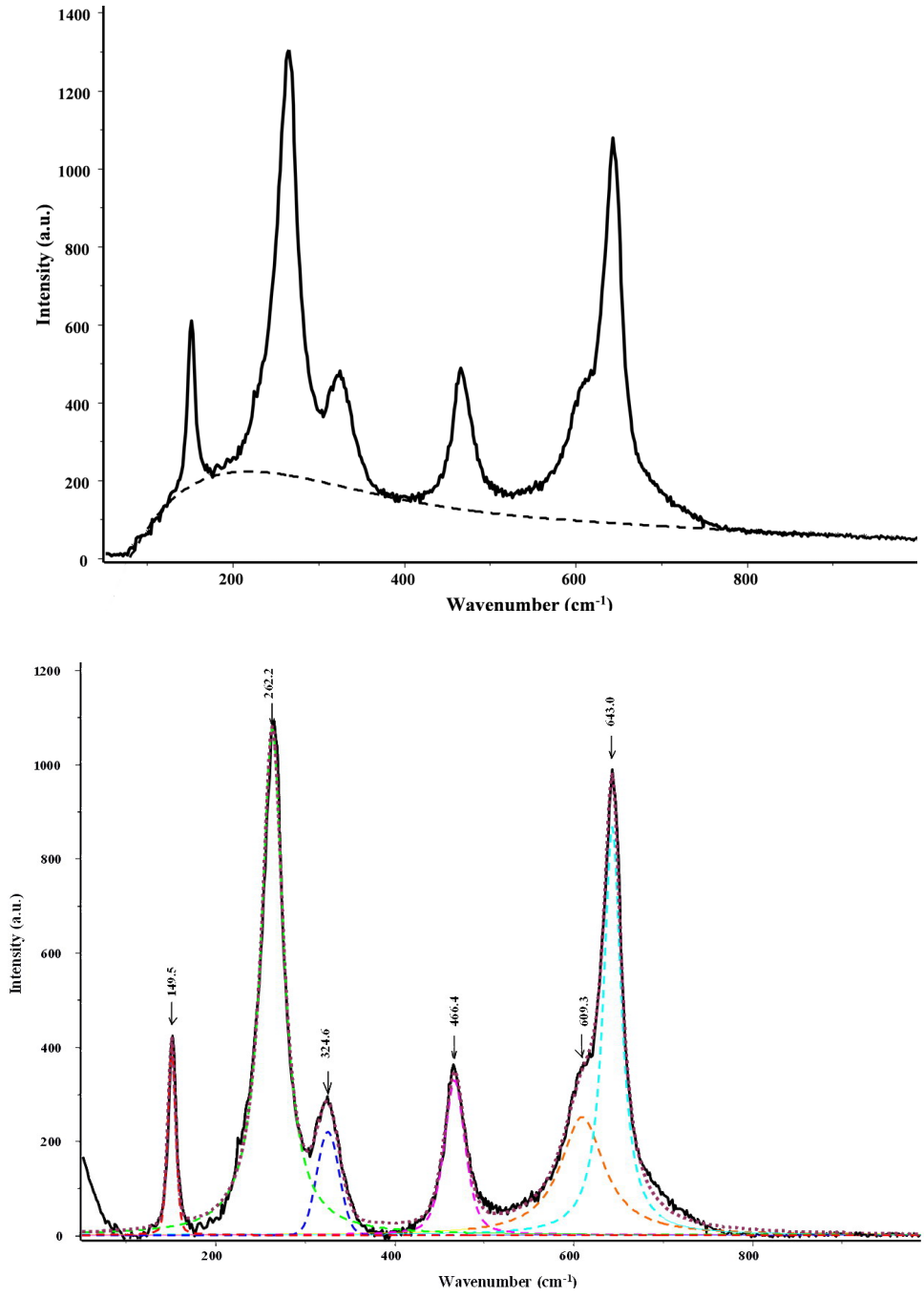

Fig. 61 Polynomial background subtraction (upper) andGauss/Lorentze fitting (lower) of a ZrO_2 spectrum.

4.2.2.3.3 Folded line background subtraction

A folded line connecting the lowest points is an easy and direct way to subtract the background. Because the area around bands 300 and 500 cm^{-1} was subtracted better in this way than with polynomial subtraction, the error between measured and fitted bands is smaller (Fig. 62). In the following chapters if there exists no special remark, the Raman spectra will be treated in this way.

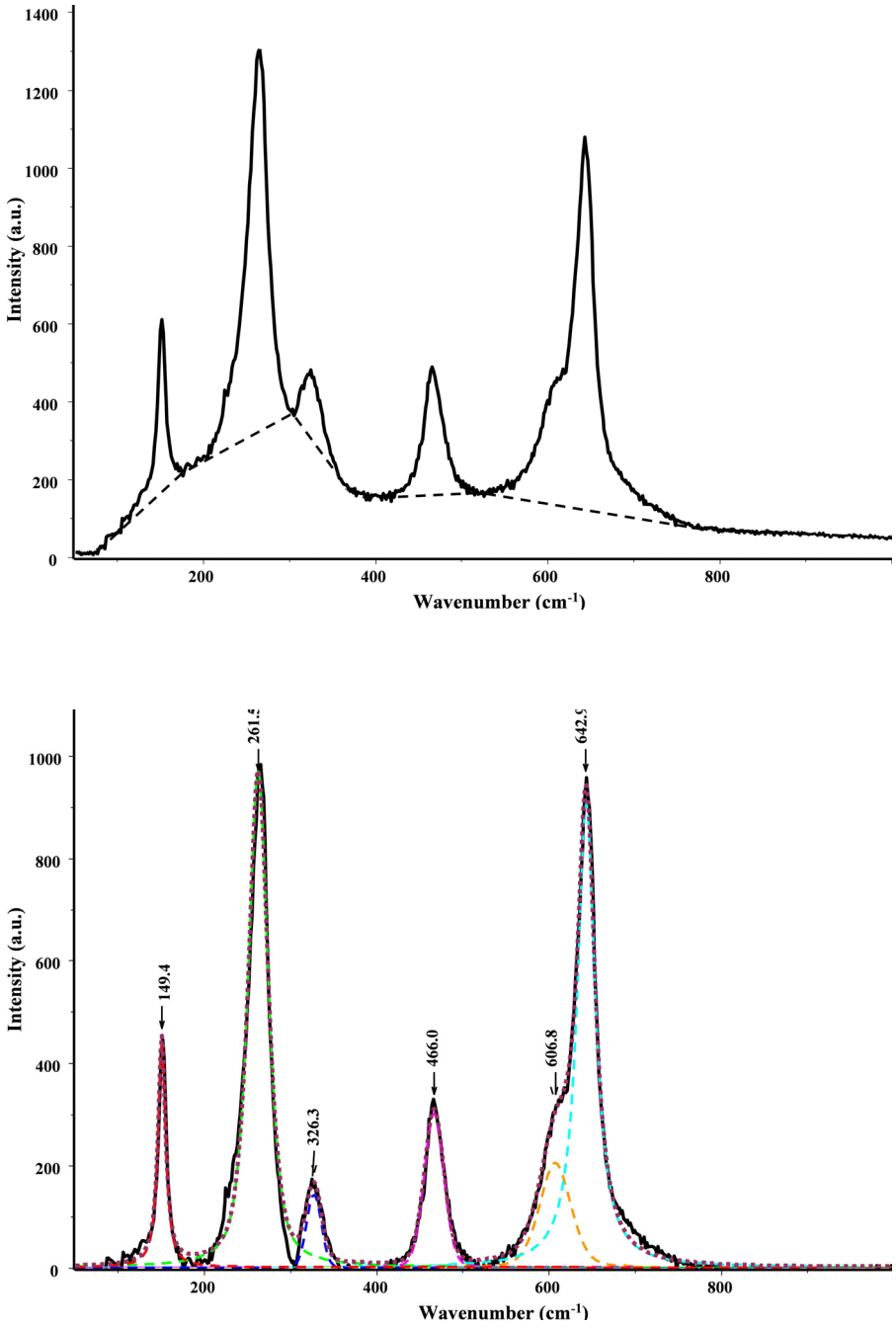

Fig. 62 Folded line background subtraction (upper) and Gauss/Lorentze fitting (lower) of a ZrO_2 spectrum.

4.2.2.4 Focusing the laser beam on the sample surface

In Raman measurements the focusing of laser on the sample surface may deviate when the surface is rough or fractured during automatic line or area scans. This leads to the change in band intensities. Fig. 63 is the schematic diagram of three forms of Raman beam focus. The left focuses below sample surface, the middle on the surface and the right above the surface. When the laser is focused below the sample surface, the illuminated sample volume is much larger than the other two, and more information from the material can be collected.

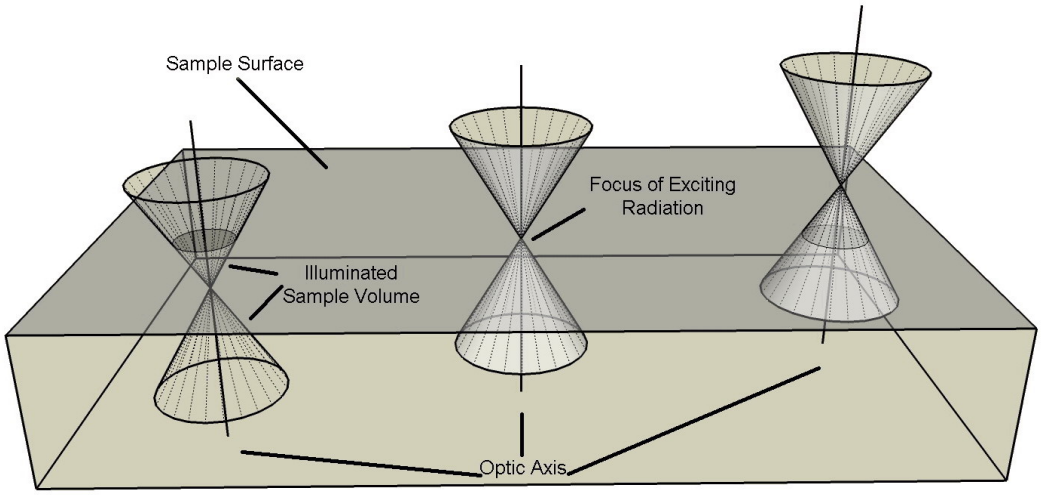

Fig. 63 Schematic diagram of three forms of Raman beam focus. Left focuses below sample surface, middle on the surface and right above the surface.

In order to make the influence clear, three kinds of samples were tested with a defocusing test using blue light with wavelength 488 nm. Cubic ZrO_2, diamond and quartz were chosen to represent transparent materials, while Silicon represents opaque material and baddeleyite (Uganda) and 3 mol% Y_2O_3-TZP are in-between.

The relationship between defocus distance and band intensity of cubic ZrO_2, diamond and quartz is shown in Fig. 64 (from Fig. 64 to Fig. 66, a positive defocus distance value means the focusing point is above the sample surface, while a negative distance means the focusing point is below the sample surface).

The common behaviour for these three materials denotes that the highest intensity is not located at the sample surface, and the intensity increases rapidly downwards from the surface intensity. When the focusing point approaches the sample surface, the lower part of the illuminated volume becomes increasingly immersed in the sample until the point is below the sample surface. Then more scattered light contributes to the Raman spectrum.

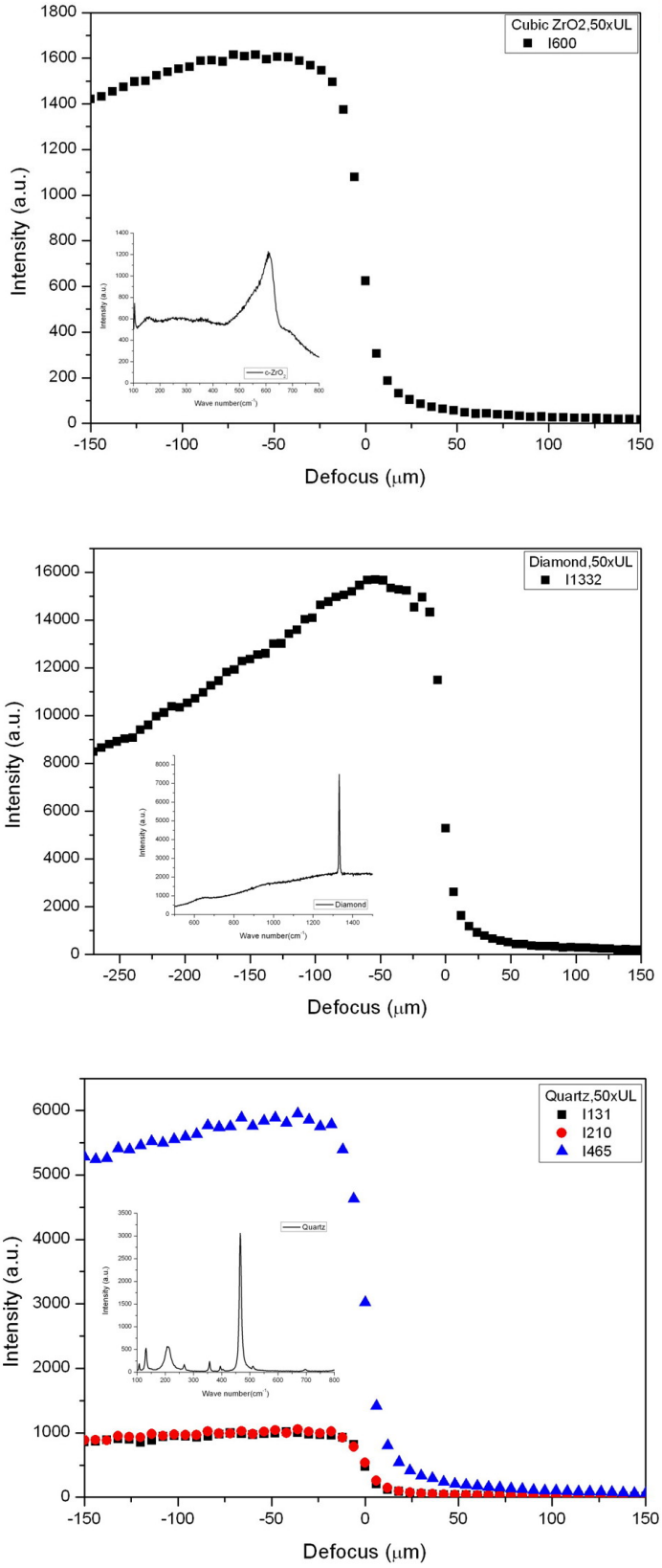

Fig. 64 Defocus distance vs. band intensity for cubic ZrO_2 (upper), diamond (middle) and quartz (lower).

However, there is a finite probability of Raman photons, generated at any point within the illuminated volume, being scattered in a suitable direction as to be detected. Therefore, after the

maximum position, the intensity will decrease with further defocus depth, leading to asymmetrical distribution of the intensity about the focusing point.

The relationship between defocus distance and band intensity of Silicon is shown is Fig. 65. For all four measurements, the maximum intensity of band 520 cm^{-1} is at the focus point on the sample surface, giving a symmetrical distribution of the intensity about focusing point. This is because Silicon is a type of opaque material. The Raman-intensity of the illuminated volume below the surface is suppressed by the absorption of the material, and has no extra influence on the final result.

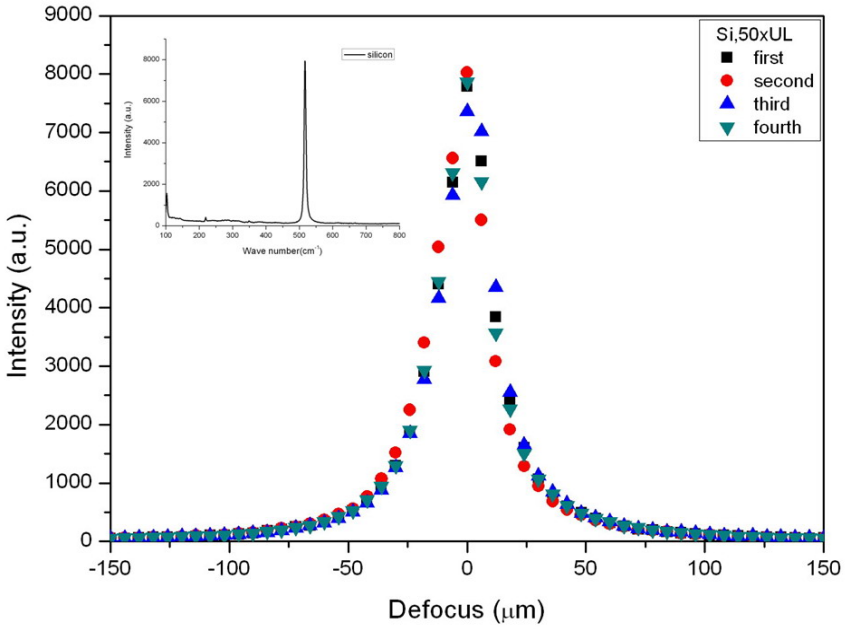

Fig. 65 distance vs. band intensity of Silicon.

Fig. 66 is the relationship between defocus distance and band intensity of baddeleyite (Sukulu, Uganda. Crystals extracted from residual soil overlying carbonatite), 3 mol% Y_2O_3-TZP and Zircon (with coating of baddeleyite, Mabuki Diamond Mine, Tanganyika). The highest intensity for all three materials is not located on the focused surface, rather a certain micrometer under the surface. The intensities of main bands of baddeleyite reach maximum values of about 12 μm below the sample surface. Even zirconia is a type of transparent material from the theoretical viewpoint, but because of the polycrystalline property, the intensity of incident light encountering grain boundaries decreases after continuously reflecting. The depth of penetration to reach the maximum intensity is much lower than the materials in Fig. 64.

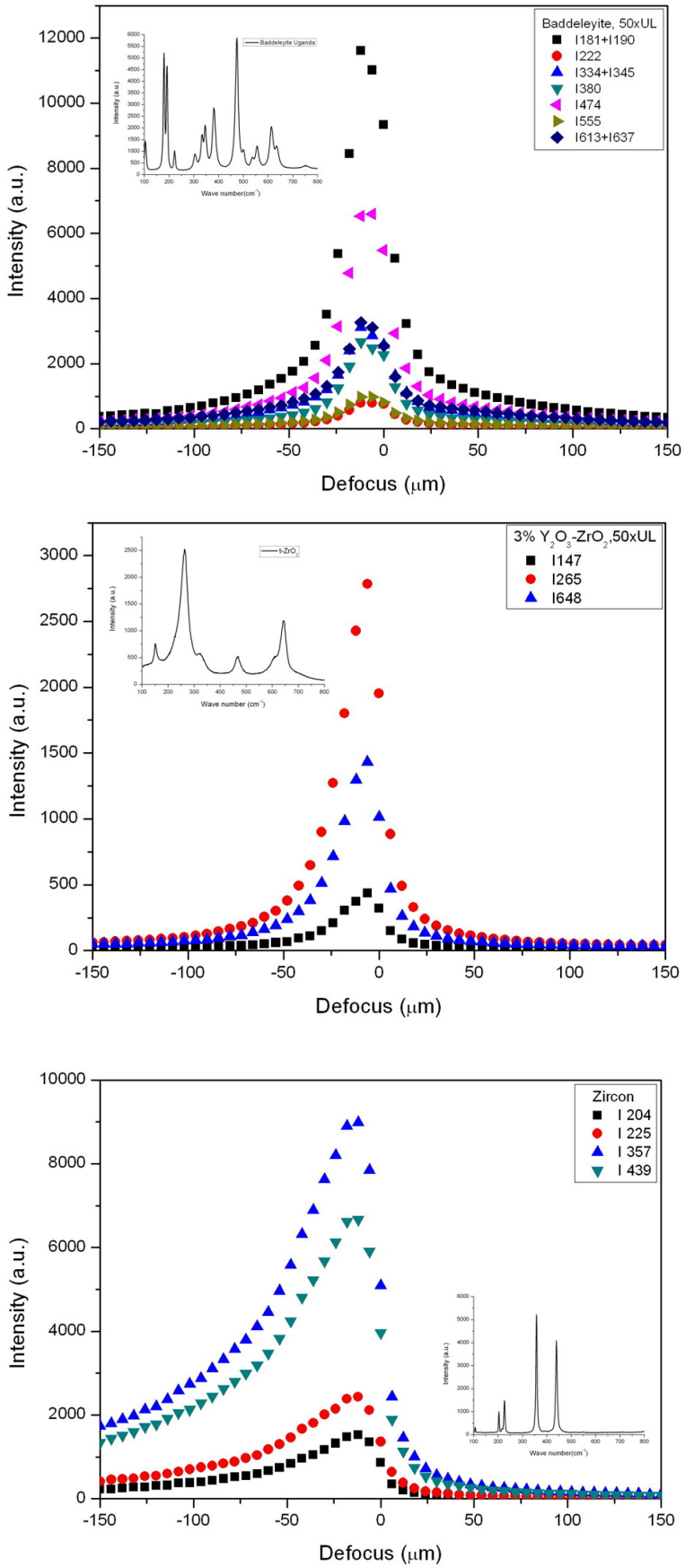

Fig. 66 Defocus distance vs. band intensity for baddeleyite (upper), 3 mol% Y_2O_3 -TZP (middle) and zircon (lower).

4.2.2.5 Calculation of the monoclinic fraction

4.2.2.5.1 Calculation of the monoclinic-cubic fraction

Kontoyannis and Carountzos quantitatively determined the cubic and monoclinic phases of zirconia through the pressed pellets from monoclinic-cubic powder mixtures [132]. This method was independent of the origin of the materials and could be easily used for providing similar analyses of polycrystalline PSZ and FSZ materials in which the cubic phase was present.

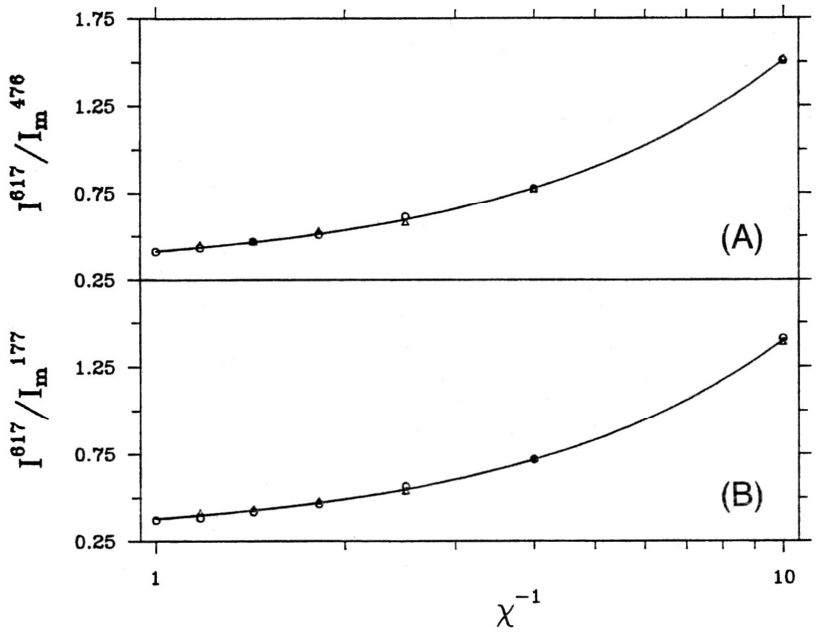

Fig. 67 Plots of the ratios of the Raman band at 617 cm^{-1} of the cubic phase and the bands at 476 cm^{-1} (A) and 177 cm^{-1} (B) of the monoclinic phase with the molar fraction of the monoclinic phase[132].

The 177 and 476 cm^{-1} bands of the monoclinic phase, and the 617 cm^{-1} band of the cubic phase were chosen for the quantitative study. Instead of using integrated intensities, which is normal in dealing with the Raman spectra, the band height was used. Shown in Fig. 67 are the plots of the ratios of the Raman band at 617 cm^{-1} of the cubic phase and the bands at 476 cm^{-1} (A) and 177 cm^{-1} (B) of the monoclinic phase, with the molar fraction of the monoclinic phase. From the plots, the following equations to calculate the monoclinic fraction χ were generated:

$$\frac{I^{617}}{I_m^{496}} = \frac{1}{\chi} 0.12 + 0.29 \qquad (70)$$

$$\frac{I^{617}}{I_m^{177}} = \frac{1}{\chi} 0.11 + 0.26 \qquad (71)$$

The largest standard error from rough estimation among these calculations of the monoclinic-phase molar fraction was considered to be approximately ±2.1%.

4.2.2.5.2 Calculation of the monoclinic-tetragonal fraction

Fig. 68 (a) is a typical image of indentation, which was achieved under 100 N with 20 times magnification. A spatial mapping of monoclinic phase around such indentations will be shown in the next step. Raman spectra obtained at different distances from the indentation edge are shown in Fig. 68 (b). It can be clearly observed that the monoclinic doublet (the bands at 181 cm^{-1} and 190 cm^{-1}) vanished along the path.

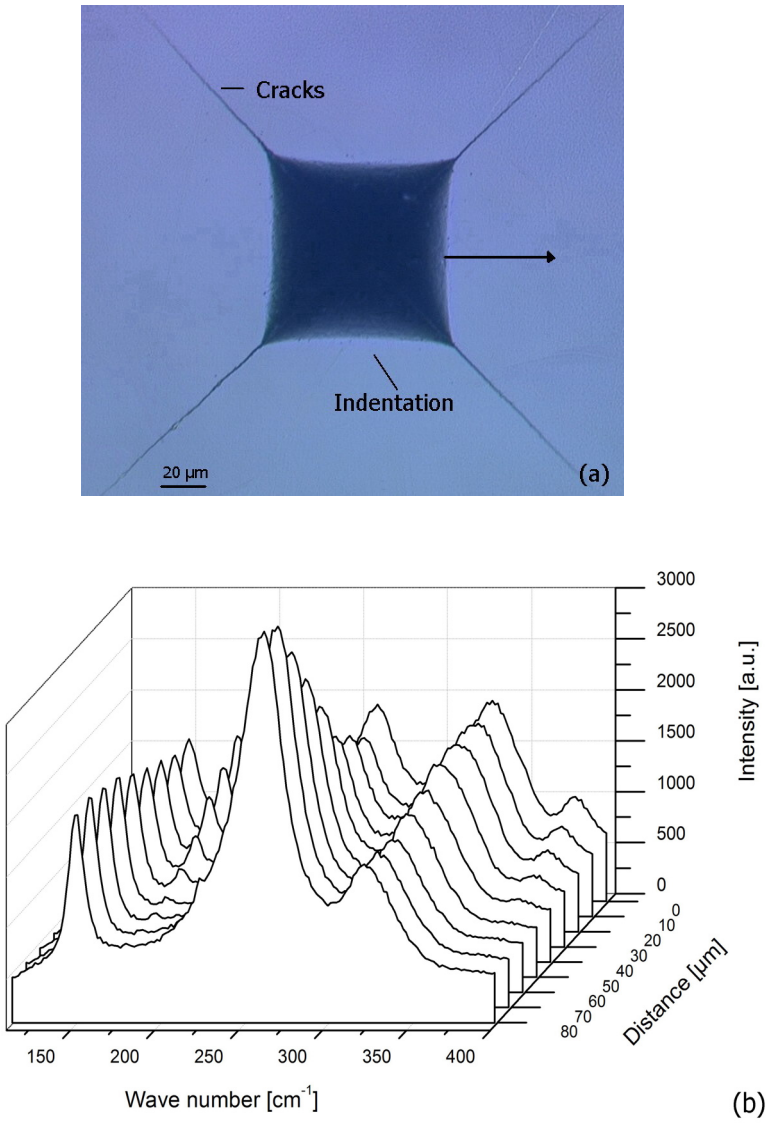

Fig. 68 (a) Magnified image of an indentation with the mapping path. (b) Raman spectra obtained at different distances from the indentation edge.

There are two methods to calculate the fraction of monoclinic phase: (72) was modelled by Clarke and Adar [74, 133]. In equation (72), I_m is the intensity value of monoclinic bands at 181 and 190 cm^{-1}, I_t is that of tetragonal bands at 147 and 265 cm^{-1} (intensity calculated using area under the curve). The use of fact F (=0.97) is to correlate the Raman and XRD intensities. (73) was modelled by Dorn and Nickel [129] because of the strong dependence of band 265 cm^{-1} on polarisation. The calculation of monoclinic fraction was improved in equation (73), where I_m is the same as in equation (72); I_t is the intensity value of tetragonal bands at 648 cm^{-1} which is rotation-independent (intensity calculated using area under the curve). Fact K (=0.42) is used to get similar values to the monoclinic phase in (72).

$$C_{m1} = \frac{I_m^{181} + I_m^{190}}{F * (I_t^{147} + I_t^{265}) + I_m^{181} + I_m^{190}} \tag{72}$$

$$C_{m2} = \frac{I_m^{181} + I_m^{190}}{K * I_t^{648} + I_m^{181} + I_m^{190}} \tag{73}$$

It is known that the fracture toughness is dependent on the transformability of tetragonal phase [55, 134]. This equation is proposed:

$$K_{IC} = K_{IC}^m + \frac{\eta V_f \Delta V E \sqrt{d}}{1 \quad \nu} \tag{74}$$

where K_{IC} is the actual fracture toughness, K_{IC}^m is the fracture toughness without tetragonal to monoclinic transformation, η is a constant, V_f is the fraction of transformed tetragonal phase, ΔV is the volume expansion due to the transformation, E is Young's modulus, d is the half width of the transformation zone (the width where the fraction monoclinic phase decreases to *1/e* of the fraction monoclinic phase at the edge) and ν is Poisson's ratio. It is clear that except $V_f\sqrt{d}$ the others values are constants, so the fracture toughness is a function of $V_f\sqrt{d}$. The parameters are η=0.23, ΔV=0.05, E=220 GPa, ν=0.28 and K_{IC}^m=3 $MPa\sqrt{m}$ [81, 134, 135]. In order to calculate the fracture toughness, a scratch was made on the surface of the sample and the Raman spectra were measured, departing from the scratch. Using equation (73) the fraction monoclinic phase was calculated from Raman spectra (Fig. 69). With reference to the edge of the scratch, the fraction monoclinic phases are about 0.56, and the width of the transformation zone is estimated to be about 9 μm. The $V_f\sqrt{d}$ is 1.68, and the corresponding fracture toughness is 7.17 $MPa\sqrt{m}$, which is in good agreement with the theoretical value.

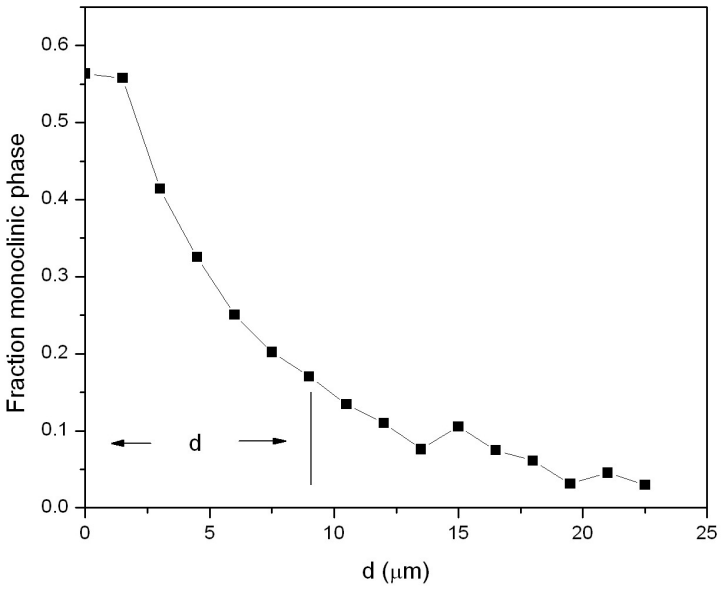

Fig. 69 Monoclinic phase distribution of a 3Y-TZP sample as a function of the distance from the scratch.

From Fig. 70 to Fig. 72, mapping of monoclinic phase fraction using equation (73) has been done for indentations with 100 N, 250 N and 500 N, respectively. The pictures on up side are surfaces of indentations (red dot lines inside represent size of indenter), while the ones below are for cross-section.

The measurements are found using an area scan of Raman spectroscopy, manually focusing on every point. The experimental data was treated using Origin (Microcal Software) and Labspec v4.02 (DILOR) software. Baselines were subtracted before any curve fitting.

From all three pictures for planar plotting, monoclinic phase especially can be seen along the cracks starting from indentation tips, cracks which form lines with an angle of about 45° from the horizontal line. The distance required for monoclinic phase to appear depends on the force. The highest monoclinic phase fraction concentrates around the corners of the indentations because they have the highest stress distribution. The global distributions of monoclinic phase present approximate circular contours, with radii 80, 120 and 175 μm for 100 N, 250 N and 500 N, respectively.

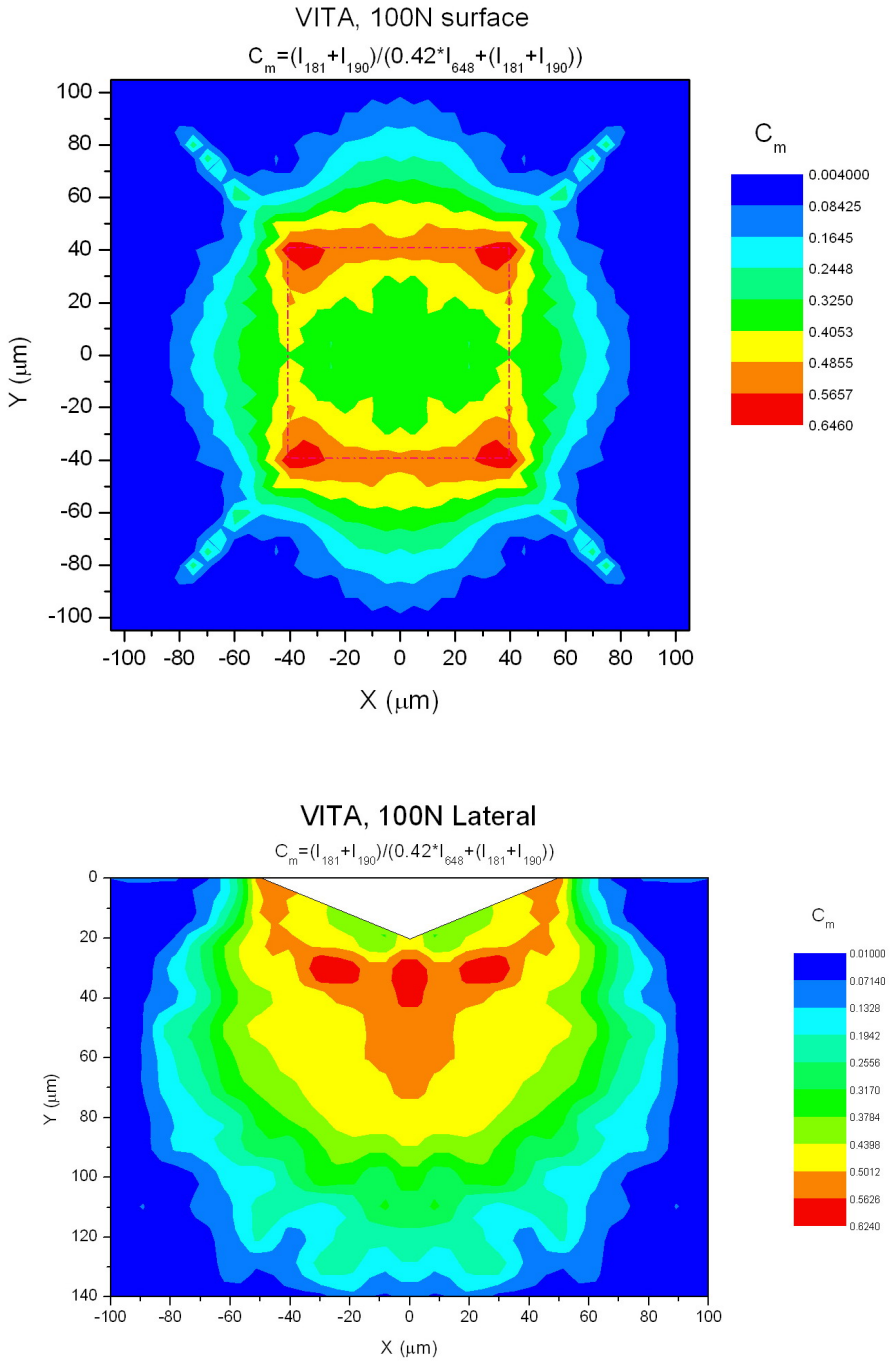

Fig. 70 Surface (upper) and cross-section (lower) mapping of m-phase around an indentation of 100 N.

The indentation depths are 20, 32 and 48 μm for 100 N, 250 N and 500 N, respectively. The monoclinic zone beneath the indenter has a spherical contour, and the maximum depths that monoclinic phase may reach are 140, 200 and 275 μm for 100 N, 250 N and 500 N, respectively. The highest monoclinic phase fraction zones are not directly below the indenter; rather, they exist as a ring-shaped zone with a certain distance around the indenter. This distance depends on the magnitude of the pressure: the greater the pressure, the longer the distance.

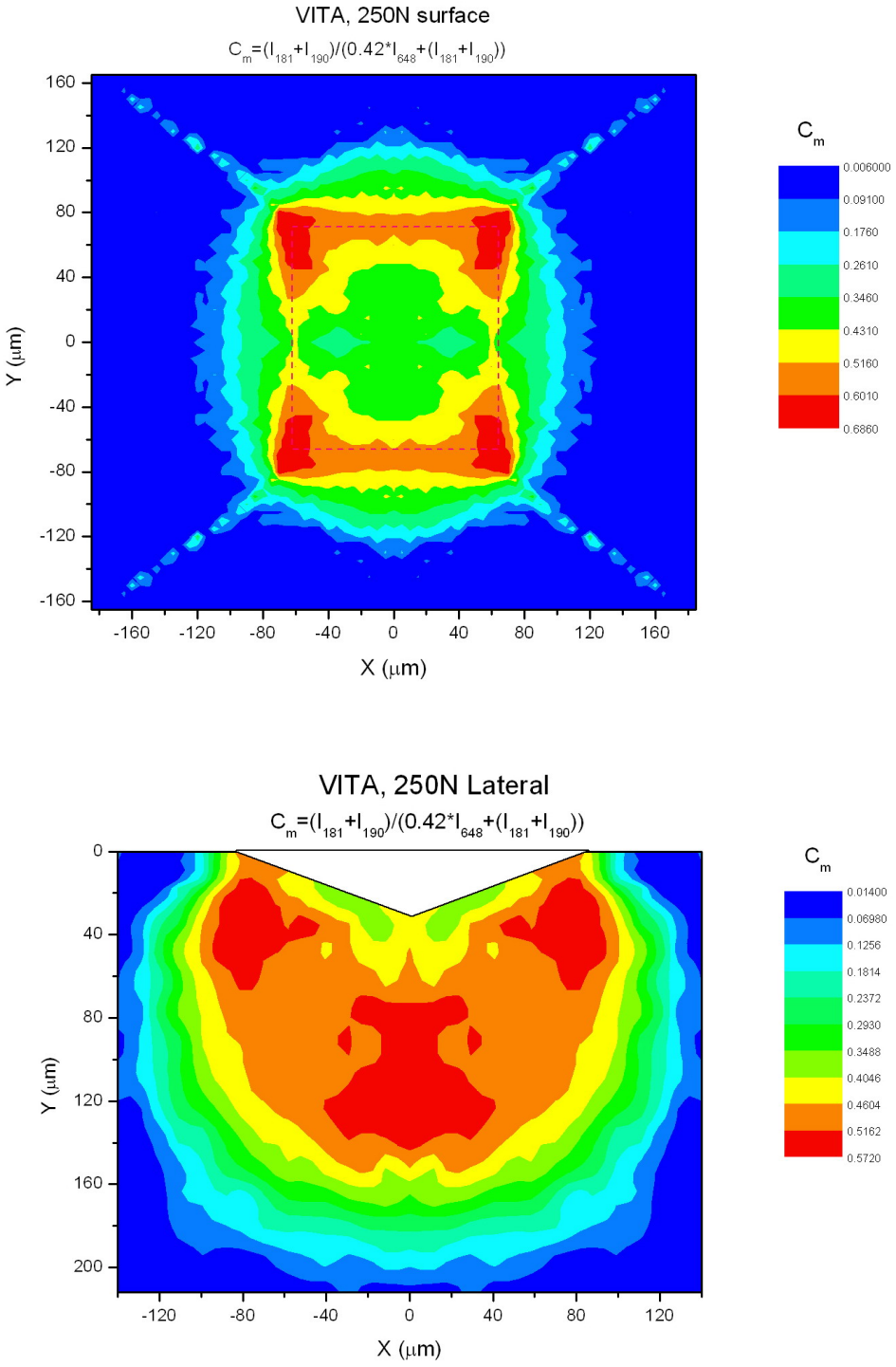

Fig. 71 Surface (upper) and cross-section (lower) mapping of m-phase around an indentation of 250 N.

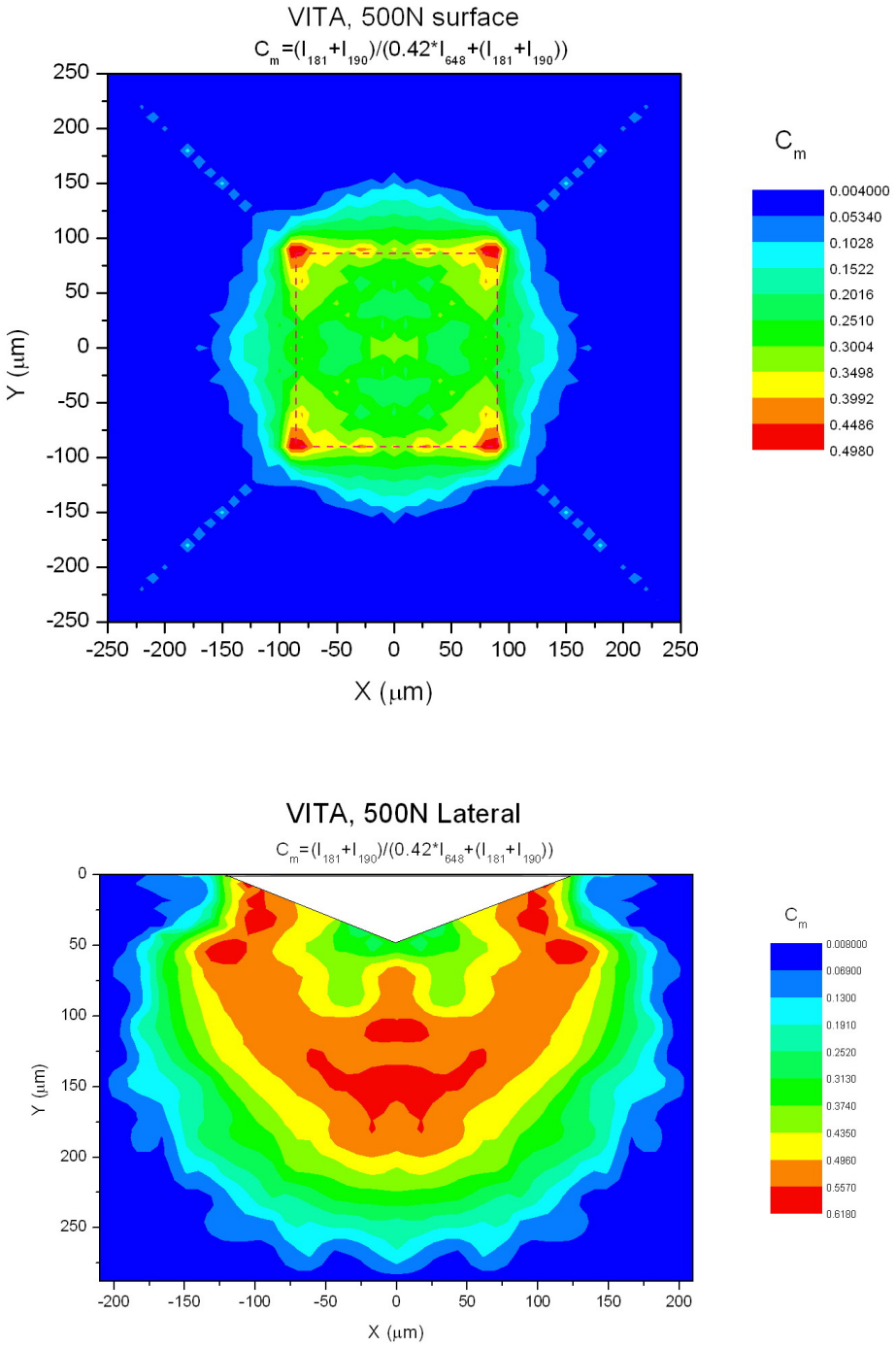

Fig. 72 Surface (upper) and cross-section (lower) mapping of m-phase around an indentation of 500 N.

4.2.2.6 Residual stress analysis from Raman spectra

Determination of the magnitude and distribution of residual stress field is helpful in understanding the deformation and fracture properties during sharp indentation in brittle materials. Different methods have been developed to reach this target, such as Raman spectroscopy [136-139], X-ray [140, 141], photoelasticity [142], fluorescence spectroscopy [143], hole drilling [144] and layer

removal, etc. However, regarding the measurement accuracy, spatial resolution, materials geometries and feasibility, a different method will be chosen. Raman scattering method has been used as a powerful non-destructive method to characterize the local residual stress information with micron-meter order, in which even the measured area is limited to indentation edge. Residual stress of different Zirconia ceramics has been studied in the past using Raman spectroscopy [145-148].

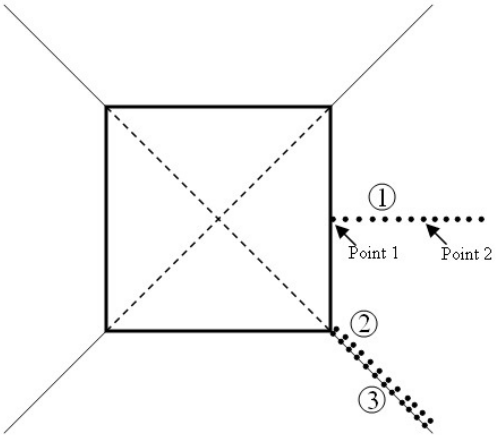

Fig. 73 Schematic drawing of line scans.

Three line scans for an indentation with load of 100 N have been done here. Line 1 started from middle of vertical indentation edge, line 3 lies on the crack and line 2 was very close to line 3 (Fig. 73). Both point 1 and 2 located on line 1, point 1 was close to the indentation edge, and 44 μm away from point 1 was point 2. The peak fitting and data processing are the same with that described in Chapter 4.2.4.

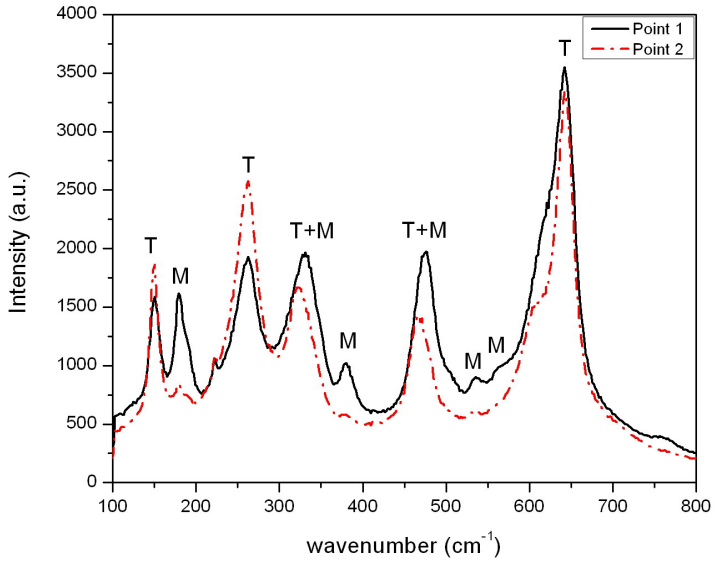

Fig. 74 Comparison of peak positions of point 1 and point 2 for Raman spectra.

Residual stress field around an indent can be investigated using Raman microscopy, based on the well-known fact that Raman signals (phonon energies) can be affected by internal stresses. In a Raman spectrum of deformed material, the positions of the peaks will shift relative to ones obtained from stress-free material. Quantifying such shifts gives the magnitude of internal stress. Fig. 74 shows the peak shift of Raman spectra according to the different positions related to the indentation. While a shift to higher wavenumbers is due to compressive stress, shift to lower wavenumbers indicates tensile stress.

The shifts of five major bands of 3Y-TZP as a function of applied stress were characterized by Cai [108] (Table. 7, Chapter 3.3.5.3). This material band at 261 cm^{-1}, as an exception, shifts to lower wavenumbers under uniaxial pressure.

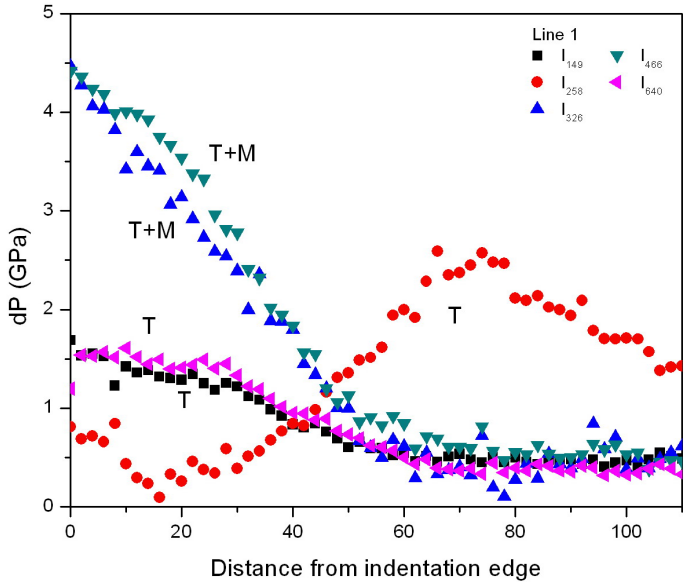

Fig. 75 Stress field for the indentation of 100 N force.

To show the stress distribution, an indentation of 100 N was considered. Measurements started from the middle point of the vertical indentation edge, and peak positions were determined by fitting the measured intensity with a Gaussian function. Five main peaks show three different kinds of behaviours (Fig. 75): values from bands at 326 and 466 cm^{-1} close to the indentation edge are about three times of those of bands at 149 and 640 cm^{-1}. The band at 258 cm^{-1} shows a completelydifferent tendency from the others, behaves like a cosinusoid. Bands at 326 and 466 cm^{-1} have high values because monoclinic and tetragonal phases simultaneously exist at the same wavenumbers and together contribute to the shifts. The special behaviour of band at 258 cm^{-1} is due to the softening of the mode with the hydrostatic component of stress [108, 114]. As a result, the stress values calculated from bands at 149 and 640 cm^{-1} are more reasonably used to indicate the true residual stress field.

In Fig. 76, linear and polynomial subtractions were done to show the different stress values caused by different background-dealing methods as described before in Chapter 4.2.2. Stress curves for bands at 326 and 466 cm^{-1} close to the indentation edge separated, and the ones for bands at 149 and 258 cm^{-1} had a continuous problem with linear subtraction. This proves again to the significance of choosing a suitable way to deal with the spectra.

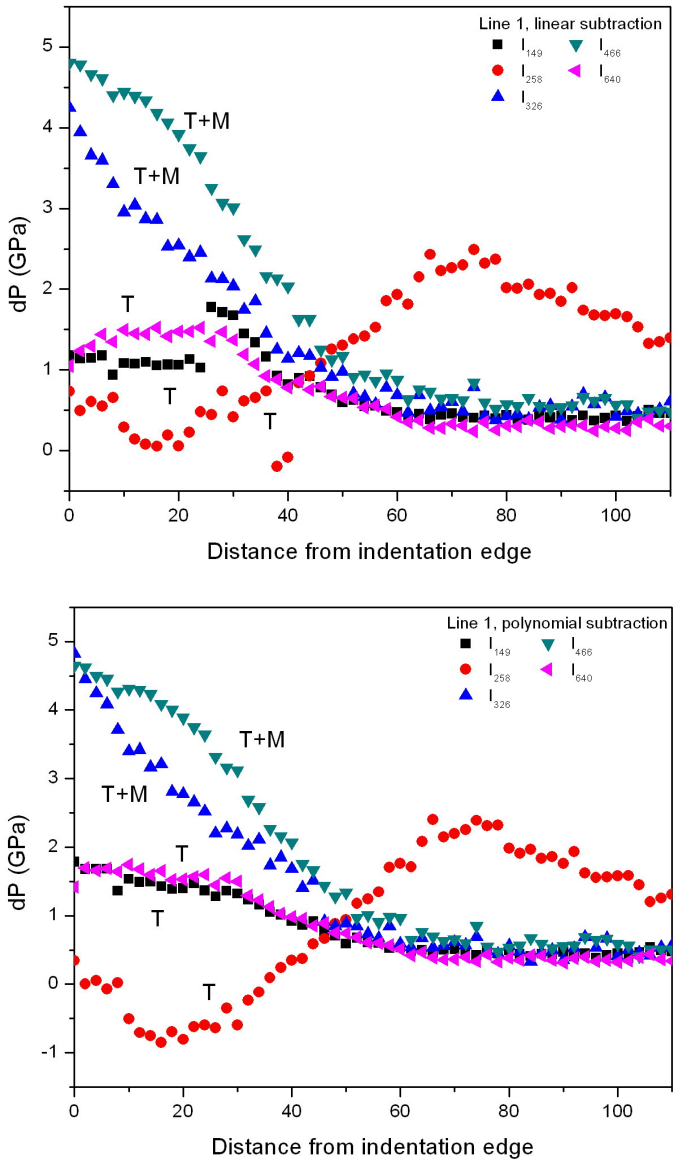

Fig. 76 Stress fields for the indentation of 100 N force with linear subtraction (upper) and polynomial subtraction (lower), respectively.

The relationship between the residual stress and monoclinic phase content of line 1 calculated from Eq. (73) is shown in Fig. 77. The residual stress corresponding to the highest monoclinic phase fraction 40%, which is located on the edge of the indentation, is about 1.5 GPa. From bands at 149 and 640 cm-1 when the residual stress is about 1 GPa, monoclinic phase fraction is around 15%.

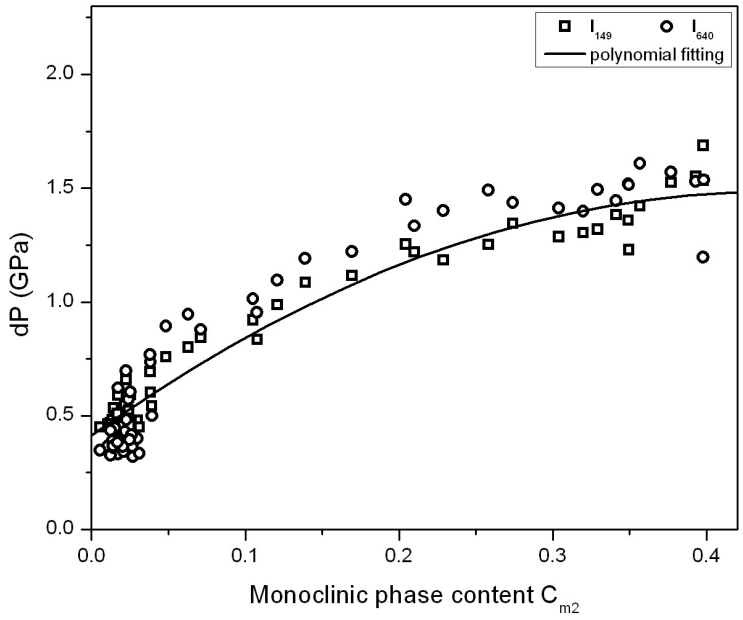

Fig. 77 Plot of residual stress and monoclinic phase content (Eq. (64)).

The calculation of stress distribution along lines 2 and 3 in Fig. 73 is shown in Fig. 78. The results from line 2 show similar behaviour to line 3, but with higher values. This is because line 3 is located exactly on the crack where more stress can be released than in other places.

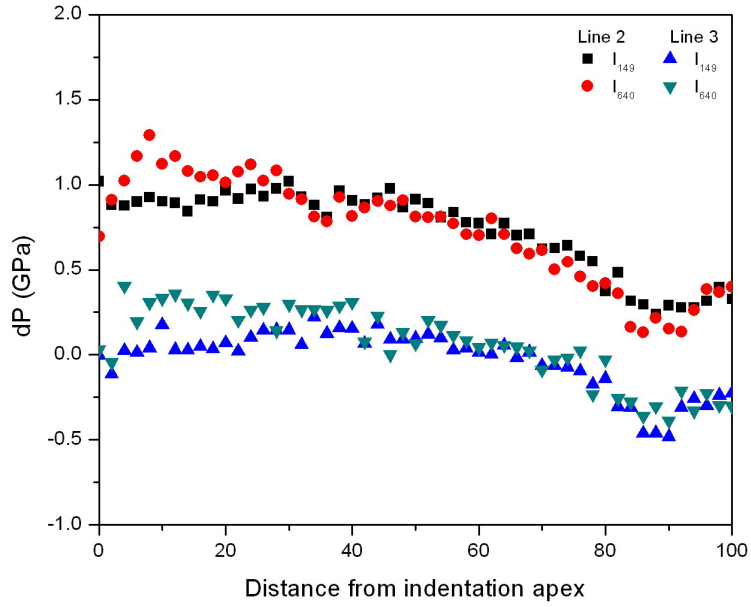

Fig. 78 Stress distribution of line 2 and 3 for the indentation of 100 N force.

4.2.3 The finite element model

4.2.3.1 Two-dimensional FEM simulation

Two-dimensional finite element modelling (FEM) simulations were done using the commercial software ABAQUS/standard Version 6.5 and 6.7 (HKS Ins., Pawtucket, RI). According to the symmetry, geometric models of 2D were shown in Fig. 79.

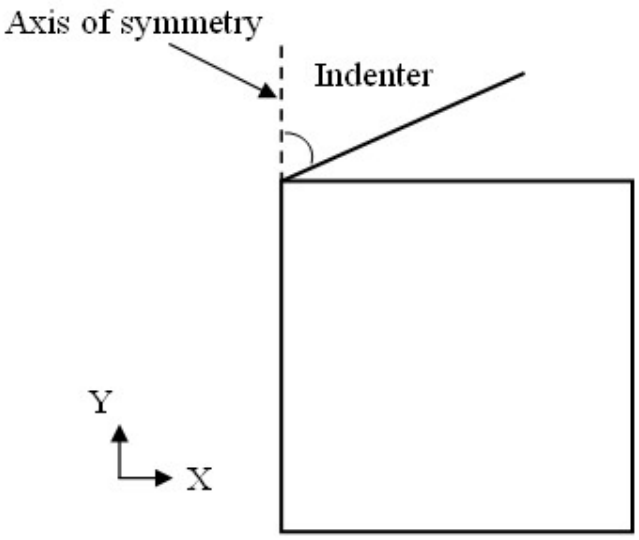

Fig. 79 Two-dimension geometry of indentation process (not to scale).

In 2D simulation, the diamond indenter was assumed to be a rigid conical indenter with a 70.3° semi-angle [4, 149], which had the same area function as a perfect Vickers four-sided pyramidal indenter. A contact model was used for such simulations. Fine finite element meshing was used in the vicinity of the contact region underneath the indenter. A gradually coarser meshing was used away from the contact region to reduce the computational time and ensure a high degree of accuracy. The meshing comprised of 5421 nodes and 1750 elements belonged to the CAX8R (8-noded biquadratic axisymmetric quadrilateral) category. During the analysis, loading was achieved by displacing the rigid indenter downward along the Y axis (Fig. 80). To unload, the indenter was displaced upwards back into the original position. The boundary conditions were defined as: (1) the bottom edge U1=U2=UR3=0; (2) the symmetric center U1=UR2=UR3=0. The loading and unloading curves could be obtained directly from the ABAQUS output of the reaction force in the normal direction on the rigid indenter as a function of the indenter vertical displacement.

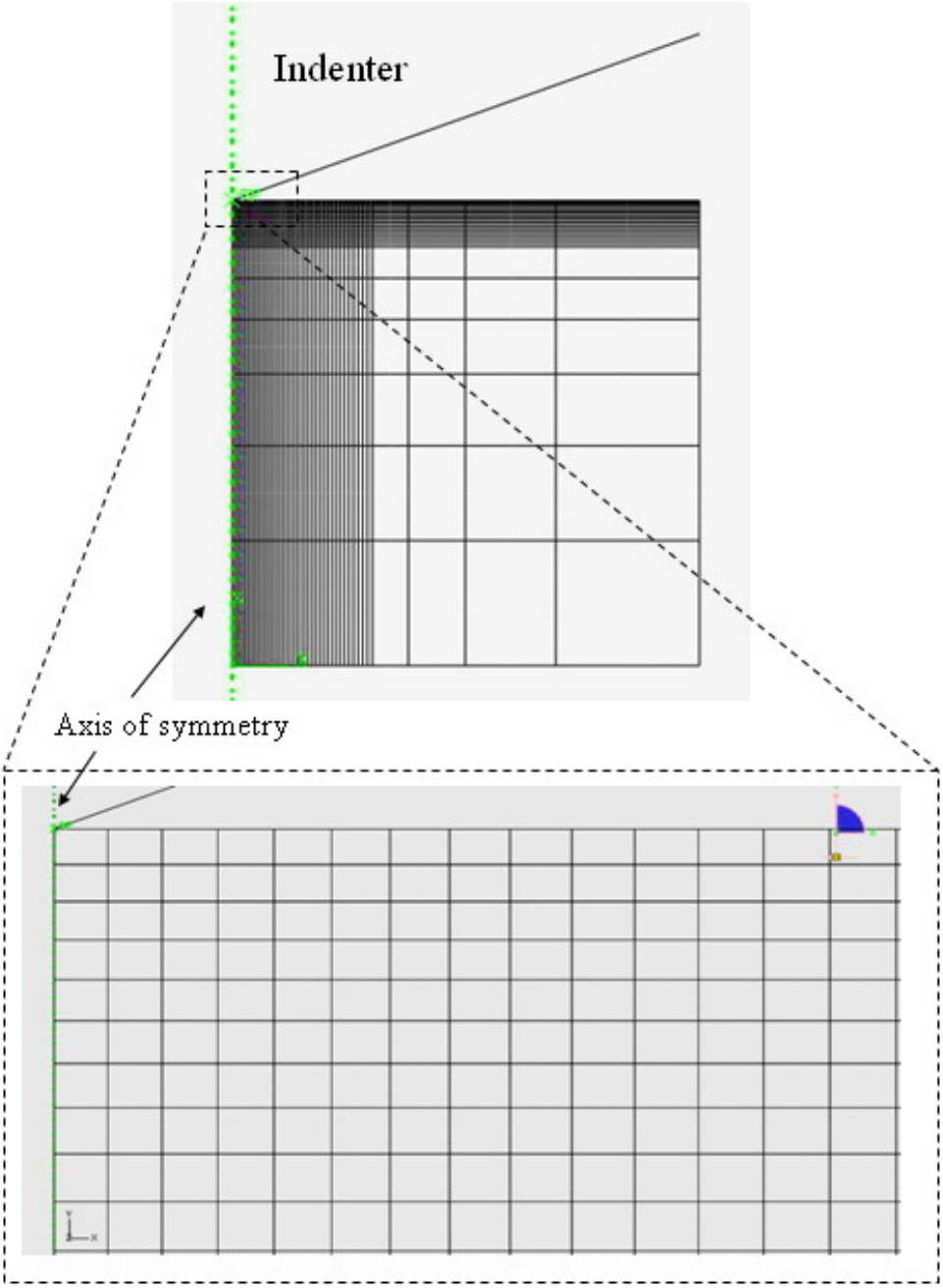

Fig. 80 Finite element meshing of the axisymmetric indentation problem.

4.2.3.1.1 Influence of yield stress

Simulations were undertaken for a variety of materials characterized by the following property definitions to show the influence of different yield stresses on the results of simulation. Three different ratios of σ_y/E were used for calculations: (1) σ_y/E=0.03 (2)

σ_y/E=0.0125 (3) σ_y/E=0.0025. Young's modulus is assumed to be 200 GPa and Poisson's ratio to be 0.28. The friction coefficient between the indenter and the sample was assumed to be 0.1. The Mises yield criterion was used.

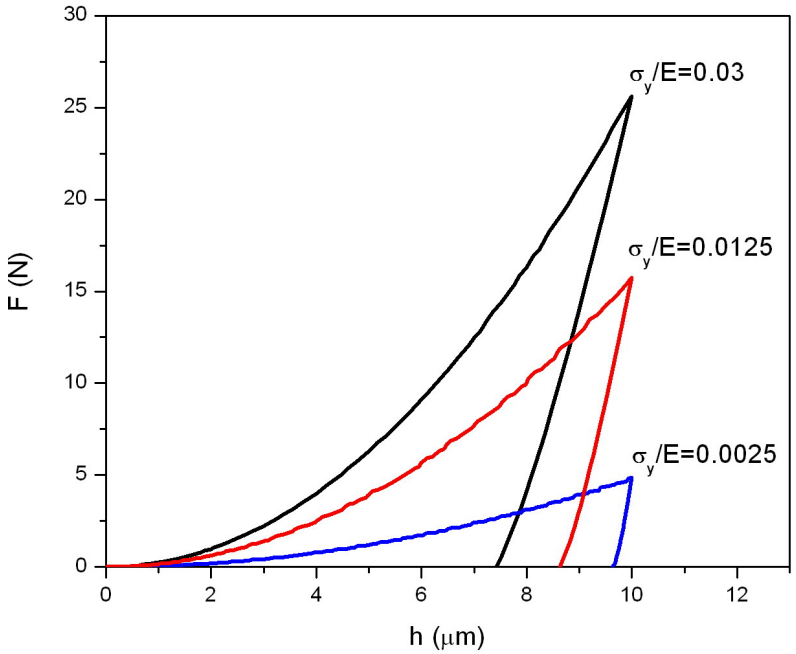

Fig. 81 Load-depth relationships for: σ_y/E=0.03, σ_y/E=0.0125 and σ_y/E=0.0025.

The yield stress is defined as the stress at which large strains take place without further increase in stress and the material begins to deform plastically. Before the yield point the material will deform elastically and when the applied stress is removed it can recover to its original shape. Once the yield point is surpassed, some fraction of the deformation will be permanent and non-reversible [4]. From Fig. 81, it can be seen that when the yield stress decreased from 6 GPa to 0.5 GPa, the highest reaction force achieved dropped down heavily, and the remaining depth increased.

The contour plots for von Mises stress for yield stress of 6, 2.5 and 0.5 GPa under full loading and unloading are shown in Fig. 82. It was mentioned by Johnson [24] that the pressure in the hydrostatic core beneath the indenter is a function of the single non-dimensional variable

$$\varepsilon^* = \frac{E^*}{\sigma_y \tan\alpha} \tag{75}$$

where α is the semi-angle of the conical indenter, and $\frac{1}{E^*} = \frac{1-\nu_1^2}{E_1} + \frac{1-\nu_2^2}{E_2}$, E_1, E_2 and ν_1, ν_2 are the Young's modulus and Poisson's ratio of the indented material and the indenter，respectively.

This dimensionless value may be interpreted as the ratio of the strain imposed by the indenter (1/tanα) to the elastic strain capacity of the material (σ_y/E^*). The indentation pressure under elastic, elastic-plastic and fully plastic conditions may be correlated on a non-dimensional graph of (p_m/σ_y) (definition of p_m see Chapter 3.1.6) as a function of $\varepsilon^* = \frac{E^*}{\sigma_y \tan\alpha}$. Fully plastic deformation occurs for a cone at a value of $\varepsilon^* = \frac{E^*}{\sigma_y \tan\alpha}$ about 30 [24], which means σ_y~2.5 GPa.

The above shows that the material with σ_y=6 GPa is in the elastic-plastic region; the one with σ_y=2.5 GPa is around the transition between the elastic-plastic and the fully plastic region, and the one with σ_y=0.5 GPa is in the fully plastic region. By decreasing the yield stress, the stress distribution becomes more emanative.

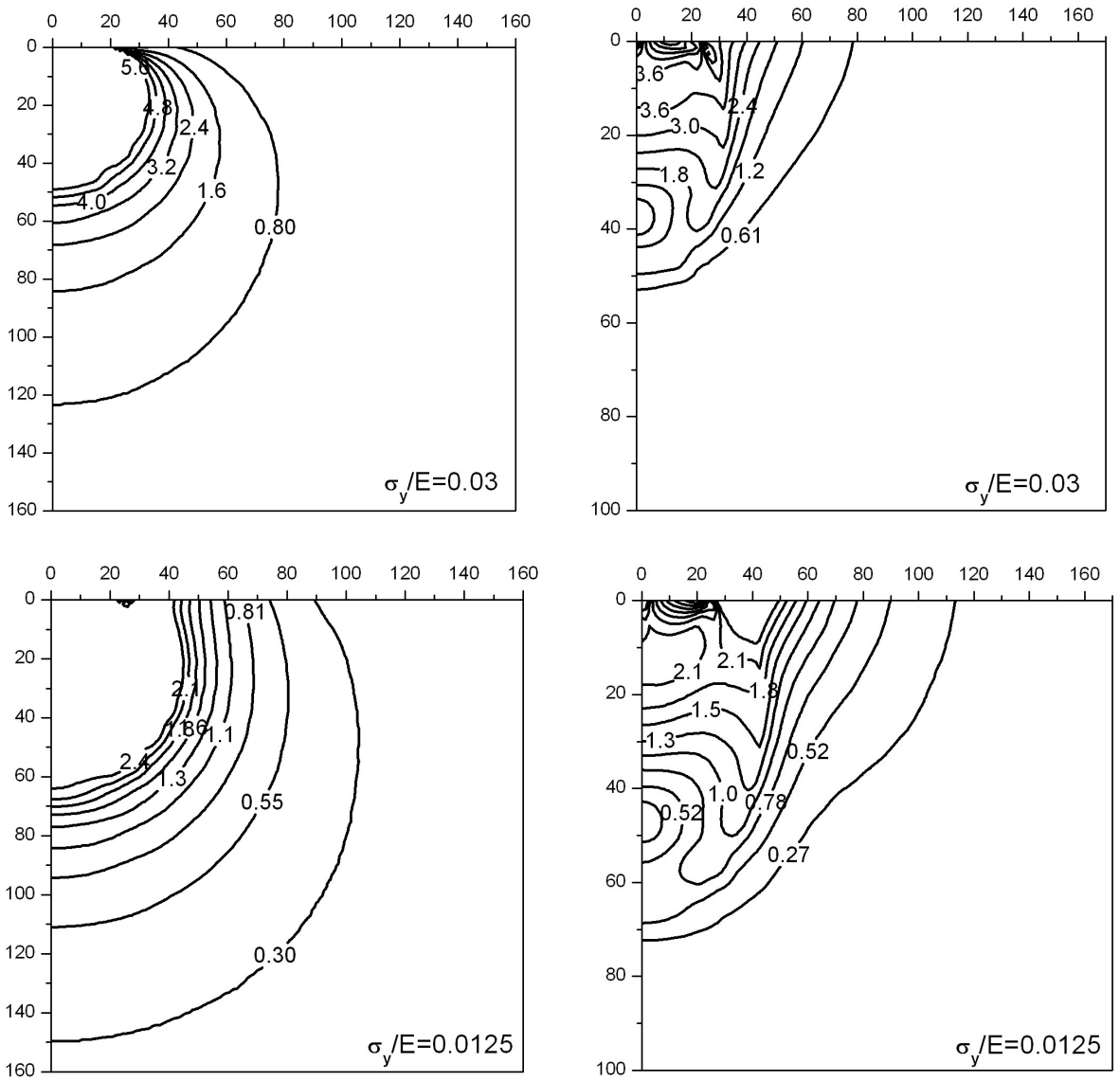

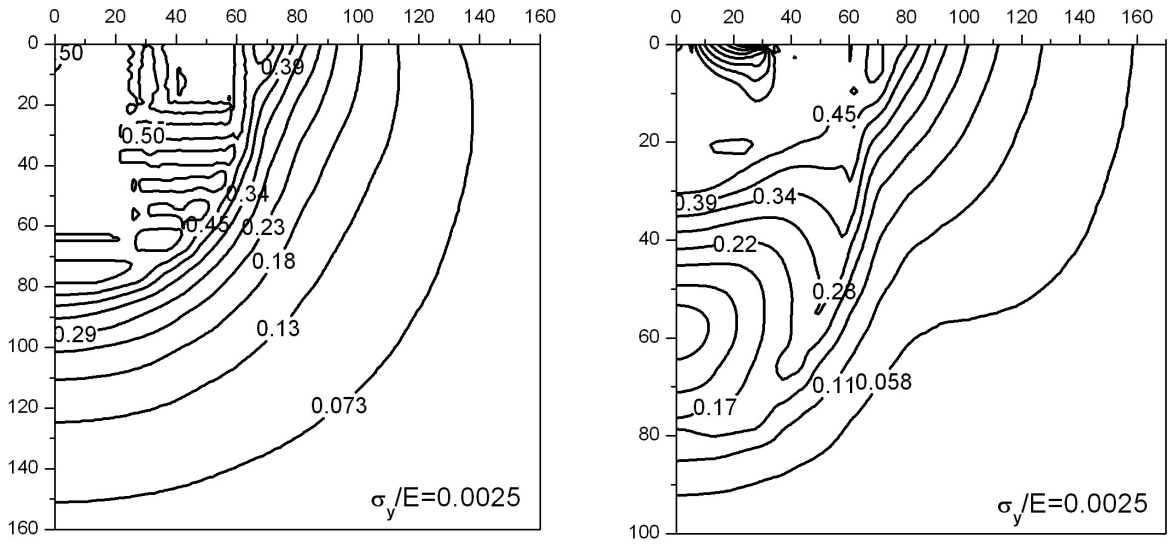

Fig. 82 Von Mises stress distributions for: σ_y/E=0.03, σ_y/E=0.0125 and σ_y/E=0.0025 under full loading (right) and unloading (left).

4.2.3.1.2 Influence of elastic modulus

Simulations were undertaken for a variety of materials characterized by the following property definitions to show the influence of different elastic moduli on the results of simulation. Three different ratios of σ_y/E were used for calculations: (1) σ_y/E=0.01 (2) σ_y/E=0.02 (3) σ_y/E=0.04. Yield stress was assumed to be 2 GPa and the Poisson's ratio to be 0.28. The friction coefficient between the indenter and the sample was assumed to be 0.1.

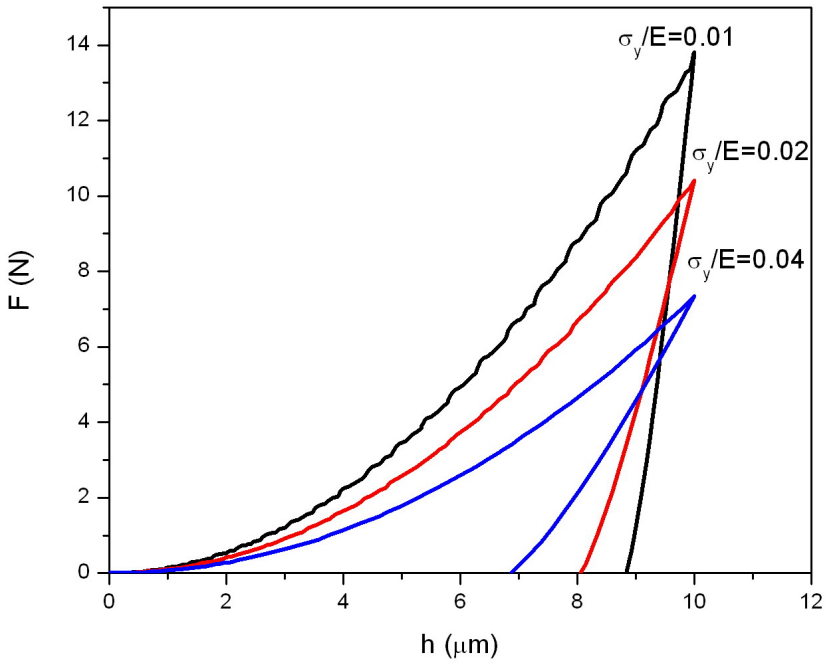

Fig. 83 Load-depth relationships for: σ_y/E=0.01, σ_y/E=0.02 and σ_y/E=0.04.

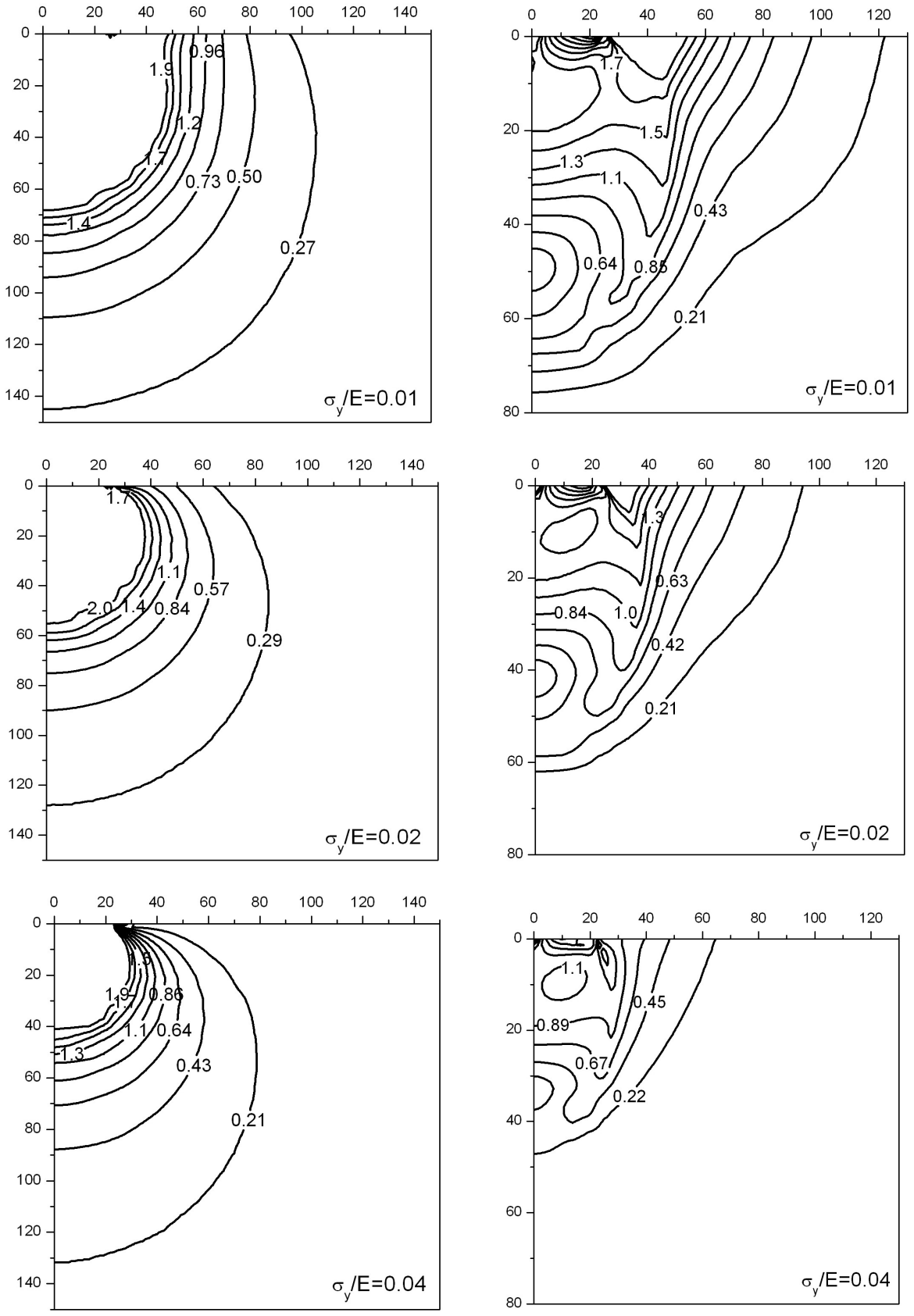

Fig. 84 Von Mises stress distributions for: σ_y/E=0.01, σ_y/E=0.02 and σ_y/E=0.04 under full loading (right) and unloading (left).

Fig. 83 is the plot for load and depth profile for σ_y/E=0.01, σ_y/E=0.02 and σ_y/E=0.04. The elastic modulus describes the tensile elasticity of the material, or the tendency to deform along an axis when opposing forces are applied along that axis. When the elastic modulus decreases from 200 GPa to 50 GPa, the maximum reaction at full loading decreases, as does the residual depth.

Von mises stress contour plots for different elastic moduli are shown in Fig. 84. The stress magnitudes at the same coordinate for both loading and unloading decrease with decreasing elastic modulus from 200 GPa to 50 GPa, and at the same time the distributions become more convergent.

4.2.3.1.3 Influence of Poisson's ratio on simulation

Simulations were undertaken for a variety of materials characterized with different Poisson's ratios to show the ratio's influence on the results of simulation. Yield stress was assumed to be 2 GPa and the elastic modulus to be 200 GPa. The Poisson's ratio of 0.4, 0.2 and 0.1 were used to calculate. The friction coefficient between the indenter and the sample was assumed as 0.1.

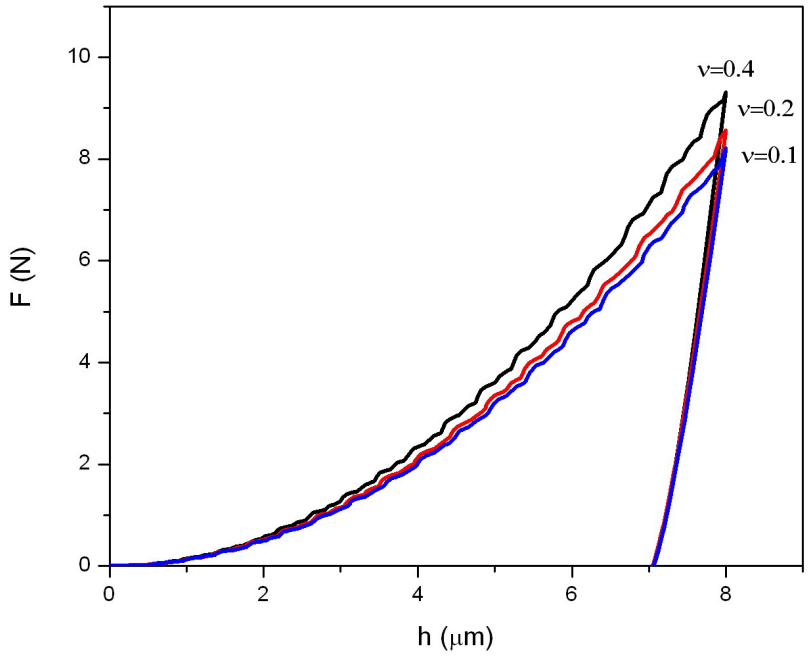

Fig. 85 Load-depth relationships for Poisson's ratio: 0.4, 0.2 and 0.1.

Poisson's ratio is defined as the absolute value of the ratio of lateral strain to the corresponding axial strain resulting from uniformly distributed axial stress [4]. Poisson's effect, observed from the molecular level, is caused by slight movements of molecules and the stretching of molecular bonds within the material lattice to accommodate the stress. When the bonds elongate in the stress

direction, the other directions will be shortened. The macroscopic phenomenon comes from such behaviour multiplied millions of times throughout the material lattice. The relationships for different Poisson's ratios are shown in Fig. 85.

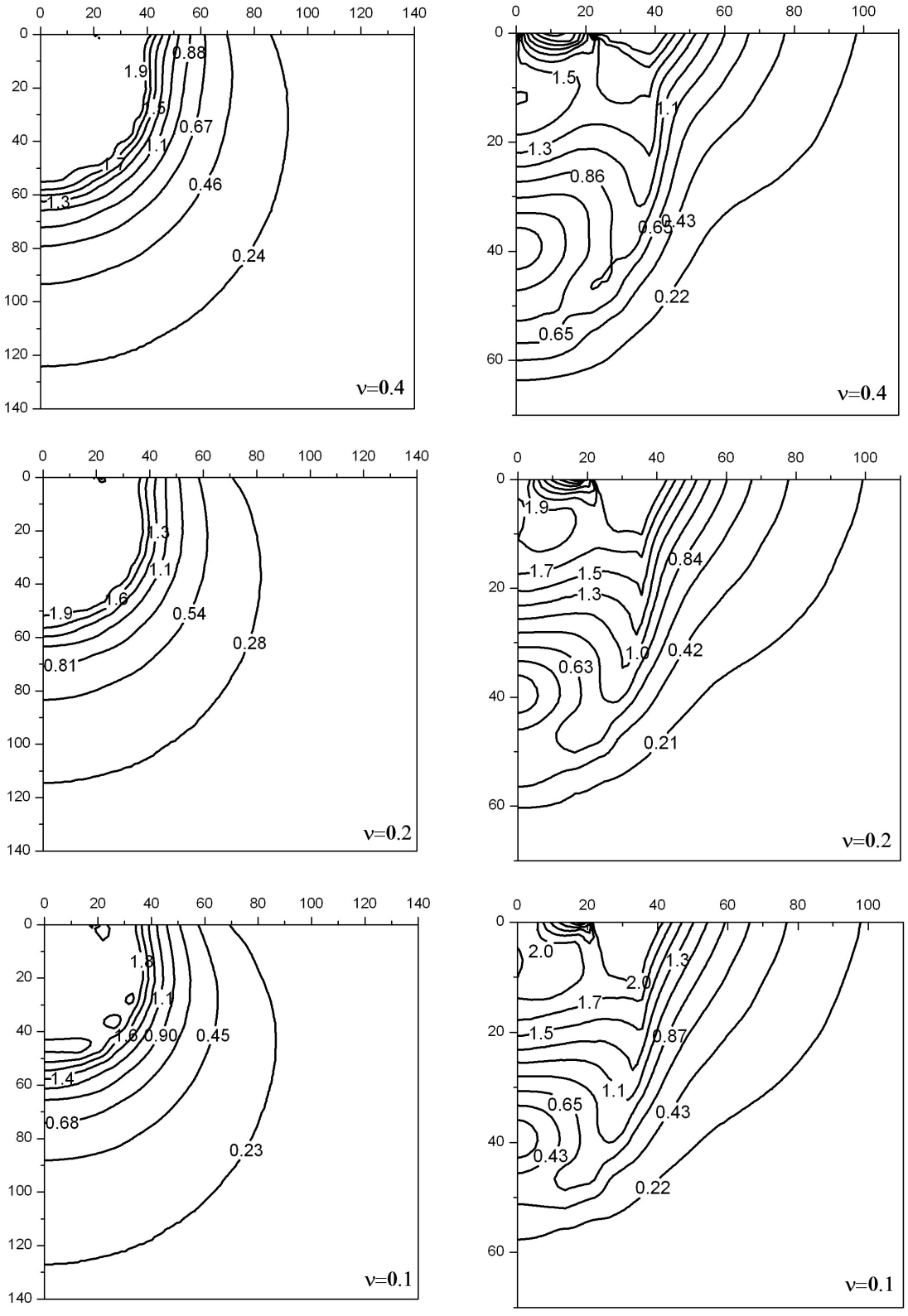

Fig. 86 Von Mises stress distributions for Poisson's ratio: 0.4, 0.2 and 0.1 under full loading (right) and unloading (left).

The loading behaviours at beginning have superposition area, so as for the latter half unloading curves. After the superposition area, the one with higher Poisson's ratio increases the force more quickly, and reaches the higher reaction force. The remained depths in the material are nearly the same.

Von Mises stress contour plots for different Poisson's ratios are shown in Fig. 86. It is clear that Poisson's ratio has no great influence on the stress magnitude. For both full loading and unloading, the stress fields do not change so much.

4.2.3.2 Modelling of 3Y-TZP material

True stress-strain curve is needed to define the plastic behaviour of the material, which was necessary for ABAQUS [130].

$$\varepsilon_{pl} = \varepsilon_{true} - \varepsilon_{el} = \varepsilon_{true} - \frac{\sigma_{true}}{E} \tag{76}$$

where ε_{pl} is true plastic strain, ε_{true} is true total strain, ε_{el} is true elastic stain, σ_{true} is true stress, and E is Young's modulus.

The plastic behaviour of Zirconia (Fig. 87) could be found from the indentation test data given by *E*. Sanchez-Gonzalez; yield stress σ_y was about 2 GPa [150]. Young's modulus *E* was 220 GPa, and Poisson's ratio *v* was 0.28 [81].

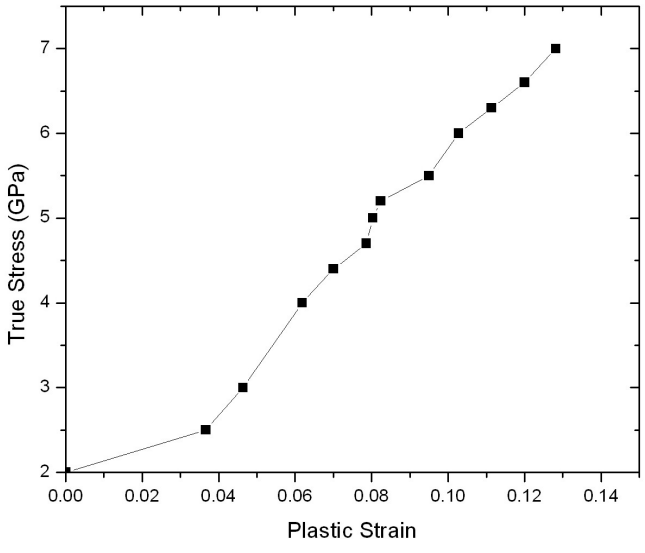

Fig. 87 Plastic behaviour of Y-TZP.

The simulations of three different loads were done: 100 N, 250 N and 500 N. The meshing belonging to the CAX8R (8-noded biquadratic axisymmetric quadrilateral) category comprised of 9221 nodes and 3000 elements for 100 N, of 10131 nodes and 3300 elements for 250 N, and of 19221 nodes and 6300 elements for 500 N. Other conditions were the same as described in Chapter 4.2.3.1. The curves for load-depth are shown in Fig. 88. The depths after recovering were 18.5 μm, 29.3 μm and 41.55 μm for 100 N, 250 N and 500 N, while from the indentation experiment they were 20 μm, 32 μm and 48 μm (Chapter 4.2.2.6).

The area bounded by the hysteresis load-displacement curve represents the energy lost in the plastic deformation and stored elastic energy as residual stresses. This energy can be written as [149]:

$$U = \int_0^{h_t} Ah^2 dh - \int_{h_r}^{h_t} A_e (h - h_r)^2 dh \tag{77}$$

where constant A factors in the elastic-plastic loading and constant A_e factors in the elastic unloading, depending on the indenter shape and the specimen material.

For a conical indenter with half angle α, these constants can be expressed by [149]:

$$A = E^* \left[\sqrt{\frac{E^*}{\pi \tan^2 \alpha H}} + \left[\frac{2(\pi - 2)}{\pi} \right] \sqrt{\frac{\pi H}{4E^*}} \right]^{-2} \tag{78}$$

$$A_e = \frac{2}{\pi} E^* \tan \alpha \tag{79}$$

where H is hardness and E^* is combined modulus (Chapter 4.2.3.1.1). Substituting the expressions for A and A_e into Eq. (77), there is:

$$U = \left(\frac{1}{3} \sqrt{\frac{1}{\pi \tan^2 \alpha}} \right) \frac{p^{3/2}}{\sqrt{H}} \tag{80}$$

From the integrations of the three load-displacement curves (Fig. 88) using Eq. 80, the Vickers hardness values can be calculated, and they are 1356 HV, 1330 HV and 1342 HV. Compared with the theoretical value 1200 HV (Chapter 4.1.5), the error may come from the simplification of a Vickers indenter into a conical indenter, and diamond indenter into a rigid indenter, which has influence on the value of E^* in 2D simulation.

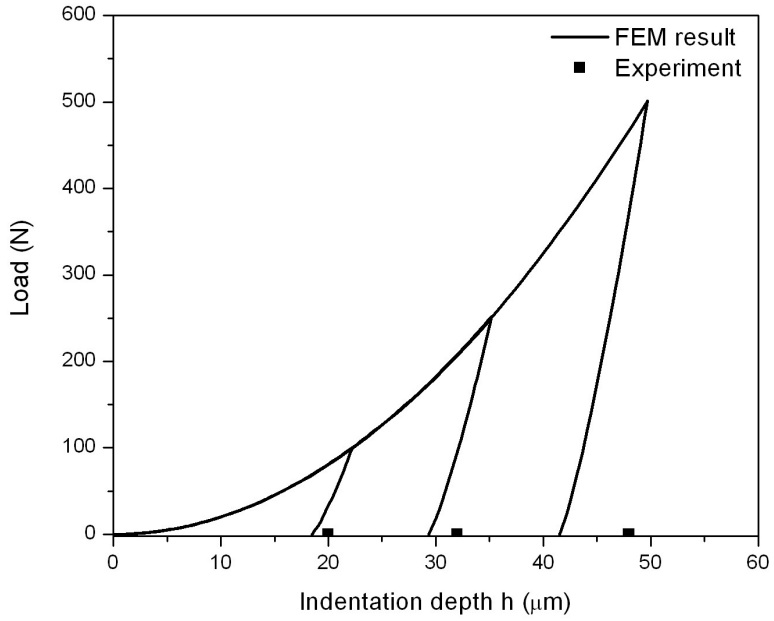

Fig. 88 Load-depth relationship of 3Y-TZP for 100 N, 250 N and 500 N (black points represent experiment data of residual depths).

The simulation results show that upon loading, the material directly beneath the indenter is placed in a state of compression, while the material surrounding the indentation impression is subjected to tensile stresses acting across the interacted surface. With increased indenter penetration depth, the maximum principal compressive stress region spreads deeper, and the tensile stress region on the interacted surface extends.

Upon unloading, the maximum principal compressive stress region directly beneath the indenter shrinks, while the surrounding tensile stress expands. At full unloading, the tensile stresses developed on the interacted surface reach the maximum values.

From the von Mises stress plots in Fig. 89 (e) at full loading stage, the plastic deformed region can reach as deep as 180 μm, and the region surrounding the plastic deformed region is called the elastic region.

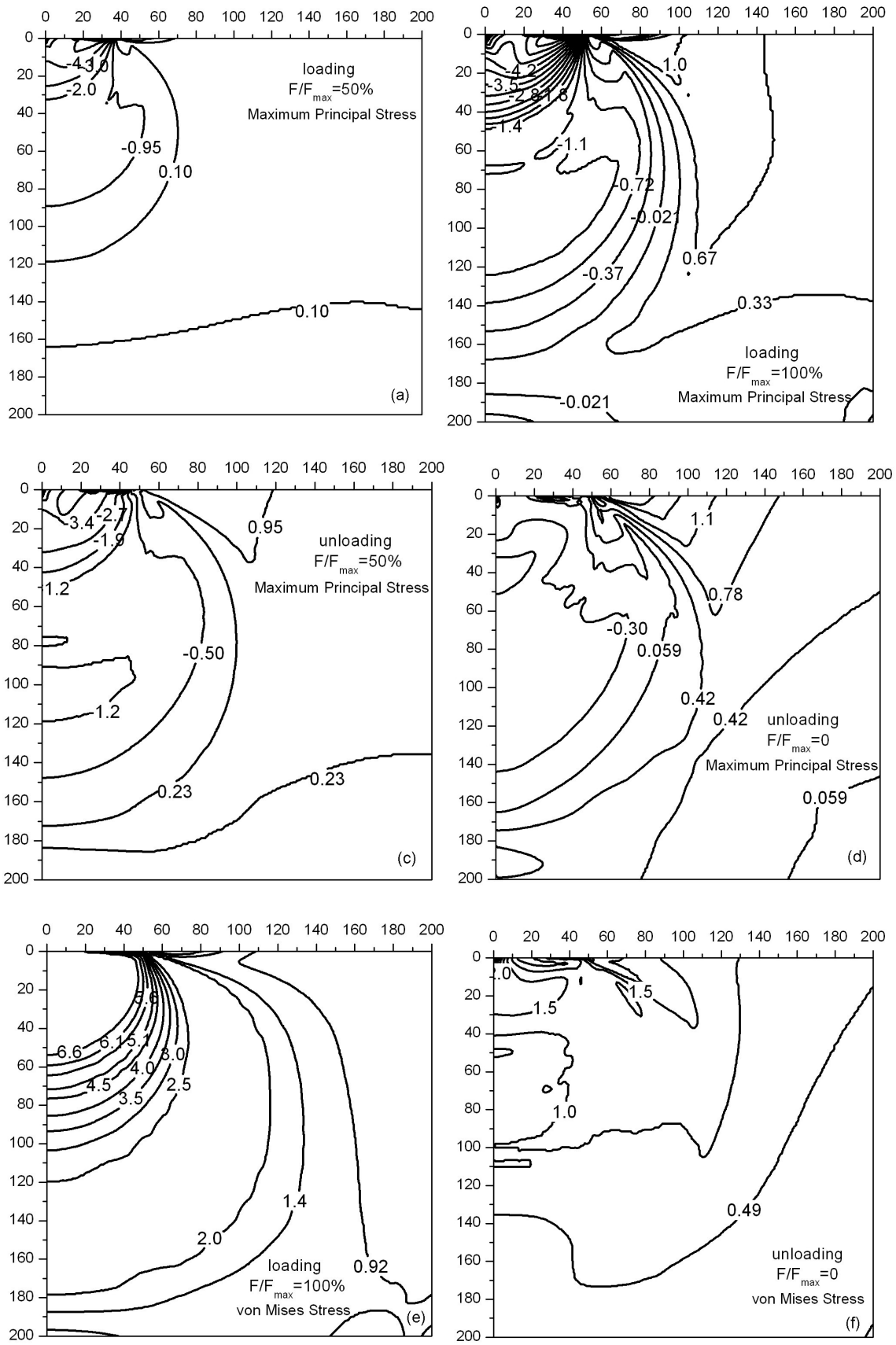

Fig. 89 Iso-stress contour plots (in GPa) of the maximum principal stress at different stages of a 100 N indentation process: (a) intermediate stage of loading (F/F_{max} = 50%); (b) full loading (F/F_{max} = 100%); (c) intermediate stage of unloading (F/F_{max} = 50%); (d) full unloading (F/F_{max} = 0%); (e) and (f) show the plots of von Mises stress (in GPa) at full loading and full unloading, respectively.

Fig. 90 and 91 are the results of the simulation for the indentation of zirconia with a load of 250 N and 500 N, in the form of plots of maximum principal stress and von Mises stress of the 2D model. Compared with the results of 100 N, at the same stage, the stress values accordingly increase, and the maximum principal compressive stress region spreads much deeper, as does the maximum principal tensile stress region. The plastic deformed region at full loading stage of 250 N and 500 N reach as deep as 240 μm and 375 μm, respectively.

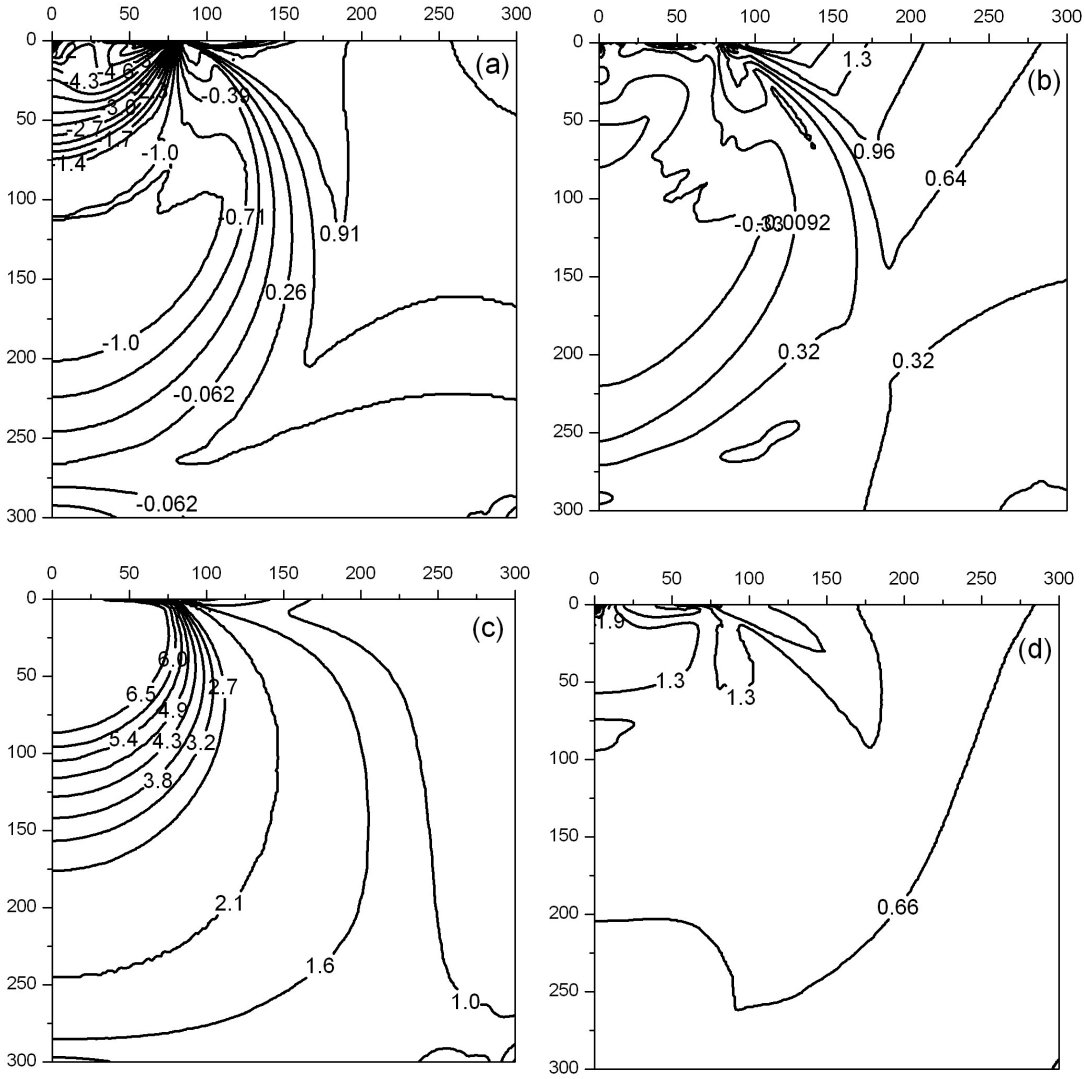

Fig. 90 Iso-stress contour plots (in GPa) of the maximum principal stress at different stages of a 250 N indentation process: (a) full loading (*h/hmax* =100%); (b) full unloading (*h/hmax* =0%). (c) and (d) show the plots of von Mises stress (in GPa) at full loading and full unloading, respectively.

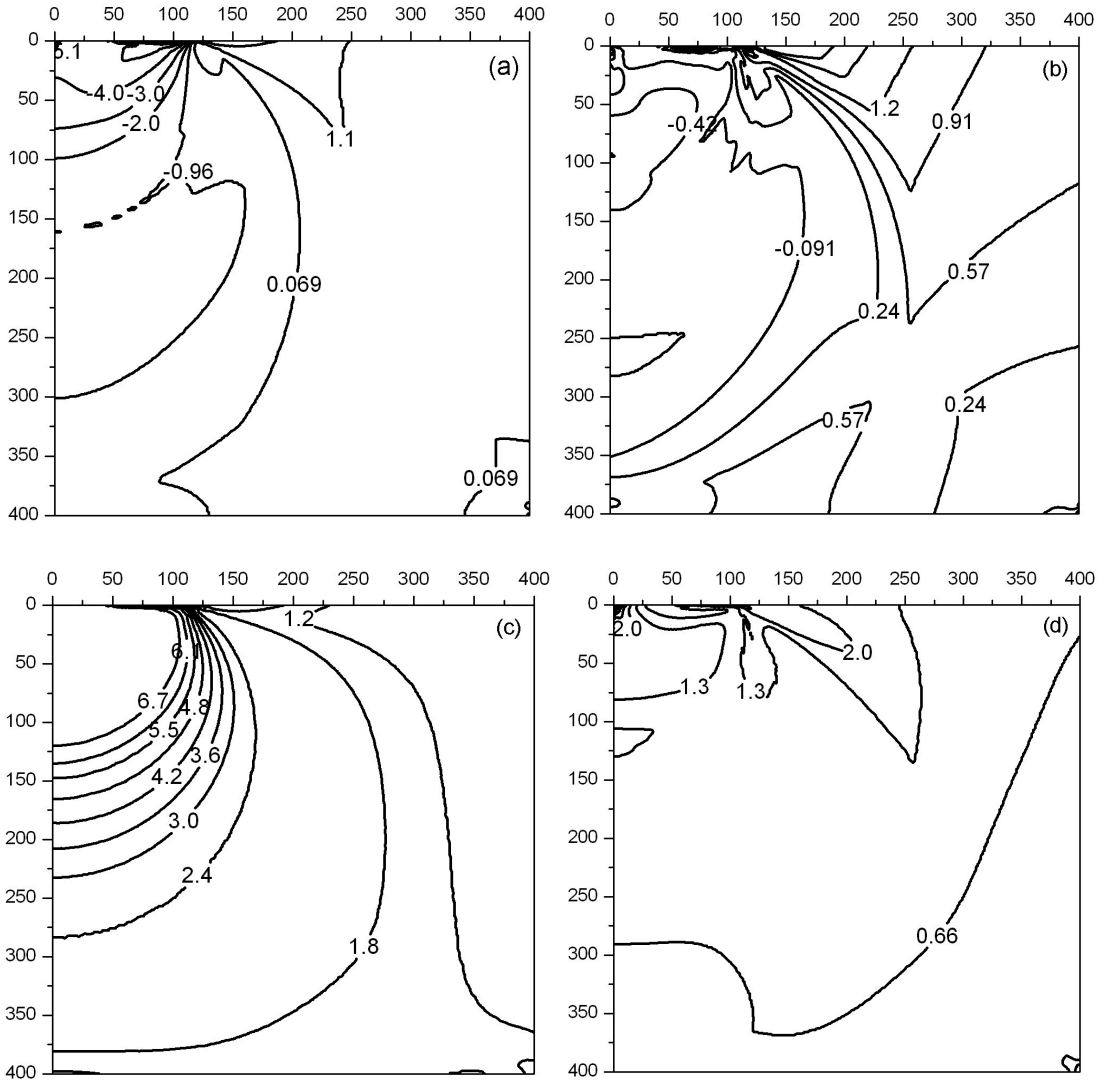

Fig. 91 Iso-stress contour plots (in GPa) of the maximum principal stress at different stages of a 500 N indentation process: (a) full loading (*h/hmax* =100%); (b) full unloading (*h/hmax* =0%). (c) and (d) show the plots of von Mises stress (in GPa) at full loading and full unloading, respectively.

Before the next step is continued, one important thing should be first announced: how to define the beginning of tetragonal to monoclinic transformation. Since the monoclinic phase content plays a very crucial role in this thesis, it will also be used to define when the transformation starts. One special point (130, 40) was selected, and the monoclinic phase friction at this point is about 10%. From the Raman spectrum at this point the bands at 181 cm^{-1} and 190 cm^{-1} are already very unapparent, and this friction can be regarded as the initial point (Fig. 92).

The cross-section mapping of m-phase around the indentations of 100 N from Fig. 70 is extracted, and compared with the stress contour of the maximum principal stress at full unloading stage from Fig. 89 (Fig. 93 (a)). Two arbitrary lines are chosen from these two plots. Line 1 is from point (0, 20) to point (0, 140), and line 2 is from point (0, 40) to point (40, 120). The highest monoclinic phase content does not locate directly under the tip of the indenter, but somewhere below the tip.

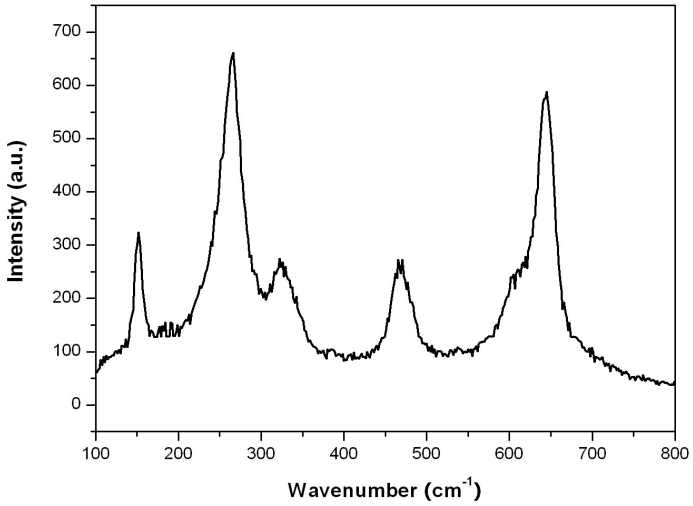

Fig. 92 Raman spectrum at point (130, 40).

This phenomenon can be explained by the maximum principal stress distribution. The highest maximum principal stress is also not at the tip, but some micrometer below it. From the plots of line 1 (Fig. 93 (b)), it can be observed that the tendencies of monoclinic phase and maximum principal stress from 0 to 30 micrometer are similar. When the monoclinic phase content approaches the starting value (≤ 10%), the corresponding stress value is about 0.35 GPa. From the plots of line 2 (Fig. 93 (c)), when the monoclinic phase content also approaches the starting value (≤ 10%), the corresponding stress value is about 0.31 GPa. This number is of the same order of magnitude as the one from the plot of line 1. In other words, at a stress level of 300 MPa, very little of the tetragonal phase starts to transform to monoclinic phase, and can be regarded as the critical stress for zirconia to have the transformation.

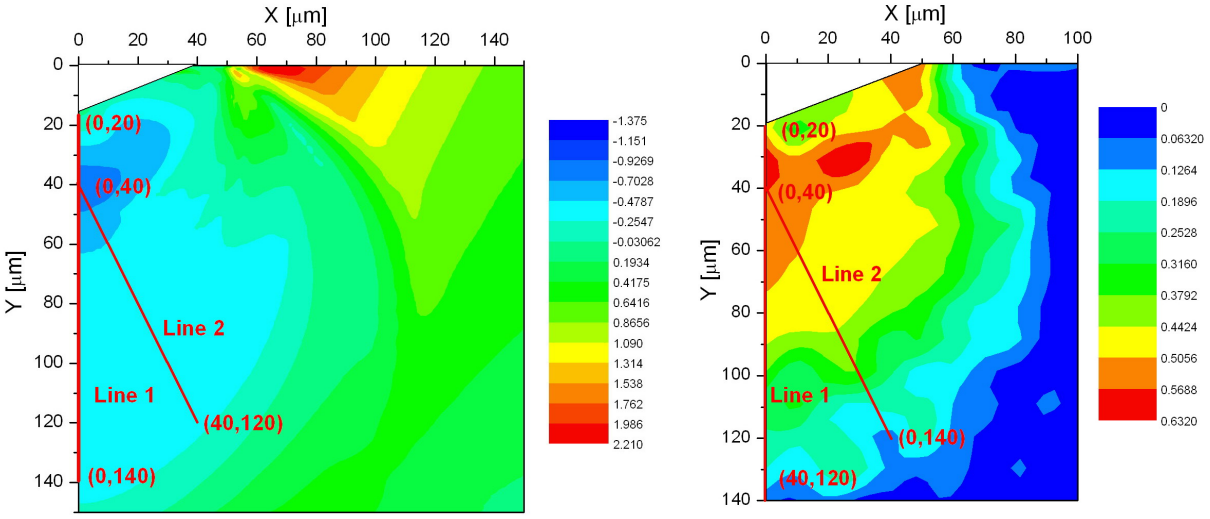

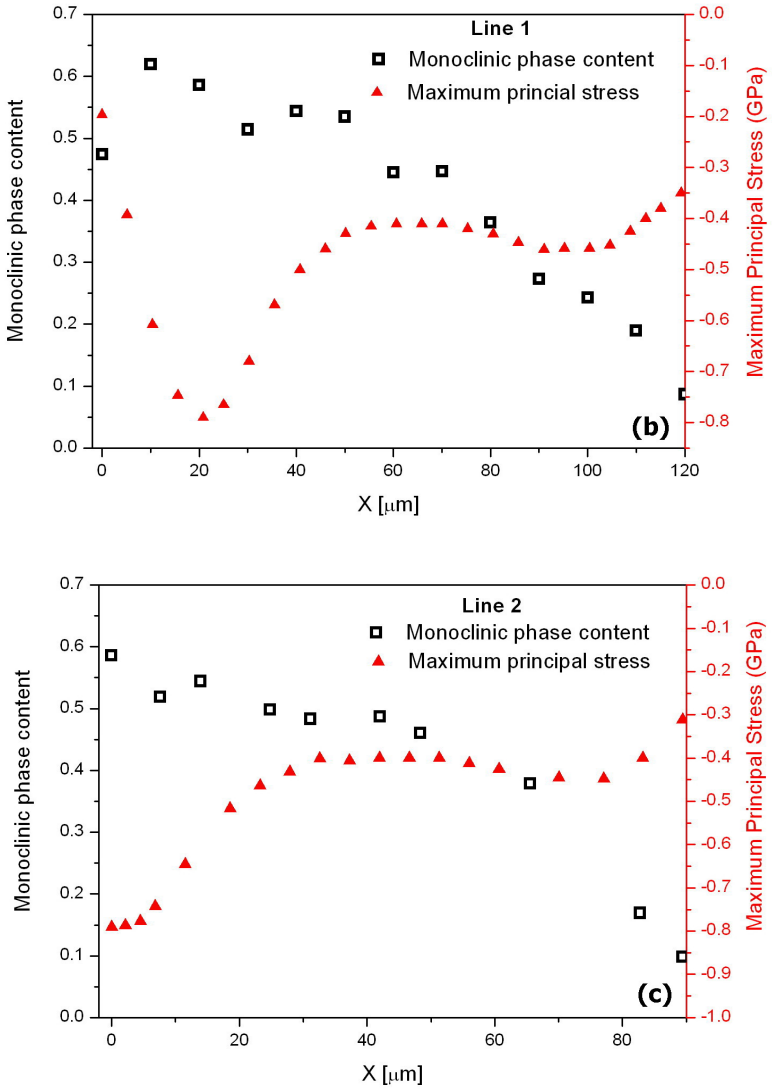

Fig. 93 (a) The cross-section mapping of m-phase around the indentations (from Fig. 70) and stress contour of the maximum principal stress at full loading stage (from Fig. 89) for 100N. (b) The plots of monoclinic phase content and maximum principal stress along line 1. (c) The plots of monoclinic phase content and maximum principal stress along line 2.

4.2.3.3 Three-dimensional FEM simulation of 3Y-TZP material

In 3D simulation, one-fourth of the indentation system was used due to the body symmetry, and the diamond indenter was assumed to be a discrete rigid indenter with opposite faces at an angle of 136°. A contact model was used for such simulations. Fine finite element meshing was used in the vicinity of the contact region underneath the indenter. A gradually coarser meshing was used away from the contact region to reduce the computational time and ensure a high degree of accuracy. The indenter comprised of 91 R3D4 (4-nided 3D bilinear rigid quadrilateral) meshing elements and the deformable part comprised 48159 nodes and 10963 elements belonging to the C3D20 (20-noded quadratic brick) category. During the analysis, loading was achieved by

displacing the rigid indenter downward along the Y axis (Fig. 94). To unload, the indenter was displaced upwards back to the original position. The boundary conditions are defined as: (1) the bottom edge: U1=U2=U3=UR1=UR2=UR3=0; (2) the symmetric face on XY: U3=UR1=UR2=0; (3) the symmetric face on YZ: U1=UR2=UR3=0. Other conditions were the same as that used for the 2D model. The loading and unloading curves can be obtained directly from the ABAQUS output of the reaction force in the normal direction on the rigid indenter as a function of the indenter vertical displacement.

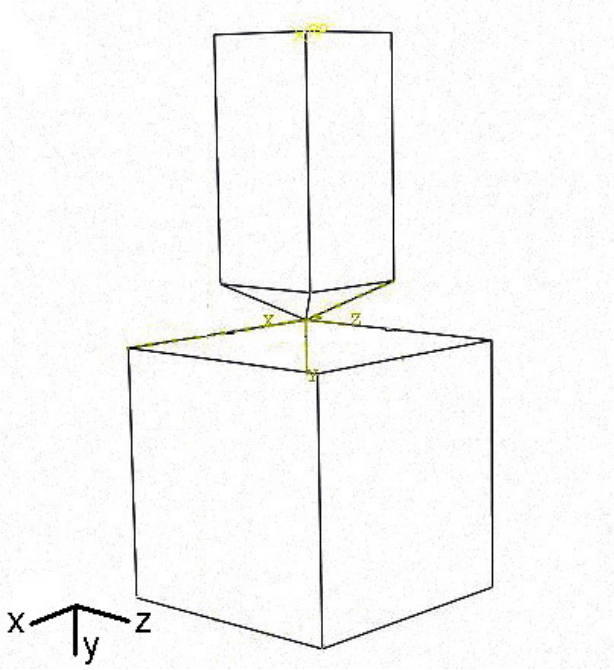

Fig. 94 Geometry of 3D indentation problem (not to scale)

Fig. 95 and Fig. 96 present the results of the simulation for the indentation of zirconia with loads of 100 N and 250 N, in the form of plots of maximum principal stress on the *XZ* surface of the 3D model. The various stages of loading and unloading are characterised by the ratio of the indentation depth to the maximum depth at full loading. Therefore, h/h_{max} =100% represents the stage of full loading, h/h_{max} =0% indicates that the stage has reached full unloading, and h/h_{max} =50% and 86% is the intermediate stage.

Upon loading, the material directly beneath the indenter is placed in a state of compression while the material surrounding the indentation impression is subjected to tensile stresses. With increased indenter penetration depth, the maximum principal compressive stress region expands in the surface, as does the surrounding tensile stress region.

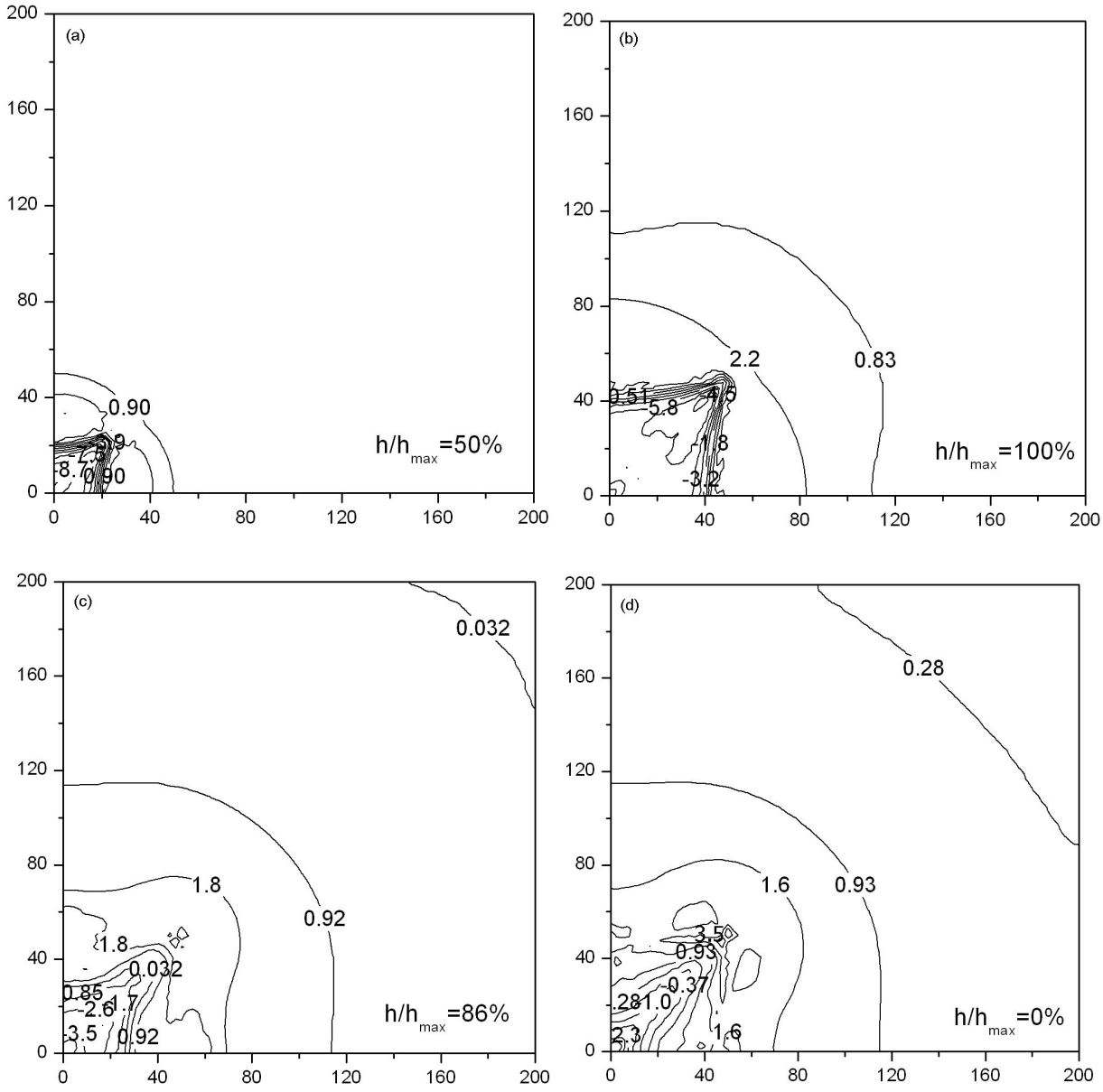

Fig. 95 Iso-stress contour plots (in GPa) of the maximum principal stress on XZ surface at different stages of a 100 N indentation process of 3D model: (a) intermediate stage of loading (h/hmax = 50%); (b) full loading (h/hmax = 100%); (c) intermediate stage of unloading (h/hmax = 86%); (d) full unloading (h/hmax = 0%).

Upon unloading, the maximum principal compressive stress region directly beneath the indenter shrinks, while the surrounding tensile stress expands. The highest stress values concentrate close to the apex of the indentation impression, which leads to the highest monoclinic content during the phase transformation shown in Fig. 70 and Fig. 71 (Chapter 4.2.2.6.2).

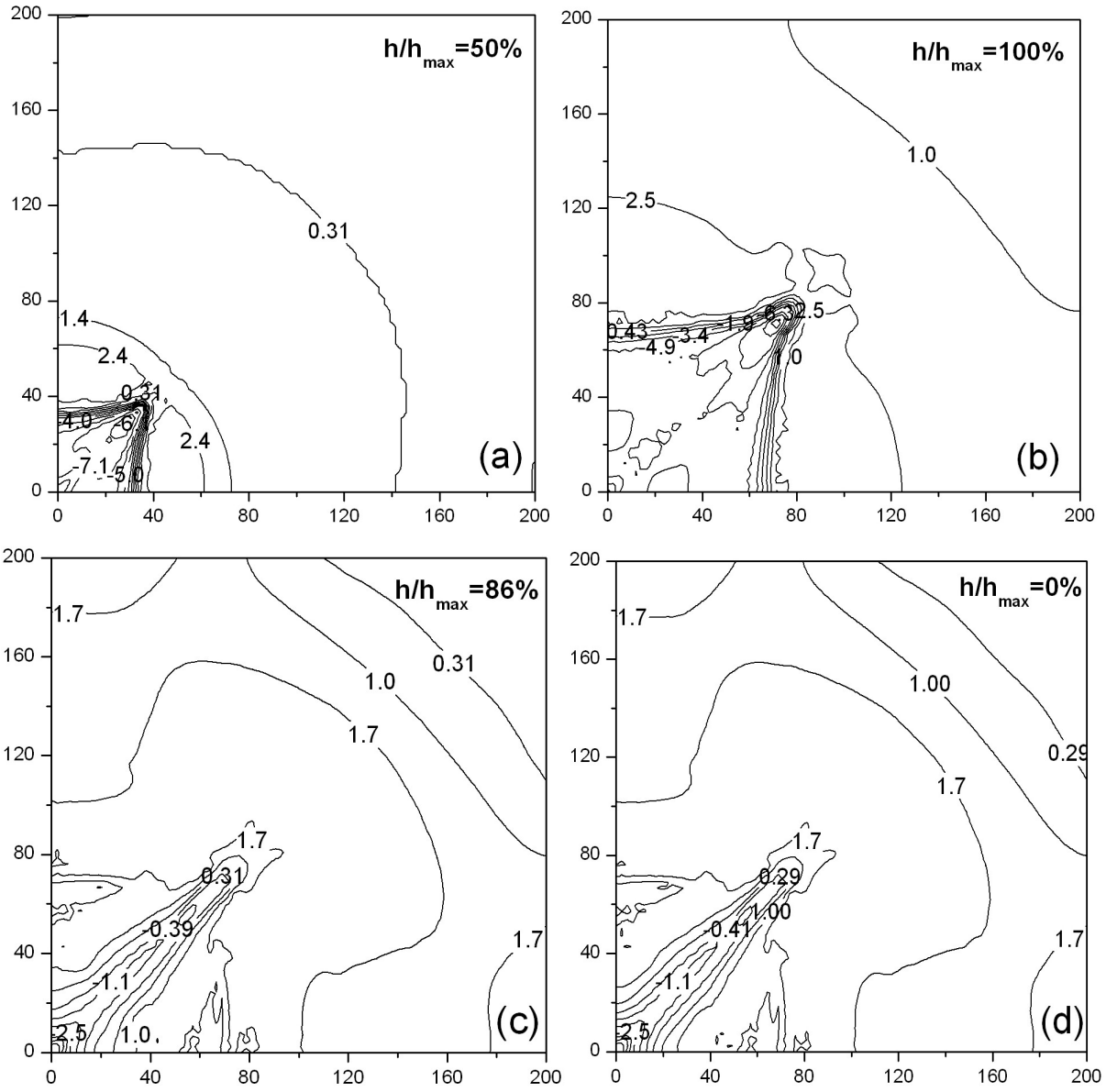

Fig. 96 Iso-stress contour plots (in GPa) of the maximum principal stress on XZ surface at different stages of a 250 N indentation process of 3D model: (a) intermediate stage of loading (h/hmax = 50%); (b) full loading (h/hmax = 100%); (c) intermediate stage of unloading (*h/hmax* = 86%); (d) full unloading (*h/hmax* = 0%).

The line starting from the middle of the vertical indentation edge is specially chosen for examination, and is y=0 in Fig. 70 and Fig 71, and y=0 and z=0 in the 3D model in Fig. 94. Fig. 97 shows the plots of monoclinic phase content (Cm) and maximum principal stress at the stage of full unloading along the distance from the indentation edge of 100 N. When monoclinic phase content is about 10% (60 μm from the indentation edge), the stress is about 1.1 GPa (Fig. 97) and the monoclinic phase has started to occur. This value is greater than the one achieved from 2D simulation because on the surface of the actual sample, cracks were produced that relaxed the stresses, whereas the fracture and crack are not considered here. However, in 2D simulation, the deduction was obtained from the lateral face of the sample, where no crack was created.

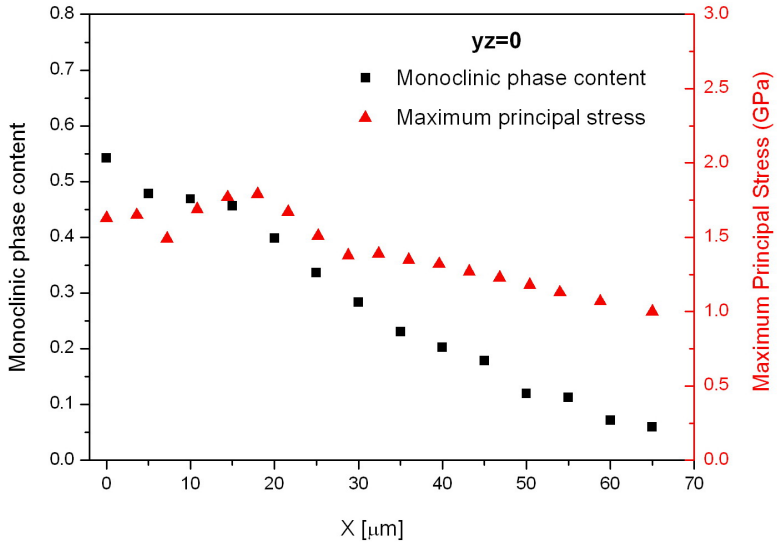

Fig. 97 Plots of monoclinic phase content (Cm) and maximum principal stress at the stage of full loading along the distance from the indentation edge of 100 N.

5 Conclusion

Phase transformation, stress-induced transformation toughening, and residual stress of stabilized zirconia ceramics under local mechanical pressure are worth elaboration and quantification, as these are the bases for the use of ceramics in engineering applications such as biomedical implants or industrial components.

The martensitic transformation of tetragonal zirconia is stress-assisted because the local stress state can interact with the unit cell transformation strain to ease the nucleation of the martensite phase, which leads to transformation toughening 3Y-TZP, and determines most of the practical application of this material. The stress can be external, such as applied stresses during mechanical testing. Characterisation of the transformation from tetragonal to monoclinic phase of 3Y-TZP, using non-destructive Raman scattering method, is helpful to understand this mechanism.

The Raman spectra of 3Y-TZP following indentation experiments are the mixtures of monoclinic and tetragonal phases. Still unknown are: how the background of the spectra should be subtracted, and how much the low intensity of many monoclinic bands influences the spectra by a slight increment of the background. There are indications that the background in such spectra is affected by a certain small fraction of cubic zirconia phase in stabilized 3Y-TZP. However, the manually subtracting cubic substrate in line or area measurements is considerably time-consuming and results in an increased uncertainty in the quantification, then leading to the unreality in real treatments. Thus a suitable algorithm must be found to determine the band intensities.

The relative position of the focus point of the Raman beam and the detected surface affects the change of band intensities in automatic line or area measurements when the surface is rough or fractured. When the beam focuses below the surface, the illuminated sample volume is greater, and more information can be collected. The band intensities of transparent, opaque and translucent materials show different behaviours according to the defocus distance, due to their different transmittance. Through such measurements, it is clear that the control of the roughness of the surface in automatic line or area measurements is significant.

To calculate the proportion of monoclinic phase, the software LabSpec was used to determine the band intensities. There are three different ways to calculate the band intensities; however in this analysis, the smooth fitting from the actual band intensities using Gauss-/Lorentz- curves was adopted.

Due to the influence of polarisation of band 265 cm^{-1} on intensity, the rotation-independent tetragonal band at 648 cm^{-1} was used in the equation of monoclinic fraction. Mapping of monoclinic phase fraction for indentation under different forces was obtained through manually-focused measurements. For planar plotting, the highest monoclinic phase fraction concentrates

around the corners of the indentations, due to the highest stress values. There is also indication that monoclinic phase exists along the 45° cracks from the indentation tips.

The fracture toughness, which is dependent on the transformability of tetragonal phase, was calculated from the fraction of transformed tetragonal phase and width of the transformation zone. This value conforms to the average value of fracture toughness according to Shetty et al., and is in good agreement with the theoretical value.

In order to acquire a cross section of the sample, a series of Vickers indentations were made on the sample surface and then the sample was broken along the line. Due to the extremely rough face, the Raman measurements were done by focusing on each point manually. The monoclinic zone beneath the indenter had a spherical contour, and the maximum depth for monoclinic phase to reach increased with the increasing load.

According to the symmetry, both finite element simulations - half of the indentation system of 2D, and one-fourth of that of 3D - were done using the commercial software ABAQUS/standard Versions 6.5 and 6.7. The same loads used in Raman measurements were also used in simulation. A rigid conical indenter with a 70.3° semi-angle was assumed to be the diamond indenter in 2D simulation, which had the same area function as a perfect Vickers four-sided pyramidal indenter.

The area bounded by the hysteresis load-displacement curve represents the energy lost in the plastic deformation and the elastic energy stored as residual stresses. The Vickers hardness calculated from load-displacement curve proved the accuracy of the model in simulation. The error may come from the simplification of the diamond indenter into a rigid indenter, which has influence on the simulation. However, this error is still in the acceptable range, so the use of such simulations is reasonable.

The deformation of materials under complex loading conditions, as well as the creep rupture associated with large deformations and a ductile failure mechanism at high stresses, are both normally controlled by von Mises criterion. However, maximum principal stresses are especially considered because the rupture in long-term situation is controlled either by maximum principal stress (MPS) or a combined MPS-von Mises criterion. Especially for brittle materials, the rupture tends to be more MPS-controlled.

The influence of yield stress, the elastic modulus and Poisson’s ratio on simulation was discussed separately for general materials. Regarding different yield stresses, when the yield stress decreased, the highest reaction force achieved dropped down heavily, and the remaining depth increased. With decreasing yield stress, the von Mises stress distribution became more emanative. In the case of varied elastic moduli, when elastic modulus decreased, the maximum reaction at full loading also decreased, as did the residual depth. The von Mises stress magnitudes at the same coordinate for both loading and unloading decreased with decreasing elastic modulus, and at the

same time the distributions became more convergent. According to various Poisson's ratios, the loading behaviour at the beginning had superposition area, as did the latter half of unloading curves. Following the superposition area, the area with a higher Poisson's ratio increased the force more quickly, and reached the higher reaction force. The remaining depths in the material were nearly equal. Poisson's ratio had no great influence on the stress magnitude. For both full loading and unloading, the stress fields did not show great change.

The 3Y-TZP material was simulated subsequently. The material directly beneath the indenter was in a state of compression, while the material surrounding the indentation impression was subjected to tensile stresses acting across to the interacted surface upon loading. With increased indenter penetration depth, the maximum principal compressive stress region spread deeper, and the tensile stress region on the interacted surface extended. Upon unloading, the maximum principal compressive stress region directly beneath the indenter shrank, while the surrounding tensile stress expanded. At full unloading, the tensile stresses developed on the interacted surface reached the maximum values.

From the association of the cross-section mapping of m-phase around the indentations with the stress contour of the maximum principal stress at full loading stage, it was apparent that when the monoclinic phase approached zero, the maximum principal stress was of the order of magnitude of 300 MPa. In other words, at stress level of 300 MPa, very little of tetragonal phase started to transform to monoclinic phase, and this value closely resembled the rupture strength of zirconia.

In a 3D simulation, the stress distribution of the sample surface was examined. The highest stress values concentrated close to the apex of the indentation impression, which lead to the highest monoclinic content during the phase transformation.
From the results of the line starting from the middle of the vertical indentation edge, when monoclinic phase content nearly faded away, the stress was about 1.1 GPa for 100 N. This value was higher than the one achieved from 2D simulation, and proved that the cracks relaxed the stresses on the surface of the sample.

6 References

1. Fischer-Cripps, A.C., *Introduction to Contact Mechanics*. Mechanical Engineering Series, ed. F.F. Ling. 2000, Austin: Springer.
2. G.R.Sawyer, P.M.S., T.F.Page, *Microhardness anisotropy of silicon carbide.* Journal of Materials Science, 1980. **15**: p. 1001-1013.
3. S.Fujita, K.M., S.Hyodo, *Anisotropy of high-temperature hardness in 6H silicon carbide.* Journal of Materials Scicece Letters, 1986. **5**: p. 450-452.
4. Kuhn, H. and D. Medlin, *ASM Handbook*. Mechanical Testing and Evaluation, ed. S.R. Lampman. Vol. 8. 2000.
5. Krell, A. and P. Blank, *Grain size dependence of hardness in dense submicrometer alumina.* Journal of the American Ceramic Society, 1995. **78**(4): p. 1118-20.
6. P.M.Sargent, *Indentation size effect and strain-hardening.* Journal of Materials science letters, 1989(8): p. 1139-1140.
7. Elmustafa, A.A., et al., *Indentation size effect. Large grained aluminum versus nanocrystalline aluminum-zirconium alloys.* Scripta Materialia, 2000. **43**(10): p. 951-955.
8. Li, H. and R.C. Bradt, *The microhardness indentation load/size effect in rutile and cassiterite single crystals.* Journal of Materials Science, 1993. **28**(4): p. 917-26.
9. Iost, A. and R. Bigot, *Indentation size effect: reality or artifact?* Journal of Materials Science, 1996. **31**(13): p. 3573-3577.
10. Li, H., et al., *The frictional component of the indentation size effect in low load microhardness testing.* Journal of Materials Research, 1993. **8**(5): p. 1028-32.
11. Ma, Q. and D.R. Clarke, *Size dependent hardness of silver single crystals.* Journal of Materials Research, 1995. **10**(4): p. 853-63.
12. Cook, R.F. and G.M. Pharr, *Direct observation and analysis of indentation cracking in glasses and ceramics.* Journal of the American Ceramic Society, 1990. **73**(4): p. 787-817.
13. Anstis, G.R., et al., *A critical evaluation of indentation techniques for measuring fracture toughness: I. Direct crack measurements.* Journal of the American Ceramic Society, 1981. **64**(9): p. 533-8.
14. Lawn, B.R., A.G. Evans, and D.B. Marshall, *Elastic/plastic indentation damage in ceramics: the median/radial crack system.* Journal of the American Ceramic Society, 1980. **63**(9-10): p. 574-81.
15. Evans, A.G. and E.A. Charles, *Fracture toughness determinations by indentation.* Journal of the American Ceramic Society, 1976. **59**(7-8): p. 371-2.
16. Niihara, K., R. Morena, and D.P.H. Hasselman, *Evaluation of KIc of brittle solids by the indentation method with low crack-to-indent ratios.* Journal of Materials Science Letters, 1982. **1**(1): p. 13-16.
17. Niihara, K., R. Morena, and D.P.H. Hasselman, *Further reply to "Comment on 'Elastic/plastic indentation damage in ceramics: the median/radial crack system'".* Journal of the American Ceramic Society, 1982. **65**(7): p. C116.
18. Shetty, D.K., et al., *Indentation fracture of tungsten carbide-cobalt cermets.* Journal of Materials Science, 1985. **20**(5): p. 1873-82.
19. Lankford, J., *Indentation microfracture in the Palmqvist crack regime: implications for fracture toughness evaluation by the indentation method.* Journal of Materials Science Letters, 1982. **1**(11): p. 493-5.
20. Laugier, M.T., *New formula for indentation toughness in ceramics.* Journal of Materials Science Letters, 1987. **6**(3): p. 355-6.
21. Laugier, M.T., *Palmqvist indentation toughness in tungsten carbide-cobalt composites.* Journal of Materials Science Letters, 1987. **6**(8): p. 897-900.

22. Laugier, M.T., *Palmqvist toughness in tungsten carbide-cobalt composites viewed as a ductile/brittle transition.* Journal of Materials Science Letters, 1987. **6**(7): p. 768-70.
23. Dukino, R.D. and M.V. Swain, *Comparative measurement of indentation fracture toughness with Berkovich and Vickers indenters.* Journal of the American Ceramic Society, 1992. **75**(12): p. 3299-304.
24. K.L.Johnson, *Contact Mechanics*. 1985, Cambridge: Cambridge University Press.
25. Yashima, M., et al., *Structural changes of ZrO2-CeO2 solid solutions around the monoclinic-tetragonal phase boundary.* Physical Review B: Condensed Matter, 1995. **51**(13): p. 8018-25.
26. Zhao, X. and D. Vanderbilt, *Phonons and lattice dielectric properties of zirconia.* Los Alamos National Laboratory, Preprint Archive, Condensed Matter, 2001: p. 1-10, arXiv:cond-mat/0108491.
27. Hannink, R.H.J., P.M. Kelly, and B.C. Muddle, *Transformation toughening in zirconia-containing ceramics.* Journal of the American Ceramic Society, 2000. **83**(3): p. 461-487.
28. P.Haasen, *Phase Transformations im materials*. Materials Science and technology, ed. R.W.Cahn, P.Haasen, and E.J.Kramer. Vol. 5. 1991, Weinheim: WCH.
29. Y.Gogotsi and S. Domnich, *High Pressure Surface Science and Engineering*. Materials science and engineering. 2003, Bristol: Institute of Physics Publishing.
30. Zhao, X. and D. Vanderbilt, *Phonons and lattice dielectric properties of zirconia.* Physical Review B: Condensed Matter and Materials Physics, 2002. **65**(7): p. 075105/1-075105/10.
31. Ingel, R.P. and D. Lewis, III, *Lattice parameters and density for yttria-stabilized zirconia.* Journal of the American Ceramic Society, 1986. **69**(4): p. 325-32.
32. Foster, A.S., et al., *Structure and electrical levels of point defects in monoclinic zirconia.* Physical Review B: Condensed Matter and Materials Physics, 2001. **64**(22): p. 224108/1-224108/10.
33. Liu, D.W., et al., *Neutron-scattering studies of phonons in disordered cubic zirconia at elevated temperatures.* Physical Review B: Condensed Matter and Materials Physics, 1987. **36**(17): p. 9212-18.
34. Mackrodt, W.C. and P.M. Woodrow, *Theoretical estimates of point defect energies in cubic zirconia.* Journal of the American Ceramic Society, 1986. **69**(3): p. 277-80.
35. Heuer, A.H., M. Ruhle, and D.B. Marshall, *On the thermoelastic martensitic transformation in tetragonal zirconia.* Journal of the American Ceramic Society, 1990. **73**(4): p. 1084-93.
36. Deville, S., J. Chevalier, and H. El Attaoui, *Atomic force microscopy study and qualitative analysis of martensite relief in zirconia.* Journal of the American Ceramic Society, 2005. **88**(5): p. 1261-1267.
37. R.W.Cahn, P.Haasen, and E.J.Kramer, *Structure and properties of ceramics*. Materials Science and Technology, ed. M.Swain. Vol. 11. 1994, Weinheim: VCH.
38. Becher, P.F. and M.V. Swain, *Grain-size dependent transformation behavior in polycrystalline tetragonal zirconia.* Journal of the American Ceramic Society, 1992. **75**(3): p. 493-502.
39. Heuer, A.H., *Transformation toughening in zirconium dioxide-containing ceramics.* Journal of the American Ceramic Society, 1987. **70**(10): p. 689-98.
40. Kelly, J.R. and I. Denry, *Stabilized zirconia as a structural ceramic: An overview.* Dental materials : official publication of the Academy of Dental Materials, 2008. **24**(3): p. 289-98.
41. Matsui, K., et al., *Cubic-formation and grain-growth mechanisms in tetragonal zirconia polycrystal.* Journal of the American Ceramic Society, 2003. **86**(8): p. 1401-1408.
42. Grain, C.F., *Phase relations in the zirconium oxide-magnesium oxide system.* Journal of the American Ceramic Society, 1967. **50**(6): p. 288-90.
43. Hellmann, J.R. and V.S. Stubican, *Stable and metastable phase relations in the system zirconia-calcia.* Journal of the American Ceramic Society, 1983. **66**(4): p. 260-4.

44. Scott, H.G., *Phase relations in the zirconia-yttria system.* Journal of Materials Science, 1975. **10**(9): p. 1527-35.
45. Scott, H.G., *Phase relations in the yttria-rich part of the yttria-zirconia system.* Journal of Materials Science, 1977. **12**(2): p. 311-16.
46. Lange, F.F., *Transformation toughening. Part 3. Experimental observations in the zirconium oxide-yttrium oxide system.* Journal of Materials Science, 1982. **17**(1): p. 240-6.
47. Tani, E., M. Yoshimura, and S. Somiya, *Revised phase diagram of the system zirconia-ceria below 1400 DegC.* Journal of the American Ceramic Society, 1983. **66**(7): p. 506-10.
48. Lange, F.F., *Transformation toughening. Part 5. Effect of temperature and alloy on fracture toughness.* Journal of Materials Science, 1982. **17**(1): p. 255-63.
49. Heuer, A.H. and M. Ruehle, *Overview No. 45. On the nucleation of the martensitic transformation in zirconia (ZrO2).* Acta Metallurgica, 1985. **33**(12): p. 2101-12.
50. Hutchinson, J.W., *Crack tip shielding by micro-cracking in brittle solids.* Acta Metallurgica, 1987. **35**(7): p. 1605-19.
51. Wang, J. and R. Stevens, *Zirconia-toughened alumina (ZTA) ceramics.* Journal of Materials Science, 1989. **24**(10): p. 3421-40.
52. I.J.McColm, *ceramic hardness*. 1990, New York: Plenum Press.
53. Chen, I.W. and P.E.R. Morel, *Implications of transformation plasticity in zirconia-containing ceramics: I, shear and dilatation effects.* Journal of the American Ceramic Society, 1986. **69**(3): p. 181-9.
54. Evans, A.G., *Perspective on the development of high-toughness ceramics.* Journal of the American Ceramic Society, 1990. **73**(2): p. 187-206.
55. McMEEKING, R.M. and A.G. EVANS, *Mechanics of Transformation-Toughening in Brittle Materials.* Journal of the American Ceramic Society, 1982. **65**(5): p. 242-246.
56. Basu, B., *Toughening of yttria-stabilized tetragonal zirconia ceramics.* International Materials Reviews, 2005. **50**(4): p. 239-256.
57. Marshall, D.B., et al., *Crack-tip transformation zones in toughened zirconia.* Journal of the American Ceramic Society, 1990. **73**(9): p. 2659-66.
58. Arashi, H., et al., *New high-pressure phase of zirconium dioxide above 35 GPa.* Physical Review B: Condensed Matter and Materials Physics, 1990. **41**(7): p. 4309-13.
59. Ohtaka, O., et al., *Phase relations and equations of state of ZrO2 under high temperature and high pressure.* Physical Review B: Condensed Matter and Materials Physics, 2001. **63**(17): p. 174108/1-174108/8.
60. Block, S., J.A.H. Da Jornada, and G.J. Piermarini, *Pressure-temperature phase diagram of zirconia.* Journal of the American Ceramic Society, 1985. **68**(9): p. 497-9.
61. Ohtaka, O., et al., *Stability of monoclinic and orthorhombic zirconia: studies by high-pressure phase equilibria and calorimetry.* Journal of the American Ceramic Society, 1991. **74**(3): p. 505-9.
62. Ohtaka, O., et al., *Phase relations and equation of state of ZrO2 to 100 GPa.* Journal of Applied Crystallography, 2005. **38**(5): p. 727-733.
63. Bouvier, P., et al., *High-pressure structural evolution of undoped tetragonal nanocrystalline zirconia.* Physical Review B: Condensed Matter and Materials Physics, 2000. **62**(13): p. 8731-8737.
64. Leger, J.M., et al., *Pressure-induced phase transitions and volume changes in hafnium oxide (HfO2) up to 50 GPa.* Physical Review B: Condensed Matter and Materials Physics, 1993. **48**(1): p. 93-8.
65. Kitano, Y., et al., *Structural changes by compressive stresses of 2.0-mol%-yttria-stabilized tetragonal zirconia polycrystals.* Journal of the American Ceramic Society, 1989. **72**(5): p. 854-5.

66. Virkar, A.V. and R.L.K. Matsumoto, *Ferroelastic domain switching as a toughening mechanism in tetragonal zirconia.* Journal of the American Ceramic Society, 1986. **69**(10): p. C224-C226.
67. Baither, D., et al., *Ferroelasticity of t'-zirconia: I, high-voltage electron microscopy studies of the microstructure in polydomain tetragonal zirconia.* Journal of the American Ceramic Society, 1997. **80**(7): p. 1691-1698.
68. Baufeld, B., et al., *Ferroelasticity of t'-zirconia: II, in situ straining in a high-voltage electron microscope.* Journal of the American Ceramic Society, 1997. **80**(7): p. 1699-1705.
69. Srinivasan, G.V., et al., *Ferroelastic domain switching in polydomain tetragonal zirconia single crystals.* J. Am. Ceram. Soc. FIELD Full Journal Title:Journal of the American Ceramic Society, 1989. **72**(11): p. 2098-103.
70. Chan, C.-J., et al., *Ferroelastic domain switching in tetragonal zirconia single crystals - microstructural aspects.* Journal of the American Ceramic Society, 1991. **74**(4): p. 807-13.
71. Hannnink, R.H.J. and M.V. Swain, *Metastability of the martensitic transformation in a 12 mol% ceria-zirconia alloy: I. Deformation and fracture observations.* Journal of the American Ceramic Society, 1989. **72**(1): p. 90-8.
72. Grathwohl, G. and T. Liu, *Crack resistance and fatigue of transforming ceramics: II, ceria-stabilized tetragonal zirconia.* Journal of the American Ceramic Society, 1991. **74**(12): p. 3028-34.
73. P.Ostojic and R.McPherson, *A review of indentation fracture theory: its development, principles and limitations.* International Journal of fracture, 1987. **33**: p. 297-312.
74. Clarke, D.R. and F. Adar, *Measurement of the crystallographically transformed zone produced by fracture in ceramics containing tetragonal zirconia.* Journal of the American Ceramic Society, 1982. **65**(6): p. 284-8.
75. Kaliszewski, M.S., et al., *Indentation studies on Y2O3-stabilized ZrO2: I. Development of indentation-induced cracks.* Journal of the American Ceramic Society, 1994. **77**(5): p. 1185-93.
76. Dransmann, G.W., et al., *Indentation studies on Y2O3-stabilized ZrO2: II. Toughness determination from stable growth of indentation-induced cracks.* Journal of the American Ceramic Society, 1994. **77**(5): p. 1194-201.
77. Dauskardt, R.H., D.K. Veirs, and R.O. Ritchie, *Spatially resolved Raman spectroscopy study of transformed zones in magnesia-partially-stabilized zirconia.* Journal of the American Ceramic Society, 1989. **72**(7): p. 1124-30.
78. Behrens, G., G.W. Dransmann, and A.H. Heuer, *On the isothermal martensitic transformation in 3Y-TZP.* Journal of the American Ceramic Society, 1993. **76**(4): p. 1025-30.
79. Lee, S.K., et al., *Scratch damage in zirconia ceramics.* Journal of the American Ceramic Society, 2000. **83**(6): p. 1428-1432.
80. Lee, S.K., R.P. Jensen, and M.J. Readey, *Effect of grain size on scratch damage in Y-TZP ceramics.* Journal of Materials Science Letters, 2001. **20**(14): p. 1341-1343.
81. Lee, S.W., S.M. Hsu, and M.C. Shen, *Ceramic wear maps: zirconia.* Journal of the American Ceramic Society, 1993. **76**(8): p. 1937-47.
82. Sasaki, S., *The effects of the surrounding atmosphere on the friction and wear of alumina, zirconia, silicon carbide, and silicon nitride.* Wear, 1989. **134**(1): p. 185-200.
83. Basu, B., J. Vleugels, and O. Van Der Biest, *Microstructure-toughness-wear relationship of tetragonal zirconia ceramics.* Journal of the European Ceramic Society, 2004. **24**(7): p. 2031-2040.
84. Asif, S.A.S., et al., *Surface damage of yttria-tetragonal zirconia polycrystals and magnesia-partially-stabilized zirconia in single-point abrasion.* Journal of the American Ceramic Society, 1995. **78**(12): p. 3357-62.

85. Nagarajan, V.S., et al., *Raman spectroscopic studies of phase transformations induced by a notch cut on a 3Y-TZP sample.* Materials Science & Engineering, A: Structural Materials: Properties, Microstructure and Processing, 1994. **A174**(2): p. L37-L40.
86. Sato, T. and M. Shimada, *Transformation of yttria-doped tetragonal zirconia polycrystals by annealing in water.* Journal of the American Ceramic Society, 1985. **68**(6): p. 356-9.
87. Lange, F.F., G.L. Dunlop, and B.I. Davis, *Degradation during aging of transformation-toughened zirconia-yttria materials at 250.degree.c.* Journal of the American Ceramic Society, 1986. **69**(3): p. 237-40.
88. Yoshimura, M., et al., *Role of water on the degradation process of Y-TZP [yttrium-doped tetragonal zirconia].* Journal of Materials Science Letters, 1987. **6**(4): p. 465-7.
89. Guo, X., *On the degradation of zirconia ceramics during low-temperature annealing in water or water vapor.* Journal of Physics and Chemistry of Solids, 1999. **60**(4): p. 539-546.
90. Guo, X., *Property Degradation of Tetragonal Zirconia Induced by Low-Temperature Defect Reaction with Water Molecules.* Chemistry of Materials, 2004. **16**(21): p. 3988-3994.
91. Schmauder, S. and H. Schubert, *Significance of internal stresses for the martensitic transformation in yttria-stabilized tetragonal zirconia polycrystals during degradation.* Journal of the American Ceramic Society, 1986. **69**(7): p. 534-40.
92. Chevalier, J., L. Gremillard, and S. Deville, *Low-temperature degradation of zirconia and implications for biomedical implants.* Annual Review of Materials Research, 2007. **37**: p. 1-32.
93. Sato, T., S. Ohtaki, and M. Shimada, *Transformation of yttria partially stabilized zirconia by low temperature annealing in air.* Journal of Materials Science, 1985. **20**(4): p. 1466-70.
94. Sato, T. and M. Shimada, *Crystalline phase change in yttria-partially-stabilized zirconia by low-temperature annealing.* Journal of the American Ceramic Society, 1984. **67**(10): p. C212-C213.
95. Eichler, J., et al., *Effect of grain size on mechanical properties of submicrometer 3Y-TZP: fracture strength and hydrothermal degradation.* Journal of the American Ceramic Society, 2007. **90**(9): p. 2830-2836.
96. Lilley, E., *Review of low-temperature degradation in Y-TZPs.* Ceramic Transactions, 1990. **10**(Corros. Corros. Degrad. Ceram.): p. 387-407.
97. Roy, M.E., et al., *Phase transformation, roughness, and microhardness of artificially aged yttria- and magnesia-stabilized zirconia femoral heads.* Journal of Biomedical Materials Research, Part A, 2007. **83A**(4): p. 1096-1102.
98. Sekulic, A., et al., *Determination of the monoclinic, tetragonal and cubic phases in mechanically alloyed ZrO2-Y2O3 and ZrO2-CoO powder mixtures by Raman spectroscopy.* Journal of Materials Science Letters, 1997. **16**(4): p. 260-262.
99. N.B.Colthup, L.H.Daly, and S.E.Wiberley, *Introduction to infrared and raman spectroscopy*. third ed. 1990, San Diego: Academic Press,Inc.
100. *Infrared and Raman spectroscopy*. Methods and Applications, ed. B. Schrader. 1995, Weinheim: VCH.
101. Kim, B.K. and H. Hamaguchi, *Mode assignments of the Raman spectrum of monoclinic zirconia by isotopic exchange technique.* Physica Status Solidi B: Basic Research, 1997. **203**(2): p. 557-563.
102. Arashi, H. and M. Ishigame, *Raman spectroscopic studies of the polymorphism in zirconium dioxide at high pressures.* Physica Status Solidi A: Applied Research, 1982. **71**(2): p. 313-21.
103. Keramidas, V.G. and W.B. White, *Raman scattering study of the crystallization and phase transformation of zirconium dioxide.* Journal of the American Ceramic Society, 1974. **57**(1): p. 22-4.

104. Kelly, P.M. and C.J. Ball, *Crystallography of stress-induced martensitic transformations in partially stabilized zirconia.* Journal of the American Ceramic Society, 1986. **69**(3): p. 259-64.
105. Feinberg, A. and C.H. Perry, *Structural disorder and phase transitions in zirconia-diyttrium trioxide system.* Journal of Physics and Chemistry of Solids, 1981. **42**(6): p. 513-18.
106. Quintard, P.E., et al., *Comparative lattice-dynamical study of the Raman spectra of monoclinic and tetragonal phases of zirconia and hafnia.* Journal of the American Ceramic Society, 2002. **85**(7): p. 1745-1749.
107. Merle, T., et al., *Polarized Raman spectra of tetragonal pure ZrO2 measured on epitaxial films.* Physical Review B: Condensed Matter and Materials Physics, 2002. **65**(14): p. 144302/1-144302/6.
108. Cai, J., Y.S. Raptis, and E. Anastassakis, *Stabilized cubic zirconia: a Raman study under uniaxial stress.* Applied Physics Letters, 1993. **62**(22): p. 2781-3.
109. Kermaides, V.G. and W.B. White, *Raman scattering from CaxAr1-xO2-xXx, a system with massive point defects.* Journal of Physics and Chemistry of Solids, 1973. **34**(11): p. 1873-8.
110. Morell, G., et al., *Raman scattering study of thermally reduced stabilized cubic zirconia.* Journal of Applied Physics, 1997. **81**(6): p. 2830-2834.
111. Michel, D., M. Perez y Jorba, and R. Collongues, *Study by Raman spectroscopy of order-disorder phenomena occurring in some binary oxides with fluorite-related structures.* Journal of Raman Spectroscopy, 1976. **5**(2): p. 163-80.
112. Haines, J. and J.M. Leger, *Characterization of the cotunnite-type phases of zirconia and hafnia by neutron diffraction and Raman spectroscopy.* Journal of the American Ceramic Society, 1997. **80**(7): p. 1910-1914.
113. Mirgorodsky, A.P. and P.E. Quintard, *Lattice-dynamic treatment of vibrational and elastic properties of cotunnite-type ZrO2 and HfO2: comparison with ambient pressure polymorphs.* Journal of the American Ceramic Society, 1999. **82**(11): p. 3121-3124.
114. Alzyab, B., C.H. Perry, and R.P. Ingel, *High-pressure phase transitions in zirconia and yttria-doped zirconia.* Journal of the American Ceramic Society, 1987. **70**(10): p. 760-5.
115. Kourouklis, G.A. and E. Liarokapis, *Pressure and temperature dependence of the Raman spectra of zirconia and hafnia.* Journal of the American Ceramic Society, 1991. **74**(3): p. 520-3.
116. Ishigame, M. and T. Sakurai, *Temperature dependence of the Raman spectra of zirconia.* Journal of the American Ceramic Society, 1977. **60**(7-8): p. 367-9.
117. Phillippi, C.M. and K.S. Mazdiyasni, *Infrared and Raman spectra of zirconia polymorphs.* Journal of the American Ceramic Society, 1971. **54**(5): p. 254-8.
118. Siu, G.G., M.J. Stokes, and Y. Liu, *Variation of fundamental and higher-order Raman spectra of ZrO2 nanograins with annealing temperature.* Physical Review B: Condensed Matter and Materials Physics, 1999. **59**(4): p. 3173-3179.
119. Fangxin, L., Y. Jinlong, and Z. Tianpeng, *Raman and Fourier-transform infrared photoacoustic spectra of granular ZrO2.* Physical Review B: Condensed Matter, 1997. **55**(14): p. 8847-8851.
120. Perry, C.H., D.W. Liu, and R.P. Ingel, *Phase characterization of partially stabilized zirconia by Raman spectroscopy.* Journal of the American Ceramic Society, 1985. **68**(8): p. C-184-C-187.
121. Lughi, V. and D.R. Clarke, *Temperature dependence of the yttria-stabilized zirconia Raman spectrum.* Journal of Applied Physics, 2007. **101**(5): p. 053524/1-053524/6.
122. Jouanne, M., et al., *Structural transformation in nanosized zirconium oxide.* Physical Review B: Condensed Matter and Materials Physics, 2001. **64**(15): p. 155404/1-155404/7.
123. Kim, D.-J., J.-W. Jang, and H.-L. Lee, *Effect of tetravalent dopants on Raman spectra of tetragonal zirconia.* Journal of the American Ceramic Society, 1997. **80**(6): p. 1453-1461.

124. Arashi, H. and M. Yoshimura, *Determination of tetragonal-cubic phase boundary of Zr1-xRxO2-x/2 (R = Nd, Sm, Y, Er and Yb) by Raman scattering.* Journal of Physics and Chemistry of Solids, 1996. **57**(1): p. 17-24.
125. Yashima, M., et al., *Raman scattering study of cubic-tetragonal phase transition in Zr1-xCexO2 solid solution.* Journal of the American Ceramic Society, 1994. **77**(4): p. 1067-71.
126. Li, P., I.W. Chen, and J.E. Penner-Hahn, *Effect of dopants on zirconia stabilization - an x-ray absorption study: II. Tetravalent dopants.* Journal of the American Ceramic Society, 1994. **77**(5): p. 1281-8.
127. Fujimori, H., et al., *Structural changes of scandia-doped zirconia solid solutions: Rietveld analysis and Raman scattering.* Journal of the American Ceramic Society, 1998. **81**(11): p. 2885-2893.
128. Yu.K.Voronko, et al., *Raman scattering in zirconium oxide-gadolinium oxide and zirconium oxide-europium oxide single crystals of tetragonal structure.* Opt.Spectrosc., 1981. **51**(4): p. 315-316.
129. Dorn, M.T. and K.G. Nickel, *Zirconia ceramics: phase transitions and Raman microspectroscopy.* High-Pressure Surface Science and Engineering, 2004: p. 467-520.
130. *ABAQUS/Standard, Getting started with ABAQUS, Version 6.5*
131. Dorn, M., *Phasenumwandlungen in TZP-ZrO_2-Zirkonoxid durch lokale mechanische Belastung*, in *Geowissenschaftlichen Fakultät*. 2003, Eberhard-Karls-Universität Tübingen: Tübingen.
132. Kontoyannis, C.G. and G. Carountzos, *Quantitative determination of the cubic-to-monoclinic phase transformation in fully stabilized zirconias by Raman spectroscopy.* Journal of the American Ceramic Society, 1994. **77**(8): p. 2191-4.
133. Garvie, R.C. and P.S. Nicholson, *Phase analysis in zirconia systems.* Journal of the American Ceramic Society, 1972. **55**(6): p. 303-5.
134. G.S.A.M.THEUNISSEN, J.S.B., A.J.A.WINNUBST, *Mechanical Properties of ultra-fine grained zirconia ceramics.* Journal of Materials Science 1992. **27**: p. 4429-4438.
135. J.Wang, M.R.a.R.S., *The Grain Size Dependence of the Mechanical Properties in TZP Ceramics.* Br.Ceram.Trans.J., 1988. **88**(1): p. 1-6.
136. Wermelinger, T., et al., *3-D Raman spectroscopy measurements of the symmetry of residual stress fields in plastically deformed sapphire crystals.* Acta Materialia, 2007. **55**(14): p. 4657-4665.
137. Yamazaki, K., et al., *Raman scattering characterization of residual stresses in silicon-on-sapphire.* Japanese Journal of Applied Physics, Part 1: Regular Papers, Short Notes & Review Papers, 1984. **23**(6): p. 681-6.
138. Yamazaki, K., et al., *Raman microprobe study on relaxation of residual stresses in patterned silicon-on-sapphire.* Japanese Journal of Applied Physics, Part 2: Letters, 1984. **23**(6): p. 403-5.
139. Harlan, N.R., et al., *Phase distribution and residual stresses in melt-grown Al2O3-ZrO2(Y2O3) eutectics.* Journal of the American Ceramic Society, 2002. **85**(8): p. 2025-2032.
140. Pan, L.S. and S. Horibe, *An in-situ investigation on the critical phase transformation stress of tetragonal zirconia polycrystalline ceramics.* Journal of Materials Science, 1996. **31**(24): p. 6523-6527.
141. Adachi, T., et al., *Measurement of microscopic stress distribution of multilayered composite by X-ray stress analysis.* Materials Letters, 2003. **57**(20): p. 3057-3062.
142. Anton, R.J., Miskioglu, I., Subhash, G. , *Determination of resudual stress fields beneath a Vickers indentation using photoelasticity.* Experimental Mechanics, 1999. **39(3)**: p. 227-230.

143. Banerjee, D., et al., *Characterization of residual stresses in a sapphire-fiber-reinforced glass-matrix composite by micro-fluorescence spectroscopy.* Composites Science and Technology, 2001. **61**(11): p. 1639-1647.
144. Niku-Lari, A., Lu, J. and Flavenot, J. F. , *Measurement of residual-stress distribution by the incremental hole-drilling method.* Experimental Mechanics, 1985. **25(2)**: p. 175-185.
145. Tanaka, M., et al., *Measurement of residual stress in air plasma-sprayed Y2O3-ZrO2 thermal barrier coating system using micro-Raman spectroscopy.* Mater. Sci. Eng., A FIELD Full Journal Title:Materials Science & Engineering, A: Structural Materials: Properties, Microstructure and Processing, 2006. **A419**(1-2): p. 262-268.
146. Tomimatsu, T., Y. Kagawa, and S.J. Zhu, *Residual stress distribution in electron beam-physical vapor deposited ZrO2 thermal barrier coating layer by Raman spectroscopy.* Metallurgical and Materials Transactions A: Physical Metallurgy and Materials Science, 2003. **34A**(8): p. 1739-1741.
147. Tochino, S., et al., *Spatially resolved raman spectroscopy for In-depth non-destructive residual stress and phase transformation assessments in 3Y-TZP bioceramics.* Key Engineering Materials, 2006. **309-311**(Pt. 2, Bioceramics): p. 1203-1206.
148. Teixeira, V., Nndritschky,M.,Fischer,W., Buchkremer.H.P.,Stöver,D., *Analysis of residual stresses in thermal barrier coatings.* Journal of Materials Processing Technology, 1999. **92-93**: p. 209-216.
149. Ficher-Cripps, A.C., *Nanoindentation*. Mechanical Engineering Series, ed. F.F. Ling. 2002, Austin: Springer.
150. Sanchez-Gonzalez, E., et al., *Application of Hertzian tests to measure stress-strain characteristics of ceramics at elevated temperatures.* Journal of the American Ceramic Society, 2007. **90**(1): p. 149-153.
151. L.S.Pan, S.H., *An In-situ investigation on the critical phase transformation stress of tetragonal zirconia polycrystalline ceramics.* Journal of Materials Science, 1996. **31**: p. 6523-6527.

7 Figure captions